The Impact of Radio-AGN on Star Formation Across Cosmic Time

Jasmeer Virdee

Astrophysics Department

University of Oxford

A thesis submitted for the degree of

Doctor of Philosophy

I would like to dedicate this thesis to my parents, Tejinder & Vatsala Virdee. Without my father, I would never have wanted to become a physicist. Without my mother, I would never have succeeded.

Acknowledgements

I wish to thank my supervisors Dr. Dimitra Rigopoulou and Prof. Steven Rawlings for their guidance and support throughout my D.Phil. I would also like to extend a special thanks to Prof. Martin Hardcastle and Prof. Matt Jarvis for their support after the unfortunate death of Prof. Rawlings.

A number of post-docs have been tremendously helpful throughout this process, and I owe them special gratitude: to Tom Mauch, for teaching me how to build radio catalogues; Roger Dean, for helping me write EVN proposals; Ian Heywood, for helping me to understand how VLBI works and how to reduce the data; Aprajita Verma, for general advice and help on a wide range of issues; Georgios Magdis, for his help throughout the latter stages of my D.Phil and for an incredibly fun observing trip to Arizona!

All the members of Oxford Astrophysics, especially my fellow D.Phil students, have demonstrated extraordinary generosity and humility and have always made me feel comfortable enough to ask stupid questions. The Astrophysics secretaries, Mrs Vanessa-Ferraro Wood and Mrs Ashling Morris, have helped me with the many administrative issues I have encountered during my time in Oxford, and I am very grateful for their patience and kindness.

I would also like to acknowledge the unquestioning support of my mother, father, and sister, Natisha. Finally, I would like to thank Devani Singh, whose presence throughout my D.Phil has made the whole thing worth it.

Abstract

This thesis presents a detailed study of the impact of radio-AGN on star formation and the interstellar medium (ISM) of galaxies across cosmic time. To do this, this thesis uses far-IR / sub-mm data from the *Herschel Space Observatory*. I create a well-selected sample of 1599 radio sources using the *NRAO VLA Sky Survey* (NVSS) and *Faint Images of the Radio Sky at Twenty-Centimeters* (FIRST) data in combination with the *UKIRT Infrared Deep Sky Survey - Large Area Survey* (UKIDSS - LAS) data. I find that the far-IR luminosities and dust temperatures of radio galaxies are lower in comparison to those of non-radio-detected galaxies. This luminosity deficit grows with increasing stellar mass. I argue that the reasons for these differences is probably due to indirect radio-AGN feedback, i.e. radio jets mechanically heat the halo-environment, preventing external sources of cold gas from entering the host and forming stars. The far-IR luminosity and dust temperature is found to decrease as a function of radio source size. I find the most likely explanation for this is jet-induced star formation while the jets are confined to the ISM. Finally, a method for identifying reliable high-z, star-bursting radio sources in the H-ATLAS is described with which statistically significant studies of radio-jet induced star formation may be undertaken.

Contents

List of Figures

Chapter 1

Introduction

1.1 Preamble

Approximately half of all the energy emitted since the Big Bang by all the objects in the Universe has been absorbed by dust and then reradiated between 60-500 μm (Dwek et al. 1998; Fixsen et al. 1998; Dole et al. 2006; Driver et al. 2008). The source of this emission is thermally radiating dust grains (made principally of amorphous silicates and some form of carbonaceous materials; Li & Draine 2001; Draine & Li 2007) which are generally produced in three ways: (1) by condensation in the winds of low / intermediate mass evolved-asymptotic giant-branch stars, (2) by condensation in ejecta from supernovae, and (3) by accretion in dark clouds (Gehrz 1989). Dust is only expected to contribute between 0.01 to a few percent of the total baryonic mass of a galaxy (Dunne et al. 2011; Bourne et al. 2012; Rowlands et al. 2012). Naively, this might lead one to believe that the dust content of a galaxy plays a negligible role in the field of galaxy evolution. However, a large amount of information concerning the growth and evolution of galaxies is contained within this wavelength regime. The star-formation rate (SFR) of a galaxy is one of the most informative parameters because it allows one to determine the growth in stellar mass. Star formation

results in copious amounts of ultra-violet (UV) radiation, emitted primarily from short-lived high-mass stars (e.g. OB stars). This radiation excites atomic / molecular transitions at a wide range of wavelengths, allowing hydrogen recombination lines (e.g. H_α and H_β), optical forbidden lines (e.g. [O II] and [O III]) and FIR cooling lines (e.g. $[CII]_{158}$), amongst other indicators, to be used as tracers of star formation (see Kennicutt 1998a and Calzetti 2012 for reviews of SFR indicators). However, SFR indicators at optical / UV wavelengths suffer from extinction by the dust which surrounds and envelops these star-forming regions. The dust grains which absorb the UV radiation re-process the light, and emit it at FIR wavelengths (the 60-500 μm regime) which is on the whole, optically thin. This means that, in principle, one can use the FIR luminosity to estimate the SFR without needing to account for extinction, a difficult quantity to measure especially at high redshift (see Kennicutt 1998a).

The processes which govern the growth and evolution of galaxies involve many complex phenomena. Models which seed and evolve galaxies in accordance with the growth of their dark matter haloes lead to an over-prediction of the number of faint galaxies (i.e. low mass) and / or bright galaxies (i.e. high mass) in the local Universe (e.g. Cole et al. 2000; Benson et al. 2003; Springel et al. 2005 and references therein). The over-production of low mass galaxies at the faint end of the galaxy luminosity function has largely been resolved by the introduction of photo-ionisation and supernova feedback into the models (e.g. Benson et al. 2002). The net effect is to eject gas and dust from low-mass dark matter haloes, which host the least luminous galaxies. However, at the bright-end of the luminosity function, which traces the most massive systems, a problem remains. The ejected gas in systems embedded in higher-mass haloes cannot escape and therefore cools back onto the central galaxy, eventually stimulating star-formation and by extension, galaxy growth. An additional source of energy is required, either to eject the gas or prevent its accretion onto the galaxy in the first place. This motivates the need to tap into the vast energy released by the accretion of

gas onto super-massive black-holes (SMBH) (e.g. Granato et al. 2004; Di Matteo, Springel & Hernquist 2005; Sijacki & Springel 2006; Bower et al. 2006; Croton et al. 2006; Bower, McCarthy & Benson 2008; Merloni & Heinz 2008; Martizzi et al. 2012; Vogelsberger et al. 2013). Objects which show signs of emission due to this accretion process are commonly referred to as active galactic nuclei (AGN).

Radio-loud AGN are an important subset of the general AGN population. The source of the radio emission is high-energy electrons, launched by the SMBH, gyrating in inter-galactic magnetic fields. The radio AGN activity of the most massive galaxies has been used in models to induce the sharp cutoff in the optical luminosity function of low-redshift galaxies (see above references). The fraction of galaxies showing radio-loud activity is also a very strong function of stellar mass (e.g. Sadler et al. 2002; Best et al. 2005; Mauch & Sadler 2007), providing a natural selection function for solving the bright-end problem. Radio jets deposit large amounts of energy into the halo, preventing the hot gas from cooling and so from providing fuel for more star formation. The result should be less gas and dust in the hosts of radio AGN, a prediction which could be tested observationally. However, recent studies of the dust properties of an unbiased sample of radio galaxies has been restricted by the absence of large area surveys with deep photometry between 100-500 μm. Targeted surveys of the most powerful radio galaxies show that the FIR / sub-mm luminosity is a strong function of redshift (see Archibald et al. 2001; Reuland et al. 2004), although this is also thought to be true of the general galaxy population (e.g. Eales et al. 2010b; Dunne et al. 2011). Thus, placing these results in context is difficult. To help facilitate a study of the effects of feedback, the ideal case involves comparing the FIR properties of radio galaxies and 'normal' galaxies (i.e. non-radio-detected) using a single FIR survey with a uniform depth. This allows for the use of much better statistics and for biases to be more easily accounted for.

The successful launch of the *Herschel Space Observatory* (*HSO*; Pilbratt et al. 2010)

in May 2009 provided the platform for such a survey. The largest Open Time survey, the *Herschel*-Astrophysical Terahertz Large Area Survey (H-ATLAS; Eales et al. 2010a) has mapped 550 sq. degrees at 100, 160, 250, 350 and 500 μm, allowing the FIR properties of the radio sources which fall into this area to be studied in unprecedented detail.

This thesis offers an in-depth investigation into the FIR properties of radio AGN. This is done by selecting both large and small samples of galaxies, by targeting the low- and high-redshift regimes, by using statistical / stacking methods and observations of individual sources. In short, this thesis reveals the FIR properties of radio galaxies with a focus on illuminating the role of radio-jet feedback across cosmic time.

1.2 Cosmology

1.2.1 A brief history of the Universe

After the Big Bang, the Universe was in an extremely hot and dense state which then underwent rapid expansion from a singularity to its present size, some 13.8 billion years ago. As the Universe expanded, it cooled, allowing the first nuclei to form. After approximately 370,000 years, the Universe had cooled sufficiently to produce electrically neutral atoms. At this point, photons de-coupled from electrons and were thus able to travel unimpeded, forming what we now call the Comic Microwave Background (CMB). As the Universe continued to cool, random fluctuations began to create structure. Areas with slightly lower temperatures began to condense due to the gravitational forces between atoms. This runaway process eventually formed the first stars, and as they coalesced, the first galaxies. In the following section, I discuss the overall structure of the Universe and how to compute some basic parameters.

1.2.2 Redshift and distances

The expansion of the Universe causes light travelling through space to be stretched from its emitted wavelength λ_{emit}, to its observed wavelength λ_{obs}. The redshift, z, is a measure of this shift and is defined as follows,

$$z = \frac{\lambda_{obs} - \lambda_{emit}}{\lambda_{emit}} \tag{1.1}$$

The measured cosmological redshift is related to the scale factor, $R(t)$ which describes the expansion of the Universe at time t, and can be re-written as,

$$(1 + z) = \frac{R(t_{obs})}{R(t_{emit})} \tag{1.2}$$

From Eq. 1.2 it is clear that the redshift of an object is directly related to the scale factor. Therefore, if one knows the values of the cosmological parameters which determine the scale factors, distances may be calculated.

The *comoving distance* is the distance between two objects after factoring out the expansion of the Universe. The *proper distance* is the distance one would measure between two objects using a set of rulers. The comoving and proper distance are defined as equaling each other at the present time (i.e. the comoving distance has been 'normalised' to the present day - $R(t_0) = 1$), although for distances between sources in the past, the proper distance is the comoving distance divided by a factor of (1+z). We can define the present comoving distance D_M as,

$$D_M = \frac{c}{H_0} \int_0^z \frac{dz}{\sqrt{\Omega_M (1+z)^3 + \Omega_k (1+z)^2 + \Omega_\Lambda}}, \tag{1.3}$$

where Ω_M, Ω_K and Ω_Λ are density parameters (the ratio of the observed density to the

critical density in a Friedmann Universe; Hogg 1999).

In many ways, the comoving distance is the fundamental distance measure, as all other distances are derived in terms of it. For a flat Universe ($k = 0$) such as ours, the transverse comoving distance does not differ from the 'line-of-sight' comoving distance. This allows us to write the angular diameter distance D_A, which is the ratio of an object's physical transverse size to its angular size (in radians), in terms of D_M,

$$D_A = \frac{D_M}{1+z} \tag{1.4}$$

In this thesis, D_A is used to calculate e.g. the sizes of radio sources. The luminosity distance, D_L, is simply defined as,

$$D_L = \sqrt{\frac{L}{4\pi S}} \tag{1.5}$$

where S is the bolometric flux. Eq. 1.5 can be re-written in terms of D_M and D_A as follows,

$$D_L = (1+z)D_M = (1+z)^2 D_A \tag{1.6}$$

Direct measurement of the H_0 using Cepheid variables suggest $H_0 = 74.2 \pm 3.6$ km s^{-1} Mpc^{-1} (Riess et al. 2009). In combination with the CMB and supernovae results, these measurements imply the Universe is flat (or very close to it) with $\Omega_M = 0.3$, $\Omega_k = 0$ and $\Omega_\Lambda = 0.7$ (Planck Collaboration et al. 2013b). Throughout the thesis I use a concordance cosmology with $H_0 = 70$ km s^{-1} Mpc^{-1}, $\Omega_\mathrm{m} = 0.3$ and $\Omega_\Lambda = 0.7$.

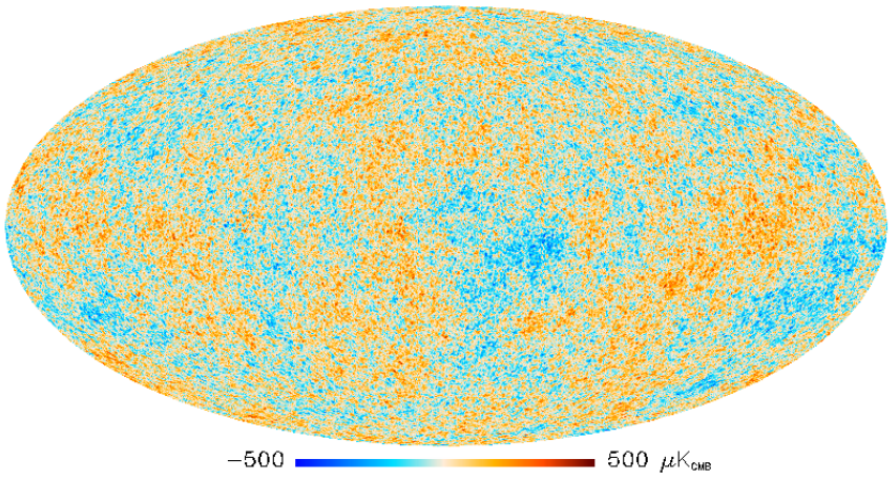

Figure 1.1: All-sky picture of the Universe created from the *Planck* survey's second data release (Planck Collaboration et al. 2013a). The image reveals temperature fluctuations (shown as colour differences) that correspond to the seeds that grew to become galaxies.

1.3 Galaxy evolution

The formation and evolution of galaxies is a complex story, the details of which are not yet fully understood. In this section, I attempt to summarise the current state of our knowledge and provide the necessary background to place the work of this thesis into context. First, I describe how the first stars and galaxies are thought to have formed, followed by a discussion of the major factors which affected their evolution. Next, I give a brief overview of the evolution of super-massive black-holes. In the last section, I concentrate on what can be learnt from the luminosity function of galaxies, and how well current models fit the data. The success and failures of galaxy evolution models form the basis for our understanding of the need for AGN feedback in the galaxy population as a whole.

1.3.1 Fluctuations, the first galaxies and their early evolution

The temperature / density fluctuations observed in the CMB (see Fig. 1.1) are thought to have a quantum mechanical origin. With the passage of time, those regions of space which

were slightly colder encouraged a rapid density build-up of dark-matter particles which in turn formed the first haloes. The evolution of these fluctuations is well described by N-body simulations (e.g. Springel et al. 2005; Springel, Frenk & White 2006) which show that haloes are gathered into filamentary structures, creating the 'cosmic web'. Inside the first dark-matter haloes, the first stars were born. These stars would have been composed entirely of hydrogen and helium and, as a result, they would have been extremely massive (perhaps $> 100\,\mathrm{M}_{\odot}$; for reviews of the 'first stars', see Bromm & Larson 2004 and Glover 2005). When they exploded as supernovae, they spread metals across a wide area immediately altering the nature of the subsequent stellar population. In mini dark-matter haloes, the mechanical and radiative energy associated with these first stars also had the effect of either delaying or completely suppressing the formation of further stars. Recent simulations seem to suggest that dark-matter haloes containing a mass of $\sim 10^{8}\,\mathrm{M}_{\odot}$ by $z \sim 10$ were the hosts of the first *bona-fide* galaxies (Wise & Abel 2007, 2008; Greif et al. 2010, 2008). The evolution of such haloes is shown in Fig. 1.2 (see Bromm & Yoshida 2011 for a review of early galaxy evolution).

By $z \sim 10$ most of the first galaxies were in place. In order to grow, sources of cold gas were necessary. This is because cold gas (i.e. $< 30\,\mathrm{K}$) is the fuel for star formation. There are two primary modes for acquiring cold gas. The first is through 'wet' (i.e. gas rich) major-merger activity and the second through simple cold gas accretion from the IGM. At high-z, major mergers are thought to have played a significant role in the build up of stellar mass (Bournaud et al. 2011), which is supported by the prevalence of morphologically distorted galaxies at high redshifts (e.g. Wang et al. 2012 and references therein). However, simulations (e.g. Cattaneo et al. 2011) show that the importance of major mergers is a strong function of stellar mass, implying that only in massive galaxies ($\mathrm{M} > 10^{11}\,\mathrm{M}_{\odot}$) do major mergers contribute to the bulk of stellar-mass growth. At lower masses, the frequency of

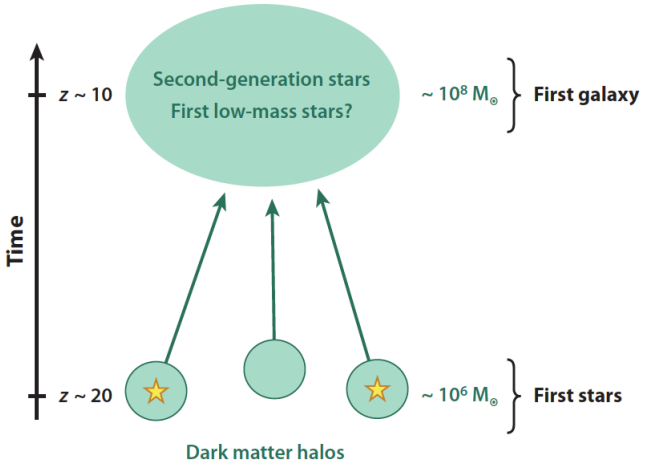

Figure 1.2: Assembly of the first galaxies. At $z \sim 20$, the first stars are formed, but clear their haloes of gas through stellar feedback mechanisms. By redshift 10, many of these mini-haloes have coalesced and a new population of stars is created, creating the first galaxies (Fig. 1 from Bromm & Yoshida 2011).

major mergers declines rapidly, limiting their ability to be responsible for mass growth. For low-mass galaxies, the bulk of their growth must come through gas accretion.

At intermediate / low redshifts the situation changes. Massive galaxies, which as we will see tend to host radio AGN, experience major mergers less often and are therefore thought to acquire most of their mass through cold flows (see Kereš et al. 2005; Dekel et al. 2009; Daddi et al. 2010 and references therein). Cold flows are streams or filaments of cold gas which penetrate the halo environment. The gas temperature of the most massive haloes can exceed 10^6 K as a result of the deep potential-well which accelerates in-falling gas. Once the gas exceeds the sound speed it is shock heated. This makes simple, uniform spherical accretion onto the host difficult as the gas must first have time to cool. In addition, AGN feedback processes, which will be discussed in more detail in Section 1.3.3, can effectively delay gas cooling for times comparable to the current Hubble time. However, shock heating of the gas is only a problem for massive dark-matter haloes ($> 10^{11}\,M_{\odot}$) (see Fig. 1.3). Throughout this period, galaxies hosted in lower mass haloes will continue to grow via standard cold-gas

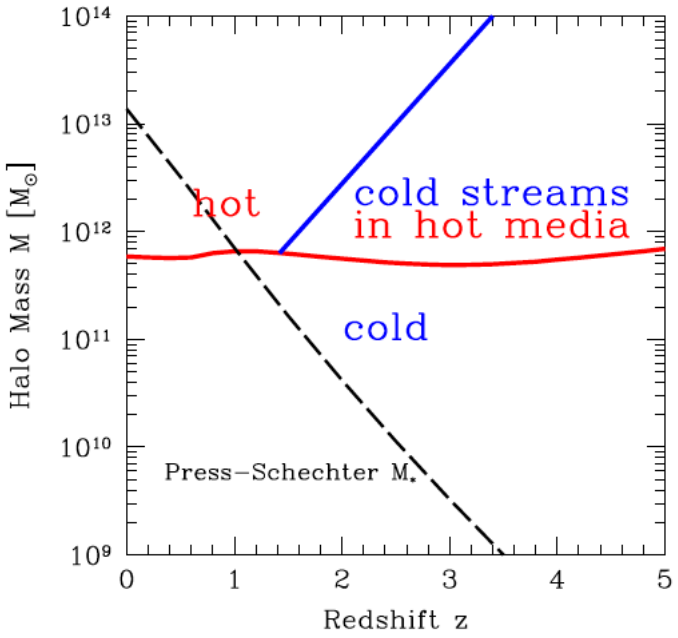

Figure 1.3: An analytic prediction for the regimes dominated by cold flows and shock-heated gas in the plane of halo mass and redshift. Also shown is the characteristic Press-Schechter halo mass $M^*(z)$; it is much smaller than M_{shock} at $z > 2$ (Fig. 5 from Dekel et al. 2009).

accretion and (possibly) merger activity.

1.3.2 The evolution of black holes

Super-massive black-holes are thought to inhabit the central region of nearly every galaxy in the Universe. Indeed, the masses of these objects are correlated with either the mass (e.g. Magorrian et al. 1998; McLure & Dunlop 2002; Marconi & Hunt 2003) or velocity dispersion (e.g. Merritt & Ferrarese 2001; Tremaine et al. 2002; Gültekin et al. 2009) of spheroids, demonstrating a direct link between the origins of galaxies and SMBHs (note, these relations have been empirically verified only for the nearby Universe due to the resolution needed to carry out the measurements). However, the origin of the SMBHs which power the luminous quasars observed at high redshifts remains unknown. Spectroscopic observations of these quasars suggest that SMBHs with masses up to $10^{10}\,M_{\odot}$ were already in place a bil-

lion years after the Big Bang (e.g. Fan et al. 2001; Willott et al. 2003). Such high-mass SMBHs require a rapid formation time scale and thus might pose a problem to current theories describing the formation of these objects. There are two favoured ideas for the origin of SMBHs.

Population III stellar remnants: The first uses the black-holes of 'dead' Population III stars as seeds which then grow via gas accretion (Madau & Rees 2001; Volonteri & Rees 2006; Li et al. 2007; Tanaka & Haiman 2009). In this case, the initial seed mass would be around $100\,\mathrm{M}_{\odot}$. Even if the black-hole accreted at or near the Eddington luminosity, growing to the mass required to power high-z quasars observed in large area surveys such as the Sloan Digital Sky Survey (SDSS; Ahn et al. 2012) would be difficult. In addition, a significant impediment is the radiative stellar feedback and the subsequent supernova which accompanies the formation of the black hole. As we have seen, these feedback effects effectively clear out the surrounding environment of gas leading to inefficient black-hole accretion for at least the free-fall time of the dark-matter halo (Johnson & Bromm 2007; Pelupessy, Di Matteo & Ciardi 2007; Alvarez, Wise & Abel 2009). In addition, radiative feedback from subsequent accretion may inhibit gas cooling, exacerbating the problem. This early bottleneck poses a serious challenge to the Population III stellar remnant scenario; however, it should be noted that not all the SMBHs need to grow rapidly to account for the observation of relatively rare, massive high-redshift SMBHs.

Direct collapse: The second idea involves the collapse of massive primordial gas clouds directly into black holes (Loeb & Rasio 1994; Eisenstein & Loeb 1995). In theory, such clouds should fragment and form individual stars due to local thermal instabilities; however, if H_2 and metal cooling could be suppressed (and thus shut off this avenue for low temperature cooling) massive gas clouds would collapse isothermally without any sub-fragmentation. As mentioned above, this mechanism need only be realistic for a small number of haloes in order to reproduce the observations. Whether such a mechanism is at all realistic requires

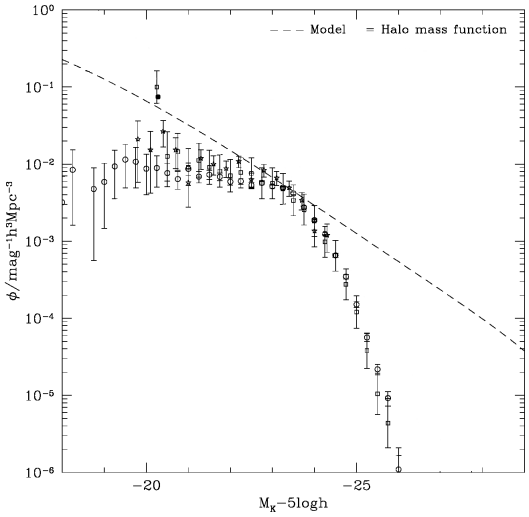

Figure 1.4: K-band luminosity function of galaxies. Circle, square and star points are from Cole et al. 2001, Kochanek et al. 2001 and Huang et al. 2003 respectively. The dashed line shows the result of converting the dark-matter halo mass function into a galaxy luminosity function by assuming a fixed mass-to-light ratio chosen to match the knee of the luminosity function (Fig. 1 from Benson et al. 2003 with adjustments).

more modelling in a cosmological setting. Nevertheless, by $z \sim 10$ most galaxies are expected to have SMBHs in their centre and, as we shall see, their activity can shape the properties of their host systems profoundly.

1.3.3 The luminosity functions of galaxies

A luminosity function is simply the number density over the absolute magnitude of some set of objects. The optical / NIR luminosity function is one of the most basic properties of the galaxy population and it contains many valuable clues to the process of galaxy formation and evolution. This is because the luminosity function does not simply trace the dark-matter halo mass function, implying that baryonic mass assembly involves physical processes which counteract the influence of gravity.

The measured K-band luminosity function of galaxies is shown in Fig. 1.4. It is clear that the halo mass function over-predicts the number of faint and bright-end galaxies, meaning

that we need physical mechanisms which reduce the number of low and high luminosity galaxies. These processes, which have the effect of preventing / delaying galaxy growth, are collectively termed *negative feedback*. Originally, it was thought that the shape of the luminosity function was regulated by the rate at which gas was able to cool in the parent dark-matter halo (Rees & Ostriker 1977; White & Rees 1978). In this picture, the sharp cutoff observed in the luminosity function was due to the long cooling times of gas in high-mass haloes. While the inclusion of such physics into the models was an improvement over the halo mass function, the overall fit was still poor. The introduction of photo-ionisation (which suppresses the formation of potential dwarf galaxies), stellar winds and supernovae feedback (which stunt the growth of small galaxies) were remarkably successful in reproducing the faint-end of the luminosity function (see Cole et al. 2000 and Benson et al. 2002). However, solving the faint-end problem in this way exacerbated the problem at the bright end; the ejected gas in massive haloes would eventually cool and lead to an excessive number of bright galaxies. Processes that would keep the gas from cooling, such as heat conduction near the centre of the halo or superwinds, had to be unrealistically efficient to account for the observations and were thus discarded (Benson et al. 2003). The conclusion was that the bright end could only be solved by tapping into the energy released by accretion onto SMBHs.

A mechanism which takes this idea further involves the use of the energy in radio jets to keep the halo environment hot and prevent gas cooling (e.g. Best et al. 2006). The sharp break at bright luminosities also suggests a preferred physical scale at which feedback would take place. Such a scale arises naturally from the interplay of two timescales: the time it takes for a gas particle to cool and the sound crossing time. If the sound crossing time is higher than the cooling time, then the gas particle is directly accreted onto the central host system. However, if the sound crossing time is lower than the cooling time, then the gas will be shock heated and transition into a state of hydrostatic equilibrium. This transition is

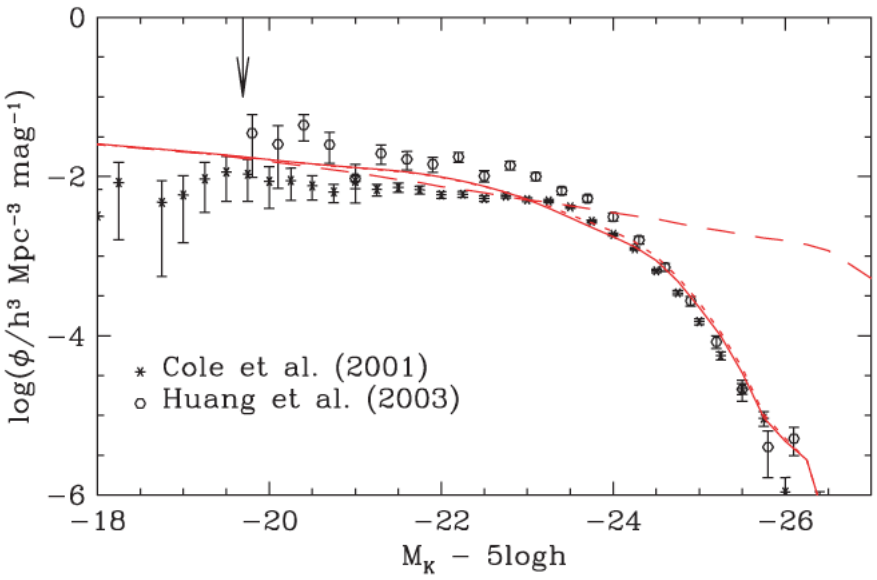

Figure 1.5: K-band luminosity function of galaxies in the local Universe (Fig. 3 from Bower et al. 2006). The solid and dashed red lines are the models with and without AGN feedback.

thought to occur at halo masses of $\sim 2\times10^{11}\,\mathrm{h}^{-1}\,\mathrm{M}_{\odot}$ (e.g. Dekel et al. 2009). Binney [2004] argued that the heat input from a central source can only be effective in the hydrostatic case. Therefore, this phase transition is believed to be the physical basis for understanding the break in the luminosity function, as radio-jet feedback is only effective in the presence of hot ionised gas.

In Fig. 1.5, a model which includes AGN feedback from Bower et al. [2006] is shown in red, against the measured K-band luminosity function in the local Universe. It is clear that the model does a good job of reproducing the observations (see also Bower, McCarthy & Benson 2008). However, AGN feedback is inserted in an unphysical way; if the Eddington luminosity from black-hole accretion is sufficient to offset gas cooling, the cooling flow is simply assumed to be quenched (in the hydrostatic case only). While the success of these models is encouraging, it is clear that a physical explanation supported by observational evidence will be needed in order to discover how the feedback mechanisms are working in reality.

1.4 Active Galactic Nuclei

1.4.1 A description of Active Galactic Nuclei

Active Galactic Nuclei are a class of object which reside in the centre of galaxies and contribute large amounts of power to the luminosity output at a wide range of wavelengths. Depending on the specifics of gas accretion onto the SMBH, excess emission may be observed in a wide variety of combinations, making a universal definition of AGN features difficult. However, it is still possible to distinguish two classes of AGN, defined *roughly* by the accretion efficiency; radiatively efficient and inefficient AGN may be crudely defined by whether the luminosity output due to AGN activity is above or below $\sim 1\%$ of the Eddington luminosity (defined as the maximum luminosity output a massive body can achieve in radiative equilibrium).

In the radiatively efficient case, an accretion disc forms which is optically thick, geometrically thin and surrounded by what is often referred to as a dusty 'torus' (e.g. Shakura & Sunyaev 1973; Novikov & Thorne 1973; Lynden-Bell & Pringle 1974). These sources fit into the unified scheme (see Fig. 1.6) in which the different properties exhibited by AGN are mainly due to the obscuring effect of the dusty torus (see Antonucci 1993, Urry & Padovani 1995 and Bianchi, Maiolino & Risaliti 2012 for reviews). Observational evidence suggests that a small fraction of these ($\sim$15-20%) are 'radio-loud', meaning that they have ratios of radio-to-optical (e.g. 5-GHz to B-band) flux above 10 (Kellermann et al. 1989). In all radiatively efficient AGN, the energy output from the accretion disc is radiated over a very broad range of frequencies and is expected to couple strongly to the gas inside the galaxy. Large-scale outflows and / or heating of gas and dust may be the result of such coupling (e.g. Cattaneo et al. 2009). This implies a quenching of star formation which then naturally sets up the tight relationships between galaxy properties such as the velocity dispersion / bulge mass and black-hole mass. In addition, the radio activity of radiatively efficient AGN may inject a

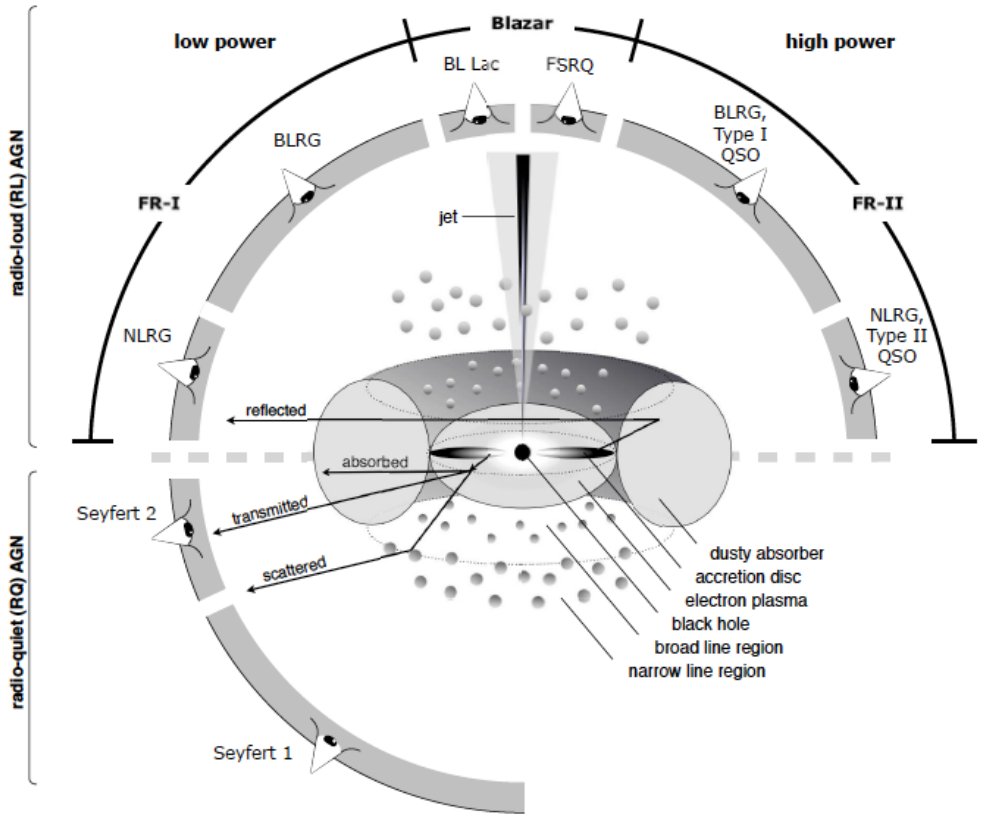

Figure 1.6: Schematic representation of our understanding of the AGN phenomenon in the unified scheme. The type of object we see depends on (1) the viewing angle, (2) whether or not the AGN produces a significant jet emission, and (3) how powerful the central engine is (Fig. 1 from Beckmann & Shrader 2013).

large amount of energy into the hot phase of the intergalactic medium (IGM), fundamentally changing the halo environment, and possibly, the nature of subsequent AGN activity (e.g. Rawlings & Jarvis 2004).

For radiatively inefficient AGN, accretion onto the black hole leads to very little radiated energy. However, those hosting jets and lobes may be identified at radio frequencies. These are thought to be fuelled by advection-dominated accretion flows (ADAFs; see Narayan, Mahadevan & Quataert 1998 for a review) which are optically thin and geometrically thick. However, the exact reason why some AGN are radio-loud and others are not is not well understood.

Fig. 1.6 is a good summary of the Unified Model. Blazars are a class of radio galaxies which are observed precisely 'face-on', appearing as bright point-like radio sources. Blazars may be split into two categories defined by whether they have strong emission lines: BL Lac's have weak emission lines while Flat Spectrum Radio Quasars (FSRQ) have strong emission lines. FSRQs will tend to appear like radiatively efficient accreting quasars if viewed at any other inclination angle, whereas BL Lacs will appear as radiatively inefficient AGN.

Broad and narrow line (BL and NL) AGN are defined by the line of sight to the broad and narrow line regions. BL regions are clumps of gas rotating rapidly around the accretion disc but not beyond the dusty tours. As such, the broad line profile observed in the optical spectra of AGN indicate either the absence of a dusty torus or an approximately 'face-on' line of sight. Such galaxies are often referred to as 'Type I QSOs'. NL regions are slower orbiting clumps of gas beyond the torus. Observations of exclusively narrow lines in the optical spectra of AGN suggest that the torus is obscuring the emission form the BL region. Such galaxies are often referred to as 'Type II QSOs'. Seyfert galaxies are a class of lower luminosity AGN which tend to be hosted by spiral galaxies. Although their accretion mechanism may be classified as radiatively efficient, the small amounts of gas accreted leads to less AGN emission than standard quasars. They are a relatively well studied population due to their ubiquity at low redshifts.

The Unification Scheme represented by Fig. 1.6 differentiates between high and low power radio sources. This division is more than just taxonomical, as it is thought to be related to the accretion efficiency which defines most of the AGN's emission profile. In the following section we discuss the evolution of AGN.

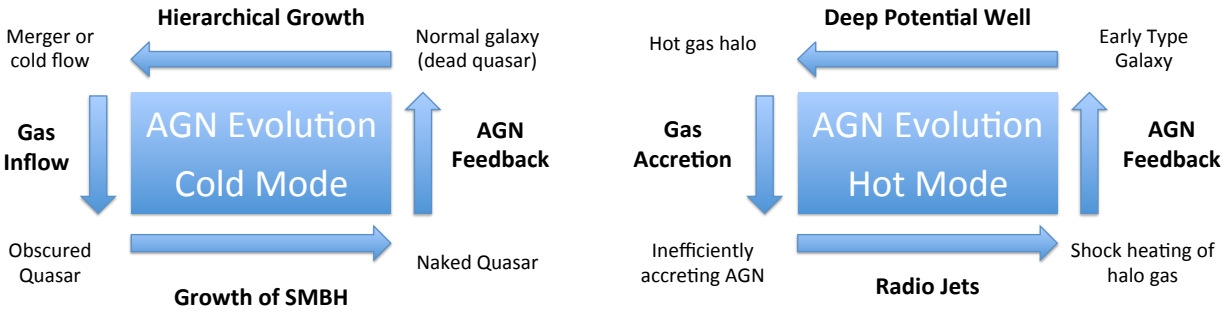

Figure 1.7: Schematic representation of the 'cold mode' and 'hot mode' cycle for AGN formation and evolution.

1.4.2 AGN evolution

The presence of SMBHs in the centre of most galaxies implies that nearly all galaxies have undergone a period of AGN activity. If this is the case, what are the details of the processes which transform quiescent galaxies to AGN and back again? Providing a unified picture of the evolution of any given AGN is difficult as the process is heavily reliant on the host's properties / formation history. Nevertheless, there are two scenarios which help explain this evolution in terms of repeatable 'cycles'; referred to here as the 'cold mode' and the 'hot mode' (see Marconi 2006; Croton et al. 2006; Hardcastle, Evans & Croston 2009).

In the case of the 'cold mode' (see left-hand side of Fig. 1.7), a triggering mechanism (possibly a gas-rich merger or the result of some disc instability) funnels cold gas into the central region, leading to radiatively efficient accretion. The initial phase of the accretion process is hidden from view by the large amounts of gas and dust covering the central region. During this period, the galaxy hosts an *obscured* AGN (e.g. Sanders et al. 1988). As the accretion rate increases, so does the radiative pressure. This makes it progressively more difficult for cold gas to continue fuelling the AGN, and eventually the fuelling is completely quenched. With the obscuring gas and dust cleared, the host now holds a 'naked quasar'. In the absence of fuelling gas, the quasar rapidly declines in brightness until it disappears

completely returning the host to a quiescent state. A host's AGN may be viewed at any point in this cycle and at any redshift below $z \sim 10$, although quasar activity is more prevalent at higher redshifts (peaking at $z \sim 2$; Boyle & Terlevich 1998). The ratio of obscured to unobscured quasars as inferred from the hard X-ray background may be as high as 4:1 (Comastri et al. 1995; Gilli, Salvati & Hasinger 2001; Gilli, Comastri & Hasinger 2007) and is probably due to the greater availability of gas and dust at high redshift and the longer lifetime an AGN is in the obscured state (e.g. Hopkins et al. 2006).

In the case of the 'hot mode' (see right-hand side of Fig. 1.7), no external triggering mechanism is required. Hot gas from the halo is believed to fuel radiatively inefficient AGN activity, which predominantly produce radio jets. As the AGN accretion intensifies, a similar pressure-fuel cycle is thought to occur, albeit at much lower luminosities and with a much lower amplitude (Allen et al. 2006). The radio jets and lobes help keep the halo gas hot, preventing the AGN from being fuelled by large amounts of condensed gas.

1.4.3 Radio galaxies

Radio galaxies are a class of object whose source of emission between 10 MHz and 100 GHz is predominately due to AGN activity. The dominant emission mechanism is synchrotron radiation; charged particles (mainly electrons, protons and positions) travelling at relativistic velocities gyrating in weak galactic / intergalactic magnetic fields. The precise details of the physical mechanisms which accelerates these particles are not well understood. As Fig. 1.6 suggests, radio AGN activity comes in many guises. Although the Unified Model provides a good picture of the parts which make up an AGN, it does not tell us which type of activity dominates at different masses and redshifts, or how radio AGN activity might evolve. It has long been known that radio galaxies tend to inhabit massive elliptical galaxies which are often characterised as having low star-formation rates and red optical colours (e.g. Matthews, Morgan & Schmidt 1964; Jarvis et al. 2001; Dunlop et al. 2003; Willott et al. 2003; Floyd

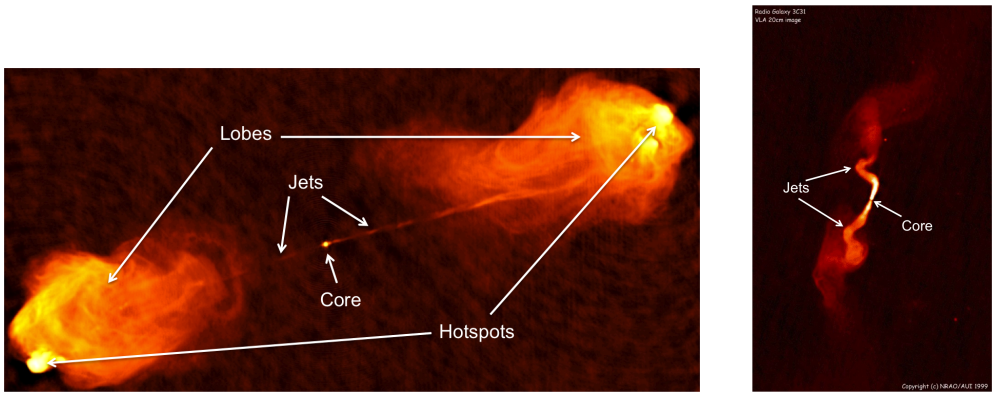

Figure 1.8: Left: Radio image at 4.8 GHz of Cygnus A, an FR II type source. Right: Radio image at 1.4 GHz of 3C31, an FR I type source. Both images were obtained using the Very Large Array and can be found at http://www.nrao.edu/imagegallery courtesy of NRAO/AUI.

et al. 2004; Best et al. 2005; El Bouchefry 2009). However, radio AGN activity has also been associated with slightly lower mass galaxies with much higher SFRs, blue optical colours and quasar-like emission features (e.g. Baldi & Capetti 2008). Understanding why and how the radio AGN population is divided is the topic of this section.

1.4.3.1 The structure of radio galaxies

The structure of radio sources may be split into two morphological classes: Fanaroff-Riley (FR) type I and type II (Fanaroff & Riley 1974). Examples of both types are shown in Figure 1.8. The radio emission from FR I type sources consist of a core and two bi-polar jets. These jets are poorly collimated becoming more diffuse further out. On the other hand, FR II type sources consist of highly collimated jets which terminate with hotspots at either end. These hotspots are what seed the lobes with plasma.

Observations of the cores of many AGN show a flat radio spectrum, in the sense that for the flux density as a function of frequency, we observe $F_\nu \propto \nu^\alpha$ with $\alpha \sim 0$. How may a flat spectrum be produced? The usually assumed jet acceleration mechanisms (i.e. shocks Fermi accelerating electrons) are very unlikely to produce flat spectrums. However, if the core is assumed to be optically thick, then the standard power-law distribution from synchrotron

emission is altered by radiating electrons re-absorbing some of the emitted photons. In other words, a turn over is observed towards lower frequencies resulting in each shock or knot producing a 'peaked spectrum.' If the plasma conditions are such that each knot peaks at roughly the same level, then summing the contributions from these knots produces a flat spectrum. This has become the standard model for interpreting the observations of flat radio spectra from jetted sources.

Radio lobes follow the much simpler synchrotron power-law spectrum, as the surrounding environment is usually optically thin. The exact slope of the spectrum depends on several factors, such as the age of the plasma (i.e. high energy electrons will radiate their energy at a higher rate than lower energy electrons) and the size of the lobes (i.e. as the lobes expand, the magnetic field decreases lowering the energy of the emitted photons), amongst others. Hotspots, which seed the lobes with plasma, usually have an SED which has a spectral index between that of the core and the lobes. Orientation also plays a part in what is observed. As one moves closer to looking down the jet, greater relativistic boosting of the core versus the lobes results in flat spectra being observed. Thus, angle at which a radio source is viewed can explain many of the observed spectral features.

1.4.3.2 Mass-dependencies of radio AGN and the K-z relation

The fraction of galaxies which show evidence for radio AGN activity is a strong function of stellar mass (see left-hand side of Fig. 1.9). It is interesting to ask whether this is simply the result of more massive galaxies hosting larger black-holes which then naturally produce more luminous radio-emission. On the right-hand side of Fig. 1.9 is a plot from Best et al. [2005], which shows the fraction of radio AGN activity as a function of stellar mass, where 'radio loud' is defined as radio luminosity per unit of stellar mass for a sample of radio galaxies with $z < 0.3$. If the mass-dependence of the radio emission is simply due to a linear relation with black-hole mass, one would expect a horizontal line; that the strong mass-dependence

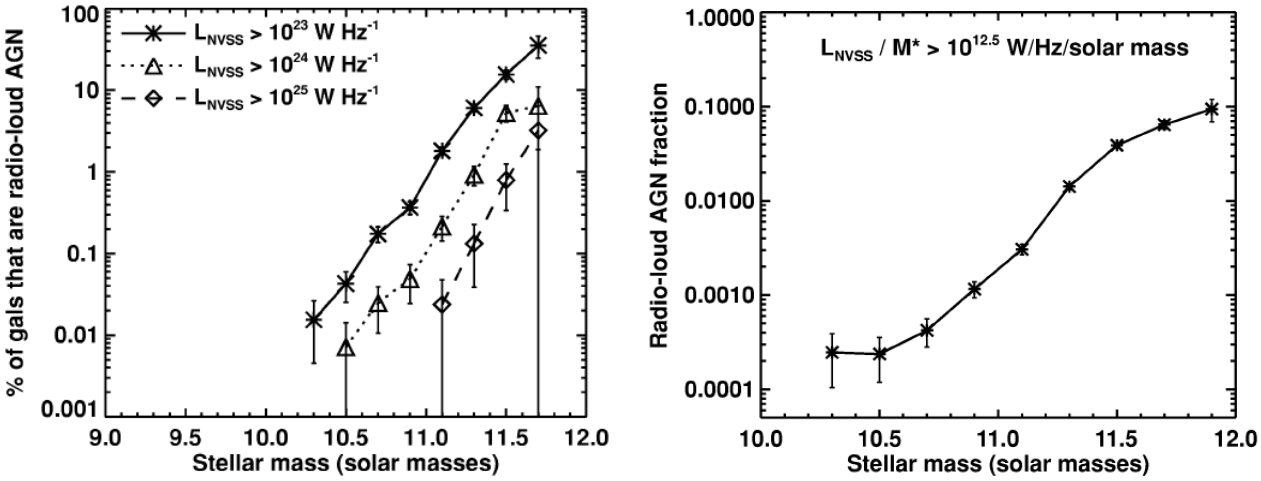

Figure 1.9: For sources $z < 0.3$; (left) the fraction of radio AGN as a function of stellar mass and (right) the fraction of radio-loud AGN as a function of stellar mass (left and right-hand side figures from Fig. 2 and 3 of Best et al. 2005, respectively).

remains suggests that either the mechanism responsible for radio emission does not scale linearly with black-hole mass or that a different accretion mechanism is responsible for radio emission in massive galaxies. Additionally, duty cycle and radio source size arguments have allowed rough lifetimes of radio sources to be calculated. These are thought to range between 10^{7-8} years (e.g. Bird, Martini & Kaiser 2008; Antognini, Bird & Martini 2012) for typical FR II type sources, and somewhere below this for typical FR I type sources.

Deep near-infrared surveys of radio galaxies indicate that at high redshift, they are also the most massive systems of their epochs (De Breuck et al. 2002). Remarkably, a tight relation exists between the apparent K-band magnitude of radio galaxies and redshift (see Fig. 1.10; note the sample of radio galaxies used is flux density limited and complete). Such a relation is only possible if the luminosity of a class of object remains approximately the same over several billions of years. The near-infrared K-band emission from radio galaxies is dominated by old stellar light (Best, Longair & Röttgering 1998; Simpson, Rawlings & Lacy 1999), implying that the stellar mass of the most powerful radio AGN remains approximately constant. In other words, most of the stellar mass build up in massive radio galaxies is

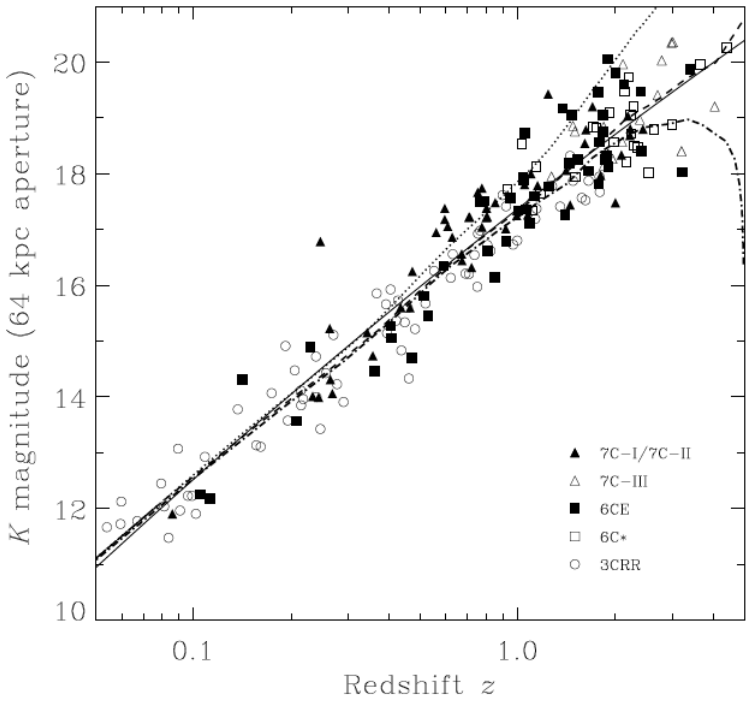

Figure 1.10: K-band magnitude versus redshift for several complete samples of radio galaxies. The solid black line is the best-fitting second-order polynomial for all the data (Fig. 2 from Willott et al. 2003).

thought to have occurred at very high redshift ($z \gtrsim 5$; Willott et al. 2003; van Breugel et al. 1998). Although, perhaps a more realistic interpretation involves massive ellipticals migrating onto the K-z relation after reaching the limit of their stellar mass growth, a point determined by feedback mechanisms. The solid line in Fig. 1.10 is the best-fitting second-order polynomial for all the data, the result of which is shown below.

$$K = 17.37 + 4.53 \log_{10} \mathrm{z} - 0.31 (\log_{10} \mathrm{z})^2 \tag{1.7}$$

The dashed line in Fig. 1.10 is the K-magnitude evolution of a galaxy of local luminosity $3\,L^*$ which forms all of its stars instantaneously at $z = 10$. The remarkable agreement between the solid and dashed lines reinforces the idea that powerful massive radio galaxies produced the majority of their stars at high redshift.

1.4.3.3 High and low excitation radio galaxies

The optical spectra of radio galaxies was split at a very early stage into two classes: Class A contained high-ionisation lines while Class B contained absorption-lines and / or very weak emission-lines (Hine & Longair 1979; Heckman et al. 1986). This classification has evolved into what is now referred to as 'High Excitation Radio Galaxies' (HERGs) for Class A and 'Low Excitation Radio Galaxies' (LERGs) for Class B (Jackson & Rawlings 1997; Buttiglione et al. 2010; Cid Fernandes et al. 2010; Baldi & Capetti 2010). Details of what constitutes a LERG / HERG differ but generally rely on the values of a combination of line ratios (e.g. H_α, H_β, [OIII], [OI], [NII] and [SII]; see Buttiglione et al. 2010), and equivalent width measurements of key lines such as [OIII] (c.f. Tadhunter et al. 1998). The presence (or lack thereof) of high-ionisation lines is indicative of the type of nuclear activity in the host. HERGs / LERGs are thought to contain radiatively efficient / inefficient AGN respectively. HERGs have lower 4000 Å break strengths, bluer optical / UV colours and higher FIR luminosities than LERGs, all suggesting higher SFRs (Baldi & Capetti 2008; Herbert et al. 2010; Best & Heckman 2012; Janssen et al. 2012; Hardcastle et al. 2013). LERGs also tend to be hosted in the most massive galaxies, while HERGs tend to be hosted in galaxies with a much broader range of masses (e.g. McLure et al. 2004). LERGs dominate the radio luminosity function to 1×10^{26} W Hz^{-1} (at 1.4-GHz), after which HERGs begin to dominate (Best & Heckman 2012). It must be noted that many of the differences between HERGs and LERGs have been shown for large samples at relatively low redshifts. Large fractions of HERGs have also been associated with disturbed morphologies indicating recent galaxy interactions (e.g. Ramos Almeida et al. 2011). These differences, taken together suggest that HERGs and LERGs are objects with very different galaxy properties and formation histories. Understanding the source of this difference is the subject of the next section.

1.4.3.4 The environment and fuelling mechanism of radio AGN

Radio-loud AGN tend to be found in denser environments (Best 2000; Best et al. 2005; Galametz et al. 2012a; Wylezalek et al. 2013). This is partly due to the fact that clustering is a strong function of stellar mass (Worpel et al. 2013). In addition, the hot-hydrostatic shock-heated environments of massive galaxies / clusters of galaxies are good at confining radio lobes, boosting the observed flux and therefore the detection rate (e.g. Barthel & Arnaud 1996; Tadhunter et al. 2011). However, the importance of a radio galaxy's environment may be more fundamental; it may determine the fuel source, and therefore the accretion mechanism of radio AGN (Hardcastle, Evans & Croston 2007).

The phase transition in the environment of galaxies (e.g. between the non-hydrostatic and hydrostatic cases) fundamentally alters the properties of the gas in the halo. In the non-hydrostatic case, cold gas is able to flow largely unimpeded into the host and therefore to the SMBH, triggering bright quasar-like activity. However, in the hydrostatic case the cold gas is shock heated. This restricts the fuel source of SMBHs to very hot gas ($> 10^6$ K) preventing radiatively efficient accretion from occurring. Only relatively inefficient spherical Bondi / ADAF accretion of hot gas is possible unless cold gas is carried into the centre of the cluster by a major merger or some other secular process. This type of accretion has been associated with radio lobes which are subsequently confined by the halo gas, shock-heating it and preventing strong cooling flows from developing after approximately the free-fall time of the halo gas. Much of the recent observational work on radio galaxies attempts to elucidate aspects of this feedback cycle. For example, it has been shown that the time averaged mechanical energy output from the radio jets of most early-type galaxies is sufficient to balance gas cooling from the hot phase of the IGM (Best et al. 2006; Best et al. 2007). In addition, there is evidence for a tight correlation between the Bondi accretion rate (inferred from X-ray data) and the power emerging from these systems in relativistic jets (e.g. Allen et al. 2006); this suggests that, in at least some massive galaxies, the fuelling mechanism is

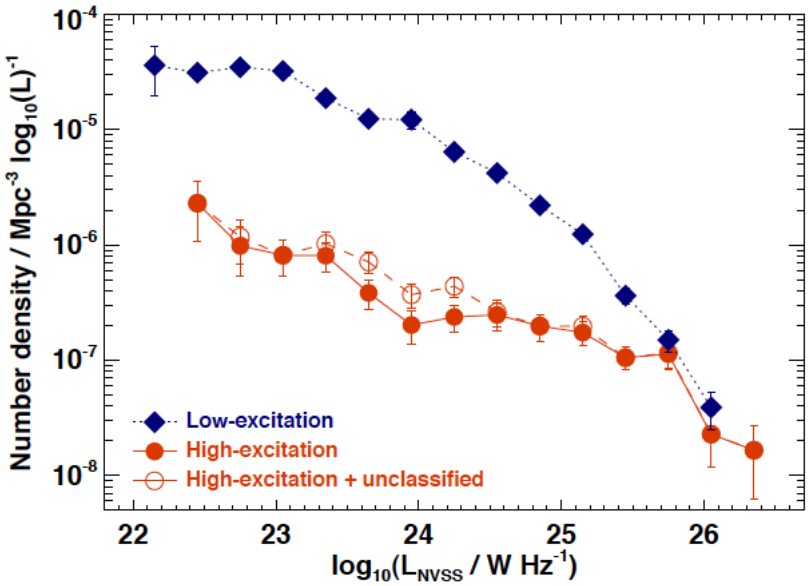

Figure 1.11: The number density as a function of radio luminosity for a sample of HERGs and LERGs below $z = 0.3$ (Fig. 4 from Best & Heckman 2012).

linked to the AGN activity.

Merging galaxies, which form a second important source of cold gas are likely to have their cold gas and dust content stripped by hot gas environment en route. Thus, the type of environment a radio galaxy inhabits may determine many of the host's properties.

1.4.3.5 A model for the describing the properties of radio AGN

It is clear that the properties of the hosts of radio AGN are varied and complex, yet a clear synthesis of these properties is now possible. At low radio luminosities, radio galaxies are dominated by LERGs (see Fig. 1.11). These have inefficiently accreting black holes with the central region contributing little from the X-ray to the far-infrared. LERGs are argued to be fuelled by the hot phase of the IGM via ADAF / Bondi accretion (Hardcastle, Evans & Croston 2007). This limits LERGs to the hottest, densest and richest environments most easily provided by the halos of massive ellipticals (Kereš et al. 2005; Dekel & Birnboim 2006).

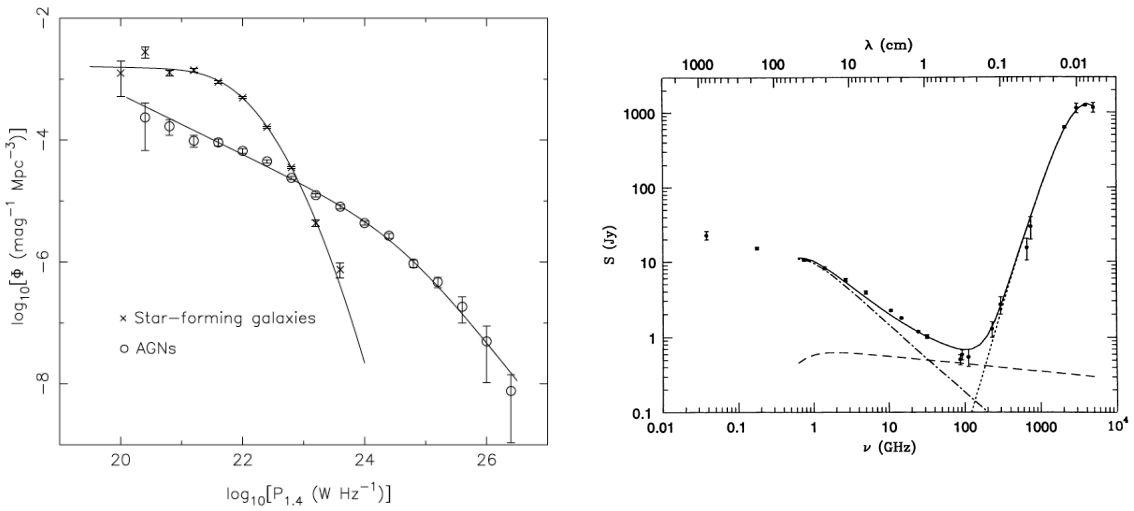

Figure 1.12: The local 1.4-GHz luminosity function for star-forming galaxies and radio AGN in the local Universe (left; Fig. 12 from Mauch & Sadler 2007). The observed radio / FIR spectrum of M82 (right). The solid line is the sum of the synchrotron (*dot-dashed line*), free-free (*dashed-line*) and dust (*dotted line*) components (Fig. 1 from Condon 1992).

At higher radio luminosities ($> 1\times10^{26}$ W Hz^{-1} at 1.4-GHz), the radio-source population is dominated by HERGs, although there is still significant overlap with LERGs. The high-excitation lines in the optical spectra of these galaxies imply a fundamentally different type of accretion mechanism (i.e. quasar-like) activity from that of LERGs. HERGs are fuelled by cold gas transported to the central regions by what are, presumably, on-going gas-rich mergers or cold flows. The nature of the fuelling mechanism allows HERGs to occupy a much broader mass range than LERGs, and in particular they are not expected to be restricted to the most massive galaxies.

1.5 Radio-selected star-forming galaxies

Star-forming galaxies dominate the radio luminosity function below $P_{1.4} = 1\times10^{23}$ W Hz^{-1} (Sadler et al. 2002; Mauch & Sadler 2007; see left-hand side of Fig. 1.12). They are characterised by their blue optical colours which are indicative of a young stellar population and

their high level of far-infrared emission. In terms of radio emission at $\sim$1 GHz, around 90% comes in the form of synchrotron radiation with the other 10% coming from thermal free-free emission originating from H_{II} regions (see right-hand side of Fig. 1.12). The relativistic electrons needed for synchrotron radiation are accelerated in the supernova remnants of the most massive stars ($M > 8M_{\odot}$) and therefore trace relatively recent star-formation (the life-time of such massive stars is $< 3 \times 10^7$ yr and these relativistic electrons have lifetimes of $< 10^8$ yr; Condon 1992). Radio surveys will therefore select the most actively star-forming galaxies, although the sensitivity of the current generation of all sky surveys (e.g. NVSS and FIRST) are such that only low redshift ($z < 0.2$) star-forming sources are detected.

1.6 Infrared astronomy

The IR regime covers wavelengths from $\sim$ 1-1000 μm. Within this spectral range, the near-IR (NIR) covers wavelengths of 1-5.0 μm, the mid-IR (MIR) covers wavelengths of 5-25 μm, the far-IR (FIR) covers wavelengths of 25-500 μm and the sub-mm covers wavelengths of 500-1000 μm, although these are not strict definitions. In the following section, we discuss the characteristics of IR sources through the advances made by key IR telescopes.

1.6.1 The *Infrared Astronomical Satellite* (*IRAS*)

The first all-sky survey at mid and far-IR wavelengths was carried out in 1983 by the *Infrared Astronomical Satellite* (*IRAS*) at wavelengths of 12, 25, 60 and 100 μm with a sensitivity of a few hundred mJy. The maps provided by *IRAS* led to the detection of tens of thousands of galaxies, the majority of which had not been observed before. The discovery of so many far-IR sources led to the development of the terminology and classification scheme shown in Table 1.1 (see Sanders & Mirabel 1996 and references therein for an early review of IR galaxies). The major conceptual advance from *IRAS* came from the realisation that the spec-

F_{fir}	1.26×10^{-14} $\{2.58\ f_{60}$ + $f_{100}\}$ [W m^{-2}]
F_{ir}	1.8×10^{-14} $\{\ 13.48 f_{12} + 5.16 f_{25} + 2.58 f_{60} + f_{100}\ \}$ [W m^{-2}]
L_{ir}	L(8-1000 μm) = 4π D$_L^2$ F$_{ir}$ [$L_\odot$]
LIRG	Luminous Infrared Galaxy, $L_{ir} > 10^{11}\ L_\odot$
ULIRG	Ultra Luminous Infrared Galaxy, $L_{ir} > 10^{12}\ L_\odot$
HyLIRG	Hyper Luminous Infrared Galaxy, $L_{ir} > 10^{13}\ L_\odot$

Table 1.1: Common, although not exclusive abbreviations and definitions for some IR parameters. f$_{12}$, f$_{25}$, f$_{60}$ and f$_{100}$ are flux densities from the *IRAS* bands (from Sanders & Mirabel 1996).

tral energy distribution (SED) of most galaxies were well fitted by a black-body spectrum indicating that thermal dust was the origin of the emission. A modified version of the Planck law was introduced to model these SEDs and took the following form,

$$B_v(T) = \frac{2h\nu^{3+\beta}}{c^2} \frac{1}{e^{\frac{h\nu}{k_B T}} - 1}, \tag{1.8}$$

where T represents the isothermal temperature of the source, k is the Boltzmann constant and h is the Planck constant. The model varies from the traditional Planck law as it contains the parameter, β, which encodes information relating to the dust grain composition and size. Although *IRAS* managed to constrain dust temperature for the first time, the wavelength coverage meant that warm-IR sources were preferentially selected (i.e. > 60 K). In addition, *IRAS* was only sensitive to relatively bright sources which limited the source population to low redshifts (i.e. $z < 0.1$).

Having established the ubiquity of IR sources, attention soon turned to the mechanism responsible for heating the dust. It became clear that the luminous IR sources were associated with indicators of high SFRs, suggesting that star formation played a key role in heating the dust (e.g. Soifer et al. 1987; Sanders & Mirabel 1996). Star formation provides a plausible mechanism for heating interstellar dust, as UV photons are approximately the same wavelength / size as dust grains. This allowed for the first conversions of IR luminosity to SFR (e.g. Kennicutt 1998b and more recently Kennicutt et al. 2009; Calzetti 2012). Such

conversions were only appropriate for non AGN dominated galaxies because the accretion discs of AGN are known to heat the surrounding dusty torus. This dust can be heated to a thousand kelvin which results in strong emission at mid-IR wavelengths; this means that the derived SFRs would be biased upwards if the AGN component was not taken into account. The lack of coverage at wavelengths $> 100\,\mu$m made the separation of both components difficult.

IRAS observations of radio galaxies were limited by their high redshifts. Nevertheless, early results showed that high-powered radio galaxies tended to be detected at far-IR wavelengths whereas low-powered radio galaxies were not (e.g. Golombek, Miley & Neugebauer 1988; Impey & Gregorini 1993). In addition, the IR luminosity seemed to correlate well with the presence of strong optical emission lines, consistent with the current view that such galaxies have the properties generally associated with HERGs.

1.6.2 *ISO* and *Spitzer*

The *Infrared Space Observatory* (*ISO*; Kessler et al. 1996) was launched in 1995 and carried high resolution spectrometers and photometers which were many times more sensitive than those carried by *IRAS*. In total, the wavelength range extended from 2.5 to 240 μm. Results from targeted observations of radio galaxies continued to support the view that unification schemes could successfully explain the FIR properties of quasar-like radio galaxies, whereas more traditional massive elliptical radio galaxies continued to show low levels of FIR emission (Meisenheimer et al. 2001; Haas et al. 2004; Müller et al. 2004).

In 2003, the *Spitzer Space Telescope* (*SST*, but commonly referred to as *Spitzer*; Werner et al. 2004) was launched. It carried three instruments; the Infrared Camera Array (IRAC; 3.6-8.0 μm; Fazio et al. 2004), the Infrared Spectrograph (IRS; 5.3-40.0 μm; Houck et al. 2004) and the Multiband Imaging Photometer for Spitzer (MIPS; 24-160 μm; Rieke et al.

2004). The IRAC bands were particularly useful for the characterisation of the rest-frame optical / NIR SED of high-redshift radio-galaxies (e.g. Seymour et al. 2007). In addition, radio sources which were not detected in deep K-band surveys (e.g. Reuland et al. 2003) could be targeted with IRAC, allowing an extremely obscured population of radio galaxies to be selected and studied for the first time (e.g. Martínez-Sansigre et al. 2005; Martínez-Sansigre et al. 2006a,b). The properties of a similarly selected sample of radio sources is the focus of Chapter 5 of this thesis.

1.6.3 The *Herschel Space Observatory* (*HSO*)

The data which have enabled the far-infrared properties of radio galaxies to be constrained (the main subject of this thesis) came from the *Herschel Space Observatory* (*HSO*). Therefore, in this section I will describe the instrumentation aboard the *HSO* in so far as it pertains to this thesis. I will also describe the survey details whose data have been used throughout this thesis. Initial results from the *HSO* will also be covered.

1.6.3.1 *HSO* instrumentation and the *Herschel*-ATLAS

The *HSO* was launched in May 2009 reaching the second Lagrangian point two months later. The *HSO* carried three instruments; the Photo-detecting Array Camera and Spectrometer (PACS; Poglitsch et al. 2010), the Spectral and Photometric Imaging REceiver (SPIRE; Griffin et al. 2010) and the Heterodyne Instrument for the Far Infrared (HIFI; de Graauw et al. 2010). In this thesis, no data from HIFI is used; therefore we will not discuss its instrumentation. PACS and SPIRE have both cameras and spectrometers. PACS covers wavelengths from 55-210 μm. The imaging camera can image simultaneously in two bands (centred either on 70 / 100 μm and 160 μm). SPIRE instrumentation covers the wavelength range from 194-672 μm. The imaging bands are centred at 250, 350 and 500 μm.

The *Herschel*-Astrophysical Terahertz Large Area Survey (H-ATLAS; Eales et al. 2010a)

was submitted for consideration as part of the Guaranteed Time Key Programmes process. The proposal was successful and data was taken for the project soon after launch. Prior to the *HSO*, most of the wave-band between 100-500 μm was uncharted. This meant that knowledge of cold low-to-medium redshift ($z < 0.5$) sources was virtually non-existent. Therefore, the primary goal of the H-ATLAS was to provide a census of the dust in the low-to-medium redshift Universe. This was only possible through a relatively high-resolution, unbiased large-area-survey utilising the wavelength coverage offered by PACS and SPIRE. The programme aimed to map ~ 150 sq degrees of the northern sky (known as the Northern Galactic Plane; NGP), ~ 262 sq degrees of the southern sky (known as the Southern Galactic Plane; SGP) and 138 sq degrees of equatorial sky (known as the GAMA[1] or Phase 1 area), giving a total coverage of 550 sq degrees. These fields were mapped at 100 and 160 μm using PACS and 250, 350 and 500 μm using SPIRE with sensitivities of 132, 121, 33.5, 37.7, 44.0 mJy, respectively (Pascale et al. 2010; Ibar et al. 2010). In this thesis, I only use data from the equatorial fields.

1.6.3.2 Some relevant results from the *HSO*

In this section I discuss some of the initial results from the *HSO* which relate to this thesis. Most of the results discussed here are derived from two extra-galactic surveys; the *Herschel*-ATLAS and the *Herschel* Multi-tiered Extragalactic Survey (HerMES; Oliver et al. 2012) which is a deep survey of ultra-deep fields.

As stated above, the primary goal of the H-ATLAS was to provide a census the dust properties of the nearby Universe. Dunne et al. [2011] studied a large sample of 5σ detected sources at 250 μm with SDSS counterparts and found that the dust mass function shows strong evolution out to $z = 0.4 - 0.5$ (See Fig 1.13). In terms of dust mass, this corresponds to a factor of 4-5 increase in the dust masses of the most massive galaxies.

[1] Galaxy Mass And Assembly survey; Driver et al. 2009

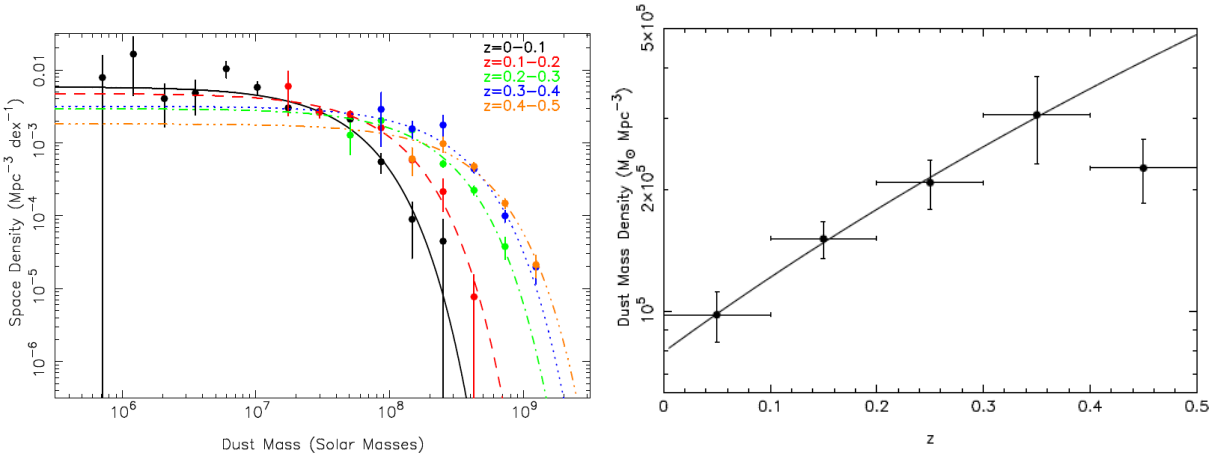

Figure 1.13: Dust mass function split into 5 redshift bins (left). Integrated dust mass density as a function of redshift for H-ATLAS detected galaxies (right). The best fitting line (which excludes the last data point due to completeness issues) is $\rho_d \propto (1+z)^{4.5}$. Fig. 9 and Fig. 17 from Dunne et al. 2011.

A thorough study of the submm properties of optically-selected galaxies below redshift 0.35 was performed by Bourne et al. [2012]. Some of the results are listed below. (1) All but the most massive galaxies are below the formal 5σ detection limit in the H-ATLAS maps. (2) The sub-mm luminosity is a strong function of optical colour, with red galaxies being up to an order of magnitude less luminous at 250 μm than blue galaxies of the same stellar mass. (3) Dust temperatures for blue galaxies are a strong function of stellar mass (rising from 11 K to 28 K) whereas red galaxies are clustered around $\sim$ 16 K for all masses. The temperature variation can account for much of the luminosity difference seen between red and blue galaxies.

The addition of photometry beyond 100 μm resulted in the detection of a population of galaxies with very cold dust temperatures missed by *IRAS* (Amblard et al. 2010; Hwang et al. 2010; Magdis et al. 2010). In addition, little temperature evolution was observed, consistent with the results presented by Smith et al. (*submitted*).

1.6.3.3 The far-infrared-radio correlation

There is a remarkably tight correlation between the FIR / sub-mm output of star-forming galaxies and the radio luminosity (Helou et al. 1988; Helou, Soifer & Rowan-Robinson 1985; Appleton et al. 2004). It is generally defined in terms of a constant value of the logarithm of the ratio of the infrared and radio luminosity. The origin of this relation is thought to be due to massive stars heating interstellar dust and accelerating electrons to relativistic velocities when they eventually explode as supernovae (Harwit & Pacini 1975). The real significance of the far-infrared-radio-correlation (FIRC), that it is so tight and so universal, was not appreciated until the advent of *IRAS*. Condon [1992] suggested that this tight FIRC could be used to distinguish star-forming galaxies from radio AGN. Such an approach is used throughout this thesis to distinguish between both populations.

The FIRC has been investigated using *Herschel*. Jarvis et al. [2010] selected a sample of radio galaxies with $z < 0.5$ in the H-ATLAS Science Demonstration Field (a subset of the 9^{hr} equatorial field) and found that it held at 250 μm. Moreover, no evolution was found for the redshift range under study. This is consistent with the results of Ivison et al. [2010] who studied the FIRC in the HerMES fields. For an in-depth study of the FIRC using PACS and SPIRE data for a single galaxy, see Tabatabaei et al. [2013]. The initial *Herschel* results concerning AGN are deferred to the introduction of Chapter 3.

1.7 Outline of thesis

The primary aim of this thesis is to characterise the FIR properties of radio galaxies across cosmic time. This involves probing the low, medium and high-redshift epochs and investigating which parameters control the FIR luminosities and dust temperatures of radio galaxies. As mentioned above, radio galaxies are thought to play a fundamental role in the evolution of the galaxy population, particularly at the bright end of the luminosity function. The FIR

offers us a unique view into the general properties of the ISM which the radio jets must alter, either directly or indirectly, if radio AGN feedback is at least partly responsible for downsizing.

In Chapter 2, I describe the construction of the radio catalogue from which the subsequent chapters draw their radio sources. I detail which surveys were used and why, as well as the biases present in the sample. In Chapter 3, I investigate the low-to-medium redshift radio-source population and attempt to determine which parameters control the FIR luminosity output of radio galaxies. I also search for observational evidence of radio-AGN feedback on the ISM via the FIR luminosity. In Chapter 4, I perform an in-depth study of the dust temperature distribution and evolution of the same radio sources and attempt to link the results with the presence of radio jets. In Chapter 5, I present a method for finding high-z, star-bursting radio AGN, which will be useful for determining the existence, frequency and nature of direct radio-AGN feedback. Finally, in Chapter 6, I summarize the main results of this thesis and end with a discussion of where the field can move on from here.

Chapter 2

The 1.4-GHz radio catalogue

In this chapter, I present the radio catalogue that forms the basis of the work presented in Chapters 3, 4 and 5. The radio catalogue was created over the *Herschel*-ATLAS phase 1 area (see Fig. 2.1) using a combination of 1.4-GHz continuum radio data and near-IR photometry. The goal was to match any observed radio emission to counterparts in the K-band; if this was not possible, then a best estimate of the positional origin of the radio emission was used. This was done in order to create a radio sample with which the H-ATLAS datasets could be exploited. This chapter is structured as follows. In Section 2.1, I describe which data were used and why. In Section 2.2 and 2.3 I describe the matching method, followed by some examples in Section 2.4. Finally, in Section 2.5 and 2.6 I describe some general catalogue statistics and the robustness of the catalogue.

2.1 The data

In this section, I describe how the radio catalogue was built. I started with three sets of survey data:

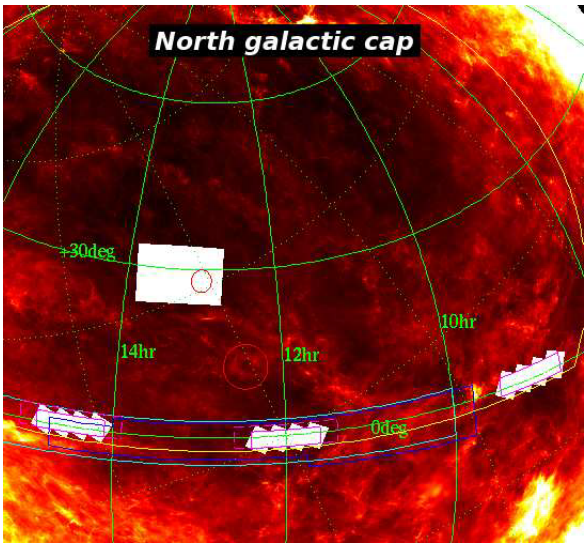

Figure 2.1: Coverage of the H-ATLAS in the northern and equatorial fields. The three equatorial fields comprise the phase 1 / GAMA area. Note that the coverage of the first data release of the phase 1 area (v1) is used in this thesis and contains only half of the 12^{hr} field (Fig. 2 of Eales et al. 2010a).

1. **NRAO VLA Sky Survey** (NVSS): The NVSS is a 1.4-GHz continuum survey covering the entire sky north of -40 degrees in declination. The survey was carried out at the Very Large Array (D and DnC configurations) over a period of 4 years and was completed in 1997. The FWHM of the beam is $45''$ and the rms of the survey is 0.45 mJy. The 90% positional confidence level for sources above 2 mJy is $\sim 10''$ and goes down to a few arcseconds for sources above 10 mJy (see Condon et al. 1998 for more survey details).

2. **Faint Images of the Radio Sky at Twenty-Centimeters** (FIRST): The FIRST survey is a 1.4-GHz continuum survey carried out at the Very Large Array (B configuration). The survey began in 1993 and by 2001, it had mapped the nearly all of the northern sky above -10 degrees in declination and between 8^{hr} and 17^{hr} in right ascension. The FWHM of the FIRST beam is $\sim 5''$, a 9-fold improvement in resolution over the NVSS. The rms of the survey is 0.2 mJy and the 90% positional confidence level for

sources above 1 mJy is $\sim$ 1″ (see Becker, White & Helfand 1995 for more survey details).

3. **The UKIRT**[1] **Infrared Deep Sky Survey** (UKIDSS) **Large Area Survey** (LAS): The UKIDSS LAS (hereafter, simply LAS) is a near-IR survey which covers approximately 4000 sq. degrees of the northern and equatorial sky. The survey mapped these areas in the Y, J, H and K bands which have central wavelengths of 1.03, 1.25, 1.63 and 2.20 μm respectively. The depth of the LAS survey in the K-band is 18.0 magnitudes[2] (see Lawrence et al. 2007 for more survey details).

The NVSS and FIRST surveys cover the H-ATLAS phase 1 area completely. However, the LAS covers 95.6% of the phase 1 area. Therefore, radio sources outside this area are not included in the radio catalogue as NIR counterparts could not be identified.

2.2 NIR-radio overlays

The NVSS formed the basis of the radio catalogue. This is because the NVSS's compact configuration makes it sensitive to diffuse radio emission which would otherwise be missed by the FIRST survey. It also makes for easier identification of core and lobe components for sources with large projected sizes across the sky. However, due to NVSS's large beam, cross matching it directly with the LAS K-band catalogue would result in a large number of false identifications. For this reason FIRST data, with its high angular resolution, is used to help identify the origin of the radio emission. One of the most effective ways to ensure the completeness and reliability of NIR-radio matches is by constructing a list of possible identifications, and then verifying each one visually using overlays of radio contours on NIR images. In Fig. 2.2, an example which demonstrates the need to use a combination of NVSS

[1] United Kingdom Infrared Telescope: http://www.jach.hawaii.edu/UKIRT/
[2] All magnitudes in this thesis are in Vega

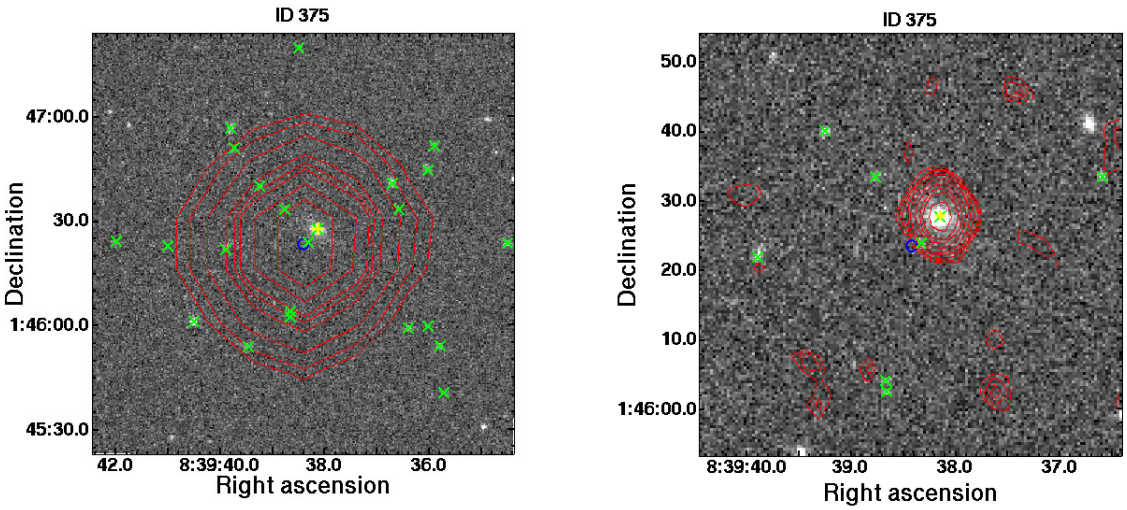

Figure 2.2: K-band NVSS overlay (left). The NVSS contours are shown in red. The contour levels are as follows: (0.4, 0.5, 0.7, 1.0, 1.5, 2.0, 2.5, 3.5) mJy / beam. The blue circle is the position of the NVSS source while the yellow '+' sign marks where a FIRST detection is present. The green crosses are formal LAS K-band detections. K-band FIRST overlay (right). The FIRST contours are shown in red. The contour levels are as follows: (1, 1.3, 1.8, 2.5, 2.8, 3.0, 3.5, 4, 5) mJy/beam. The flux density of the source shown here is $S_{1.4\mathrm{GHz}} = 5.2\,\mathrm{mJy}$.

(left) and FIRST (right) data is shown; the sizes of the overlays using the NVSS and FIRST data are $2' \times 2'$ and $1' \times 1'$, respectively.

Several interesting features are immediately apparent. Firstly, while the position of the NVSS source is $5.9''$ from that of the FIRST source, they are clearly the same radio source. Secondly, with its higher angular resolution the FIRST data has successfully identified the host of the radio emission in the K-band image. If the NVSS and LAS catalogues had been matched on a simple 'best match' algorithm the wrong K-band source would have been identified. An additional benefit of creating overlays is the ability to search for other radio components which may, or may not, be related to the K-band counterpart. In this image, there is no evidence for additional radio components as the rest of the FIRST field is blank and there are no signs of extended emission in the NVSS contours.

For these reasons (and others which will be explored in the next section), all the catalogued NVSS sources in the phase 1 area are identified visually (i.e. using overlays).

2.3 Classification scheme

In this section my approach to cataloguing the radio sources will be described. The fundamental goal was to assign the best possible position to all the radio sources, given the data. A flow diagram of the logic used is shown in Fig. 2.3.

The first question which was asked was; do the radio contours show evidence for radio emission outside of the NIR-NVSS overlay? For the vast majority of the overlays, the $2' \times 2'$ NIR-NVSS overlays were sufficiently large to encompass all the radio emission. If this was not the case, a larger image which encompassed all the radio emission was created. Next, I determined whether the NVSS radio emission had one or more hosts. If multiple hosts were identified, then the radio flux density as measured by the NVSS needed to be partitioned. This was done by calculating a ratio for every source; the integrated FIRST flux density of that source divided by the total integrated FIRST flux density in the image. This ratio was then multiplied by the total NVSS flux density, giving one an estimate of the flux density for that source. This procedure was repeated for all 'blended' sources. After this correction, the presence of a K-band counterpart was searched for; where there was more than one potential LAS ID, the closest K-band source to the FIRST position was chosen. In addition, K-band magnitude information was taken into account (i.e. brighter sources were matched preferentially to fainter ones). In the case of compact radio sources, no LAS source more than $2.5''$ away was selected as a counterpart. If a K-band counterpart was found, the position of the radio source was replaced by that of the catalogued LAS position, and the K-band magnitude added to the catalogue. If no K-band counterpart was found, then the

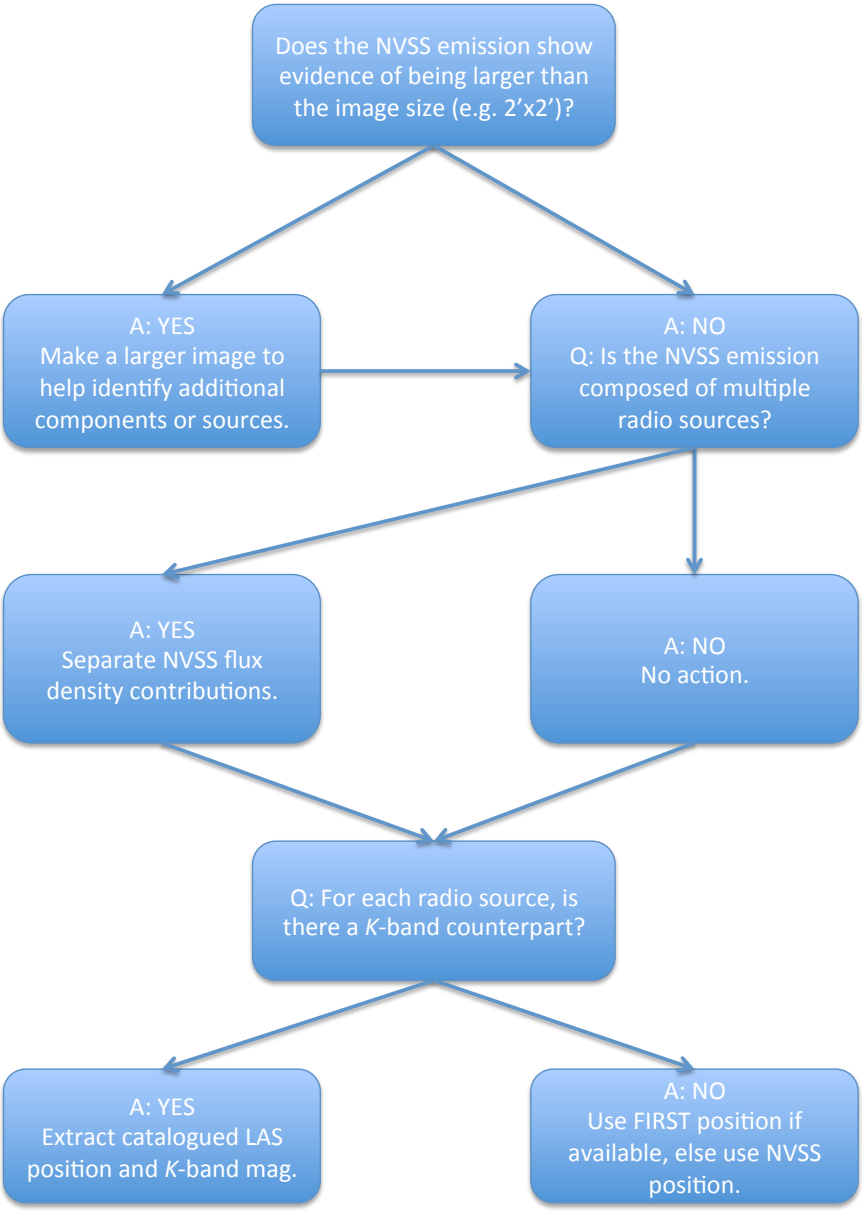

Figure 2.3: The classification scheme used on NIR-radio overlays to extract accurate source positions and matches.

FIRST position was used, or in the case that the source was diffuse, the NVSS position.

2.4 Some examples

In this section, I use the classification logic developed in Section 2.3 on four overlays in order to show how the classification method works in practice.

ID 4: The NIR-NVSS and the NIR-FIRST overlays are shown on the top left and right-hand sides of Fig. 2.4, respectively. There is no evidence for any extended emission. Moreover, there are no additional FIRST detections beyond the two present in the NVSS-NIR overlay. In this image, it is clear that both FIRST detections have similar integrated flux densities, suggesting that both sources are not independent of one another. The fact that the NVSS position, which accounts for all the flux in the image, falls onto a K-band source strongly suggests that this is a double-lobed radio source. The NIR position and K-band magnitude of the source closest to the NVSS position was used in the 'processed' radio catalogue. This source has a flux density of $S_{1.4\,\mathrm{GHz}} = 315.4\,\mathrm{mJy}$.

ID 20: The NIR-NVSS and the NIR-FIRST overlays are shown on the bottom left and right-hand sides of Fig. 2.4, respectively. There is no evidence for any extended emission. Moreover, there are no additional FIRST detections beyond the four present in the NIR-NVSS overlay. It is clear that the four FIRST detections are in fact two radio lobes. The position of the NVSS centroid is between two LAS sources; a faint one on the left and a bright one on the right. The manner in which the FIRST emission is distributed may suggest that the bi-polar jets are precessing in a clockwise direction. This is important, as it helps to create a dynamic picture of the radio source. From this, we may infer that the central point is between the two leading edges of the radio lobes, rather than between the brightest two

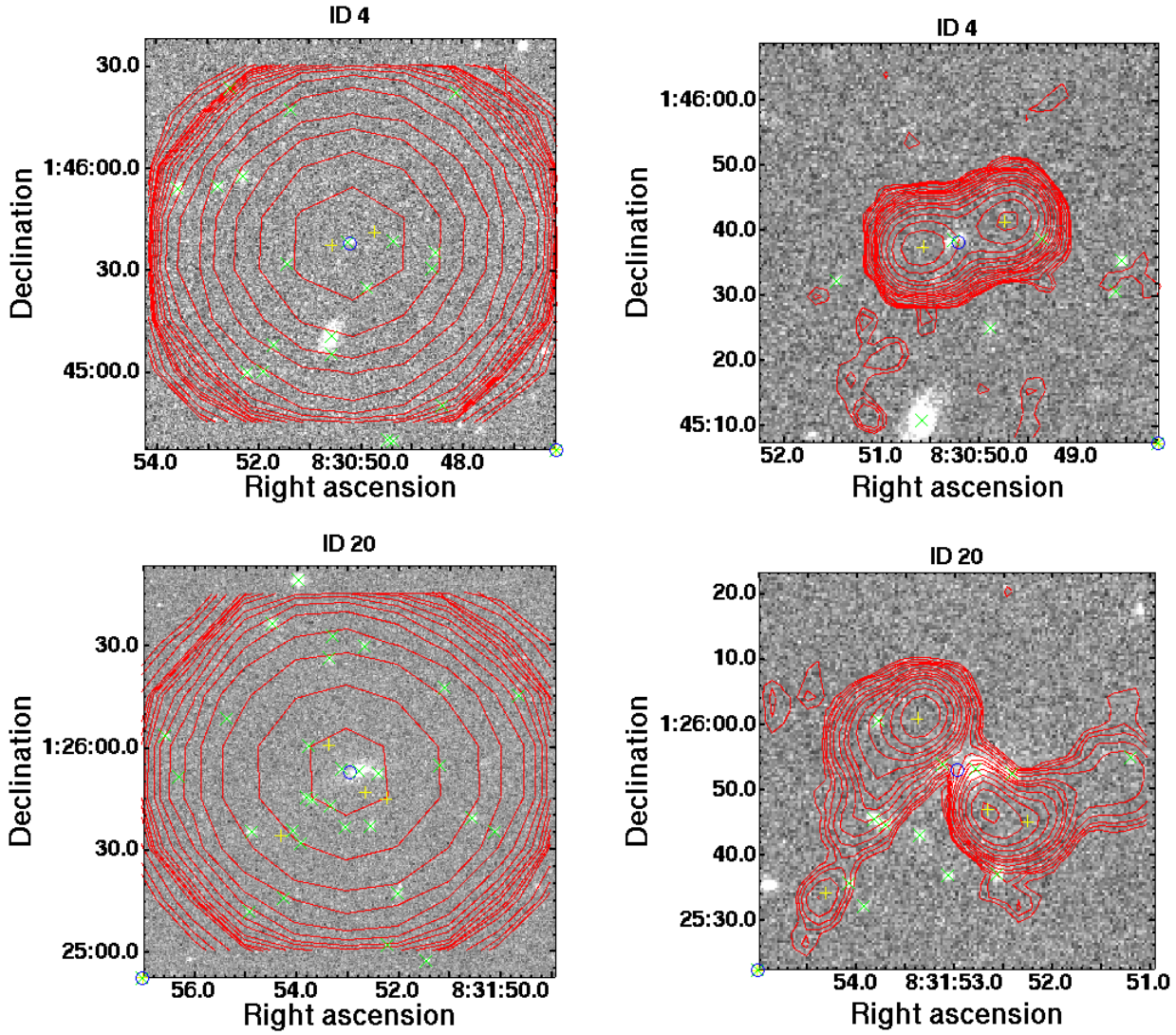

Figure 2.4: K-band NVSS overlays (left). K-band FIRST overlays (right). Contours and symbols as in Fig. 2.4. For all the overlays created, NVSS and FIRST data is represented by 23 contours between 0.3 & 2000 mJy / beam and 0.1 & 2000 mJy / beam, respectively.

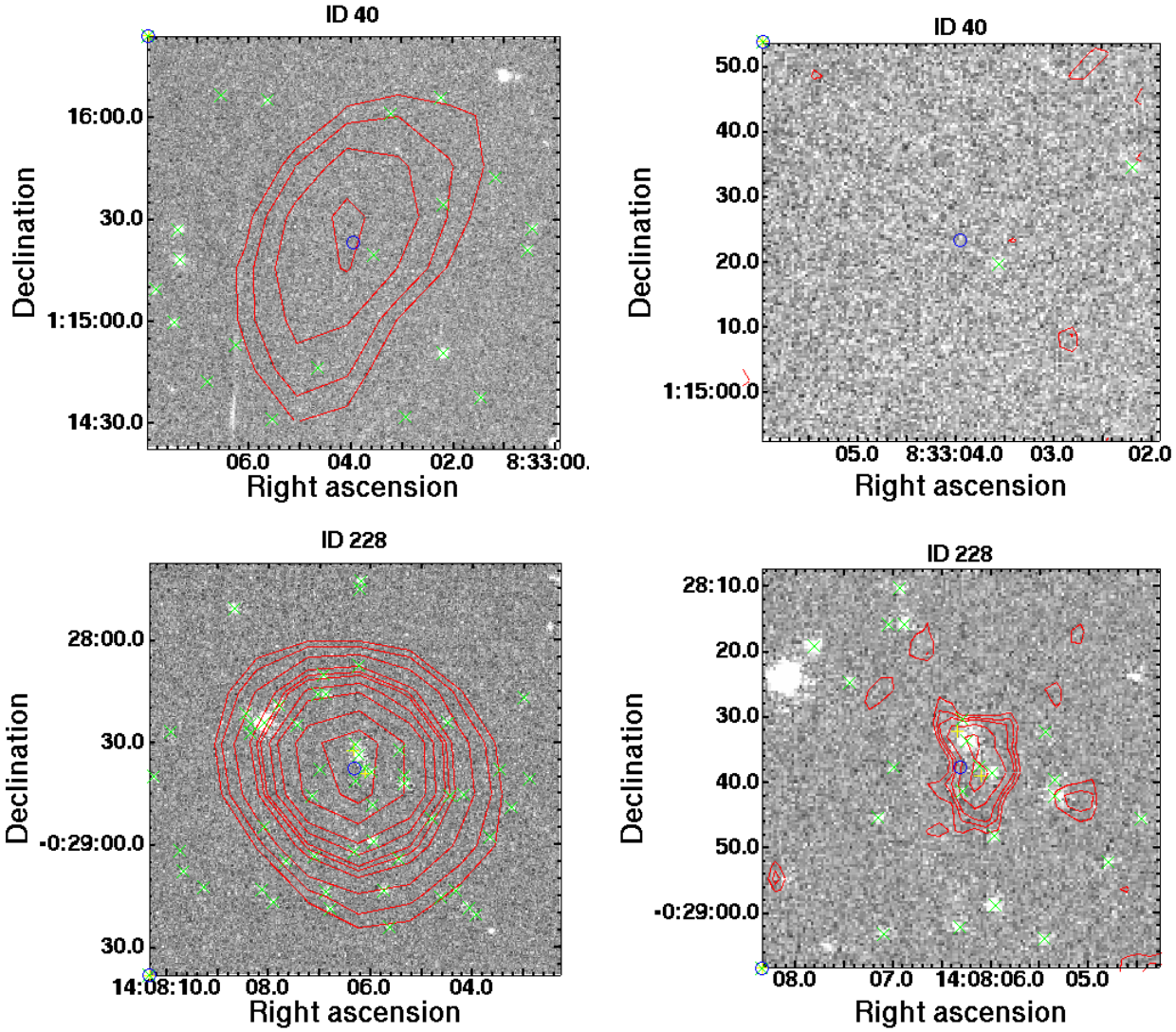

Figure 2.5: K-band NVSS overlays (left). K-band FIRST overlays (right). Contours and symbols as in Fig. 2.5. For all the overlays created, NVSS and FIRST data is represented by 23 contours between 0.3 & 2000 mJy / beam and 0.1 & 2000 mJy / beam, respectively.

FIRST detections. Thus, the host is likely the brighter LAS source. This is consistent with the fact that brighter NIR sources tend to be the hosts of the most luminous radio galaxies (e.g. Willott et al. 2003; McLure et al. 2004). For this radio source, the position and magnitude of the bright radio source was used. This source has a flux density of $S_{1.4\,\mathrm{GHz}} = 123.3\,\mathrm{mJy}$.

ID 40: The NIR-NVSS and the NIR-FIRST overlays are shown on the top left and right-hand sides of Fig. 2.5, respectively. There is no evidence for any emission beyond the extent of the overlay. There is no evidence for multiple / compact components in the NIR-FIRST image either. The flux density of the radio source is 3.5 mJy. There is a candidate host $6.9''$ from the NVSS position, but the lack of FIRST flux surrounding that source makes an association difficult. Throughout the matching process, I took a conservative approach, only matching sources which were beyond reasonable doubt, and so this radio source was not identified with any LAS counterpart.

ID 228: The NIR-NVSS and the NIR-FIRST overlays are shown on the bottom left and right-hand sides of Fig. 2.5, respectively. There is no evidence for any emission beyond the extent of the overlay. However, it is clear that the field is very crowded. Turning to the NIR-FIRST overlay, we can see that this crowding makes selecting a single, or even multiple hosts for the radio emission extremely difficult. Therefore, I conservatively decided not to select a host for this source. This does bias the matched catalogue against clusters; however, there are only 29 sources for which no host was selected for these reasons (i.e. $< 0.9\%$ of the matched sample). This source has a flux density of $S_{1.4\,\mathrm{GHz}} = 7.6\,\mathrm{mJy}$.

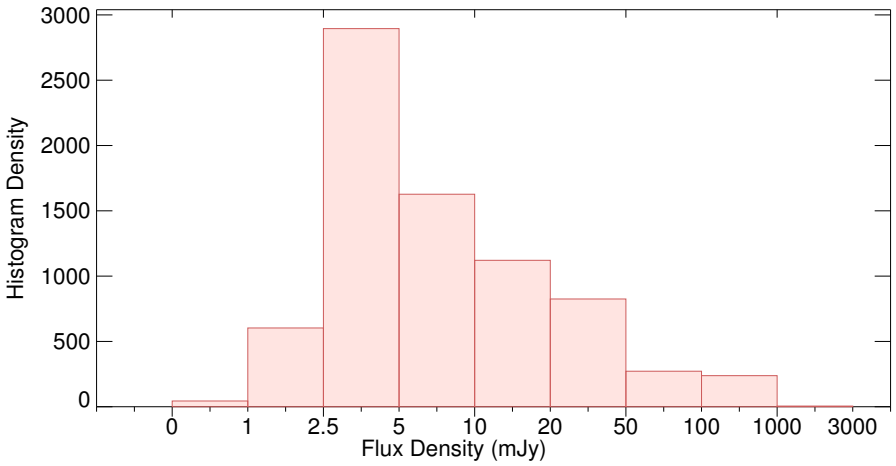

Figure 2.6: A histogram of the 1.4-GHz flux density of the radio sources in the radio catalogue.

2.5 General catalogue statistics

The initial NVSS catalogue for the phase 1 area contained 7630 sources. Since the LAS does not cover the entire phase 1 field, 592 of those sources were excluded from further analysis. A further 193 sources were 'added' after radio-source 'de-blending' was taken into account (note, the matching process allows multiple NVSS detections to merge into one as well as a single NVSS detection to be de-blended). This left a total of 7231 radio sources. A histogram of the NVSS flux density distribution is shown in Fig. 2.6.

The matching process described in Section 2.3 will obviously alter the flux density distribution of the survey from its initial state. It is interesting to ask if this change is significant and if so, at which flux densities? Only $\sim 4\%$ of the radio sources have had their flux densities altered. In Fig. 2.7, a histogram of the normalised 'corrected' flux density divided by the normalised 'uncorrected' flux density distribution is shown. I define 'uncorrected' as the initial, unprocessed flux density distribution of the radio catalogue and 'corrected' as the flux density distribution after the matching process. I find that the matching process results in an additional $\sim 20\%$ of radio sources between 1-2.5 mJy. This flux density range is be-

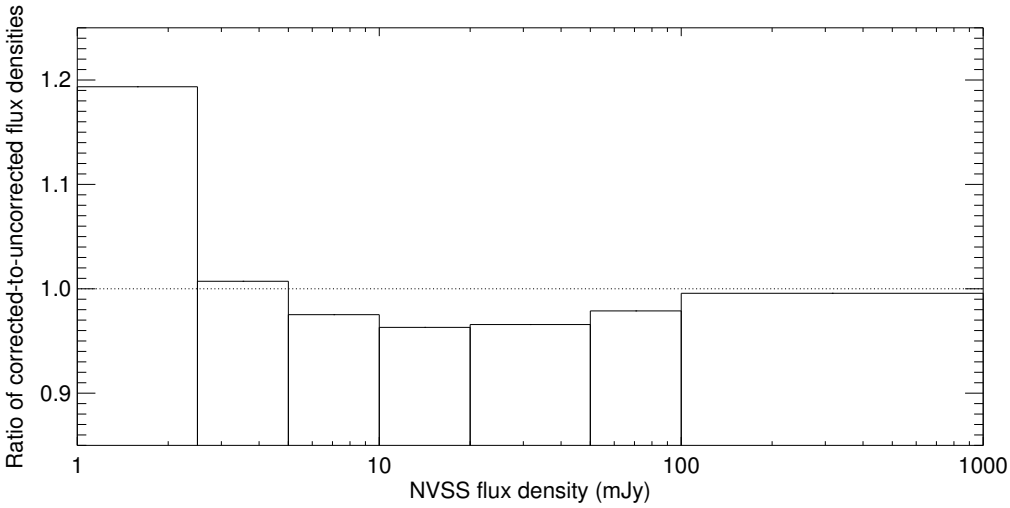

Figure 2.7: The ratio of the normalised 'corrected' and 'uncorrected' flux density distributions (as defined in the text) at 1.4-GHz.

low the 5σ sensitivity of the survey. However, it is clear that those additional sources must have been drawn from across the flux density distribution, and accounting for their existence is important if one wants the best possible list of identifications and the most accurate flux density estimates. Note that Fig. 2.7 only looks at the net changes between flux density bins and therefore does not reveal the amount of 'churn' between bins (e.g. how many sources > 100 mJy have been de-blended into two or more sources which are > 20 mJy).

Of the remaining sources, 3323 (or 46.0%) were successfully matched to a source in the K-band. A histogram of the K-band magnitude distribution is shown in Fig. 2.8, from which it is clear that the depth of the IR catalogue is ~ 18.0 magnitudes.

2.6 Spurious matches

It is clear that not all the NIR matches in a radio catalogue of this size will be correct. In this section, I try to estimate the number of spurious matches. The contribution to the probability of a spurious match may come in several forms. A widely used technique to estimate the number of spurious matches involves offsetting the radio catalogue and repeating the

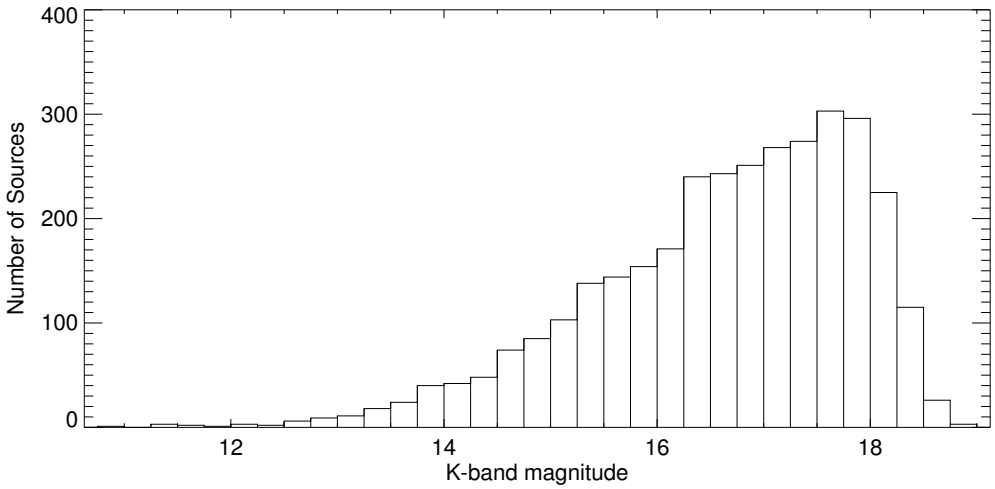

Figure 2.8: Histogram of the K-band magnitude distribution for matched radio sources.

matching process. This allows one to estimate the number of 'intrinsic' spurious matches. However, because this catalogue was created using visual classification techniques, such a process was considered impractical. Systematic errors can be described as originating from the structure of the cross-matching method. For example, if larger overlays of radio sources which showed evidence for extended emission were not created, then the probability of a spurious match would increase, as lobes may be matched to the wrong host galaxy. The matching approach described in Section 2.3 is designed to minimise this type of error, however, it is very difficult to quantify. Fortunately, another matched radio catalogue (created by John Ching, hereafter referred to as the John Ching Catalogue: JCC - see Hardcastle et al. 2013 for a brief description of the catalogue) was created for the purposes of investigating the FIR properties of radio galaxies as a function of their optical spectra. This catalogue may be used in order to estimate the agreement rate for counterpart identification. Here, I give a brief description of the JCC, although further details will be available in Ching et al. (*in preparation*). The JCC cross-matching method involves automatically grouping FIRST components that were likely subcomponents of a single optical source (e.g. the core and lobes of a radio galaxy) and automatically matching them to optical counterparts if they satisfied

certain criteria based on symmetries of the radio sources. Where they did not, visual classification was performed by overlaying SDSS images with FIRST and NVSS contours. All the FIRST components that were not identified as possible subcomponents were cross-matched to the nearest SDSS optical counterpart, with a maximum separation of 2.5″.

The JCC covers $\sim 80\%$ of the area covered by the radio catalogue presented here. However, it has a much lower surface density due to the requirement that the SDSS sources must have optical spectra. In order to calculate the agreement rate between both catalogues, the JCC was filtered in the following manner:

- The JCC is filtered so that a common area between both radio catalogues is created. This reduced the JCC from 2,066 to 1,607 sources.

- FIRST is a deeper survey than the NVSS for point sources, therefore there may be some sources in the JCC which have not been classified in the radio catalogue presented here. The filtered JCC is therefore cross-matched with the raw NVSS catalogue on a 30″ best-match basis in order to ensure a common set of sources between both catalogues. This reduced the JCC to 1,075 sources.

- Next, the JCC is cross-matched with the processed radio catalogue presented here on a 2.5″ best-match basis. 1,005 sources are recovered, which equated to $\sim$93.5% of the JCC. This implies a disagreement rate of 6.5%.

We note that the disagreement rate which has been calculated is only a *rough* estimate of the true disagreement rate. In addition, source detection differences between the LAS and SDSS may contribute a slight increase in the disagreement rate. In any case, the conclusion from this calculation is clear: the overwhelming majority of our sources would have been matched to the same hosts using the method adopted by the JCC. The fact that similar results would have been obtained using two separate identification methods gives confidence to the

quality of the radio catalogue.

A second source of error comes in the form of human subjectivity. What one human regards to be a match may not be the conclusion of another. In order to ensure that such variations were limited, another individual (Sarah V. White) classified 905 radio sources which amounts to 12.7% of the total, unprocessed radio catalogue. The disagreement rate between the radio catalogues was found to be $< 1\%$ (i.e. over 99% of the radio sources were matched, or not matched, identically). This shows that the matching method described in Section 2.3 does not produce much variability. Thus, on the basis of these two tests the expected failure rate of the matching process is likely to be $\lesssim 6\%$, small enough for the purposes of the work presented throughout the thesis.

Chapter 3

Herschel-ATLAS/GAMA: What determines the far-infrared properties of radio-galaxies?

The work presented in this chapter is based on two articles published in '*Monthly Notices of the Royal Astronomical Society*.' All work presented here was carried out by me.

(1) - Hardcastle M. J., Virdee J. S., et al., 2010, MNRAS, 409, 122: '*Herschel-ATLAS/GAMA: The FIR properties of radio galaxies*'

(2) - Virdee J. S., et al., 2013, MNRAS, 432, 609V: '*Herschel-ATLAS/GAMA: What determines the FIR properties of radio galaxies?*'

3.1 Introduction

The relationship between radio-AGN and the dust properties of their hosts has not been studied in great detail due to the lack of deep, large-area surveys at FIR / submm wavelengths.

However, a complex relationship is expected if radio-AGN feedback plays a significant role in galaxy evolution.

FIR / sub-mm studies of star-formation in samples of radio galaxies have generally concentrated on high-redshift objects, in which emission at long wavelengths (e.g. 850 μm, 1.2 mm) corresponds to rest-frame wavelengths around the expected peak of thermal dust emission. Working at these high redshifts with small targeted samples necessarily restricted these studies to the most powerful radio-AGN (e.g. Archibald et al. 2001; Reuland et al. 2004). What these studies found was that the submillimeter luminosity was a strong function of redshift, even after other correlations with galaxy properties such as radio power, radio spectral index and size, were taken into account. These results suggest that high-redshift ($1 < z < 5$) radio-galaxies contained increasingly youthful stellar populations. However, this is thought to be true of the galaxy population as a whole, so that, placing such results in context is difficult.

The availability of observations at FIR / sub-mm wavelengths with the *Herschel Space Observatory* (Pilbratt et al. 2010) opens up the possibility of studies of very large populations of more nearby objects. The *Herschel* Astrophysical Terahertz Large Area Survey (H-ATLAS: Eales et al. 2010a) has mapped 550 sq degrees in 5 photometric bands (100, 160, 250, 350 and 500μm) with 5σ sensitivities of 132, 121, 33.5, 37.7 and 44.0 mJy respectively (Rigby et al. 2011b). Using data from the Science Demonstration Phase (SDP; $\sim$ 14.4 deg^2 from the 9^{hr} equatorial field), Hardcastle et al. [2010] (a study that used the radio catalogue defined in Chapter 2; hereafter H10) studied the FIR properties of radio galaxies out to redshift 0.85. This work sought to establish, on a statistical basis, whether radio-detected galaxies have different FIR luminosities than their non-radio-detected counterparts. H10 found no evidence for any difference, although the low source count ($\sim$ 200) made it difficult to investigate the FIR luminosity dependence on parameters such as galaxy mass or optical colour.

In this chapter I investigate the FIR luminosity and dust temperature of radio galaxies as a function of radio luminosity, redshift, radio-source size and radio spectral index. There are a number of observational advantages when selecting AGN in the radio. Firstly, radio emission is unaffected by obscuring dust. Secondly, large scale surveys at radio frequencies, in combination with deep near-IR photometry, allow large numbers of sources to be identified across a wide redshift range. Thirdly, the size of the observed radio jets can provide a rough indication of the age of the radio source and consequently, the AGN (e.g. Kaiser, Dennett-Thorpe & Alexander 1997). An analysis of all the radio-selected objects identified with galaxies in the 134.7 deg^2 H-ATLAS Phase 1 field is presented. This represents an order of magnitude increase in survey area over H10. The higher number of radio sources allows one to investigate a wider range of host galaxy properties as a function of the FIR luminosity. The chapter is structured as follows. In Section 3.2 I list the various sources of data I have used in the following analysis, and describe the general sample selection. In Section 3.3 I describe the radio sample selection and the properties of these sources. In Section 3.4 I describe how the FIR luminosities and dust temperatures of our sources were calculated followed by a discussion of the results in Section 3.5. Finally, I discuss the implications of the results and conclude in Section 3.6 and 3.7, respectively.

3.2 The data

In this section an overview of the data used throughout this chapter is given.

1. Radio source catalogues and images from the NRAO VLA Sky Survey (NVSS; Condon et al. 1998) and Faint Images of the Radio Sky at Twenty-one centimetres (FIRST; Becker, White & Helfand 1995) survey. These cover the entire H-ATLAS Phase 1 area (hereafter, simply Phase 1 area).

2. Radio source catalogues and images from the Giant Metrewave Radio Telescope at 330 MHz (hereafter referred to as GMRT images and catalogues) covering $\sim 82\%$ of the Phase 1 area (Mauch et al. 2013).

3. Point spread function (PSF) convolved, background subtracted images of the Phase 1 fields at the wavelengths of 250, 350 and 500 μm, provided by the Spectral and Photometric Imaging REceiver (SPIRE; Griffin et al. 2010) instrument on *Herschel*. The construction of these maps is described in detail by Pascale et al. [2011].

4. Photodetector Array Camera and Spectrometer (PACS; Poglitsch et al. 2010) maps at the wavelengths of 100 and 160 μm. The reduction process for these maps is described in detail by Ibar et al. [2010].

5. Catalogues and images from the United Kingdom Infrared Telescope Deep Sky Survey - Large Area Survey (UKIDSS-LAS, hereafter LAS; Lawrence et al. 2007). The LAS covers $\sim 95.6\%$ of the Phase 1 area.

6. A set of photometric redshifts for galaxies detected by either the Sloan Digital Sky Survey Data Release 7 (hereafter, SDSS; Abazajian et al. 2009) or the LAS. These redshifts were generated using the artificial neural network code ANNz (Collister & Lahav 2004). More details on the generation of the photometric redshifts is described in Smith et al. [2011] (hereafter, S11). This catalogue provides a redshift estimate for every source detected in the optical and NIR bands.

7. A catalogue of identifications between optically detected galaxies and H-ATLAS galaxies (Valiante et al. *in preparation* and Hoyos et al. *in preparation*; both based on S11). They define the reliability, R, which is a measure of whether a single optical (r-band) source dominates the observed FIR emission. They suggest that only sources with $R > 0.8$ be considered matches.

8. Redshifts from the Galaxy And Mass Assembly (GAMA; Driver et al. 2011, 2009) survey. GAMA is a deep spectroscopic survey with limiting depths of $r_{\rm AB} < 19.8$ mag, $z < 18.2$ and $K_{\rm AB} < 17.6$ mag over the Phase 1 field; details of the target selection and priorities are given by Baldry et al. [2010]. The GAMA catalogue (SpecAllv14) for this area contains 131,921 new spectroscopic redshifts in addition to 10,351 redshifts from previous surveys in the area.

First, I filtered the galaxy catalogue so as to require a K-band detection in the LAS ($K < 18.0$) and an r'-band detection ($r' < 22.0$) in the SDSS. Next, this catalogue was cross-matched with the H-ATLAS catalogue using TOPCAT[1] (Taylor 2005) on a $1''$ best-match basis in order to identify which sources are detected at the 5σ limit. Note that sources which did not have matches remained in the resulting catalogue, albeit without any associated *Herschel* data from the H-ATLAS catalogue. In order to gain spectroscopic redshifts, the resulting galaxy catalogue was cross-matched with the GAMA catalogue on a $1''$ best-match basis, again retaining sources which were not matched. Spectroscopic redshifts were then selected from GAMA and SDSS in preference to photometric redshifts. If a photometric redshift was used, the error on the redshift was required to be $<20\%$ of the redshift. In addition, sources not in the redshift range $0.01 < z < 0.8$ were removed (the upper-limit is imposed via errors on the photometric data). Approximately 24% of the sample have spectroscopic redshifts. 98% of the spectroscopic redshifts are below $z<0.5$. In order to reliably calculate the stellar mass and the optical colour, I filtered the catalogue so as to exclude any sources that are point-like in either the LAS or the SDSS parent catalogues. K-corrected g′- r′ colours were then calculated using KCORRECT v4.2 (Blanton & Roweis 2007) for the whole sample. This process gave a total of 324,222 galaxies in the Phase 1 field, from which the galaxies hosting radio emission are separated in the next section. Thus, the galaxy catalogue will be split into two; the radio-detected catalogue and the non-radio-

[1]Tool for OPerations on Catalogues And Tables

detected catalogue (or simply the 'comparison' catalogue).

3.3 The radio-detected sample

To produce the radio galaxy sample, I selected all the catalogued NVSS sources in the Phase 1 field above 2.25 mJy (the 5σ limit for the NVSS catalogue). The good short-baseline coverage of NVSS ensures that the flux densities are good estimates of the true total flux-densities for sources smaller than the primary beam of NVSS (45″). Although the NVSS is only $\sim 25\%$ complete at 2.25 mJy (rising to $\sim 100\%$ at 3.5 mJy), the lower flux cut is retained since no bias is expected to be introduced from the incompleteness. None of the analysis is strongly dependent on the completeness of the sample. I estimate that $< 0.1\%$ (or ~ 230 sources) of the comparison sample should have been associated with radio-emission (this is because the NVSS source extraction software does not extract 100% of the radio sources below 3.5 mJy; see Condon et al. 1998). However, this is negligible given that there are over 320,000 sources in the comparison sample. Next, I manually inspected all of the NVSS sources in order to ensure that the correct host was identified for those radio sources which have complex structures (e.g. doubles). This process is described in detail in Chapter 2.

Next, I cross-matched the radio catalogue from Chapter 2 with the galaxy catalogue (see previous section) using the LAS positions on a $1''$ best-match basis. This process gave a total of 1599 radio-detected sources in the Phase 1 field, of which 1110 (or 69%), had spectroscopic redshifts. Approximately 80% of the spectroscopic redshifts are below $z = 0.5$. The SDSS r'-band limit accounts for the reduction of LAS identified radio sources from 3182 to 1599; $\sim$76% of the dropouts have $K > 17.0$.

Next, I measured projected radio source sizes for all the cross-matched radio sources. If the source was compact in FIRST, the de-convolved major axis from the FIRST catalogue

was used as the projected size of the radio source. The 1σ error on the source size is given by,

$$1\sigma(\text{size}) = 10.0'' \times \left(\frac{1}{\text{SNR}} + \frac{1}{75}\right), \tag{3.1}$$

where SNR is the signal-to-noise ratio of the FIRST source (Becker, White & Helfand 1995). If the de-convolved source size was less than $2\sigma(\text{size})$ (equivalent to the 95% contour) the $2\sigma(\text{size})$ upper limit was taken; this was the case for $\sim 1\%$ of the sources. The sizes of more complicated structures such as double-lobed radio sources were measured by calculating the projected distance between the peaks of the lobes. Where there was evidence for multiple lobes, the distance between the two furthest lobes from the host was recorded. There were 89 objects in which the NVSS emission was 'resolved out' in FIRST. Such sources were not assigned sizes and were thus excluded from the analysis involving radio source sizes.

In order to calculate spectral indices[1], I crossed-matched the filtered 1.4-GHz radio catalogue with 330 MHz GMRT radio catalogues and images, whose depth ranges from 3-10 mJy (Mauch et al. 2013). Each match was checked manually by overlaying GMRT radio contours on LAS K-band images. A total of 726 sources were successfully matched. Upper limits on the spectral indices were calculated for the remaining sources (654) by substituting the GMRT flux by five times the local RMS. A further 219 radio sources do not have spectral indices or limits due to limited coverage of the GMRT data in the Phase 1 field. This catalogue, which is a subset of the main radio catalogue described above, is only used in the analysis involving spectral indices (i.e. Section 3.5.3).

The above processes gave a radio catalogue which is flux-limited in the radio and also magnitude-limited in the optical and NIR. The result is that there are few sources (71) with $z > 0.7$. The catalogue is also likely to be strongly biased against radio-detected quasars since point-like sources have been excluded from the galaxy catalogue. This has the desirable effect that the measured FIR luminosities will tend not to be strongly affected by beaming

[1]Where the spectral index α is defined in the sense that $S \propto \nu^{-\alpha}$

of the radio jet and that any contamination of the fluxes measured at *Herschel* wavelengths by non-thermal emission might be expected to be limited (cf. the results of Hes, Barthel & Hoekstra 1995). Hereafter, the sources not identified with radio emission are referred to as comparison sources while sources identified with radio emission are referred to as radio-detected sources.

3.3.1 K-band luminosity cuts

In order to account for any stellar mass dependent relations, I calculated the K-band luminosity. The K-band luminosity is dominated by old stellar light (e.g. Best, Longair & Röttgering 1998; Simpson, Rawlings & Lacy 1999) and thus scales well with stellar mass. In order to enable one to compare radio galaxies with their mass-equivalent-counterparts, the K-band luminosity is used.

Fig. 3.1 shows the absolute K-band magnitude versus redshift. To calculate the K-correction and the passive-evolution correction in the K-band, a GALAXEV starburst spectral energy distribution is used (see Bruzual & Charlot 2003) with the following properties: a $z = 4$ instantaneous starburst with solar metallicity and an exponentially decaying star-formation lifetime of $\tau = 1$ Gyr. These corrections are applied to both the radio sources and the comparison galaxies. A value of -23.96 for M^*_K is adopted (Smith, Loveday & Cross 2009), from which L^*_K is calculated to be $7.87 \times 10^{10}\ L_\odot$. Next, the radio-selected sample is separated into two magnitude bins, defined by $\mathrm{M}_K >$ -24.4 (sub-1.5 L^*_K) and $\mathrm{M}_K < -24.4$ (super-1.5 L^*_K). This boundary was chosen so that both sub-samples contained roughly the same number of sources. For illustrative purposes only, I calculate the stellar mass boundary assuming a mass-to-light ratio of 0.6 (Kauffmann & Charlot 1998), and find it to be $\sim 7.1 \times 10^{10}\ \mathrm{M}_\odot$. The lower-luminosity sample contains 770 radio sources while the higher-luminosity sample contains 829 radio sources.

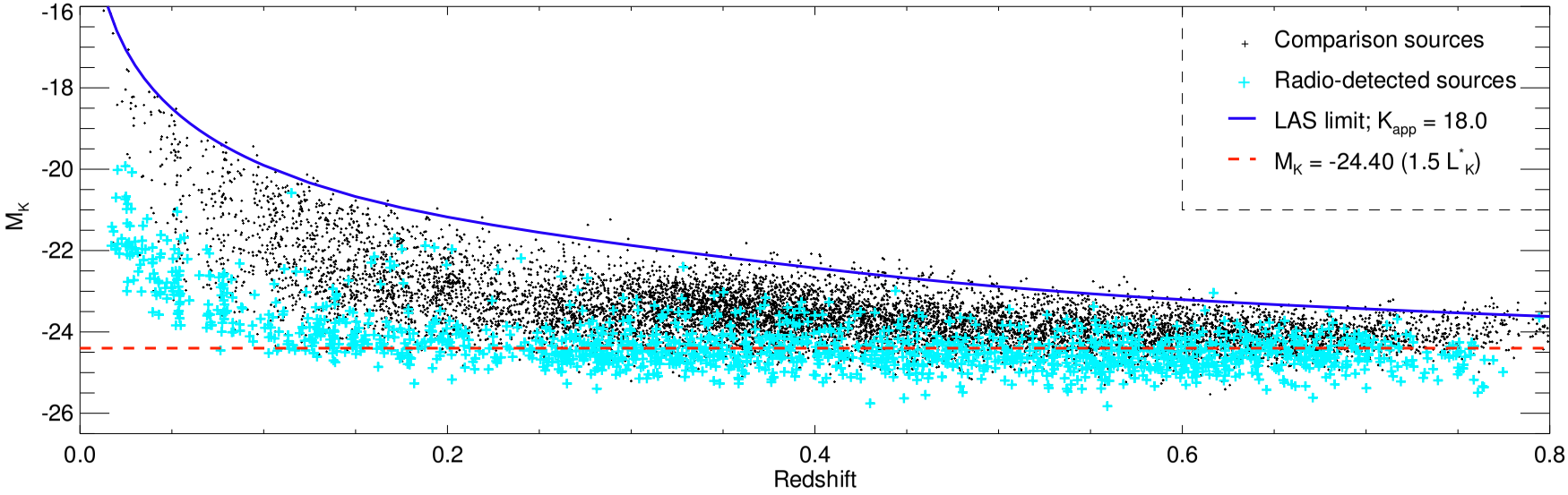

Figure 3.1: Absolute K-band magnitude (M_K) versus redshift for galaxies in the radio-detected and comparison samples. K-corrected, passive-evolution corrected radio-galaxies are shown as blue crosses. The comparison sources are shown as black dots. For clarity, only 0.3% of the comparison sources (randomly selected) are plotted. The dashed red line, at -24.40, separates the sub- and super-1.5 L^*_K samples. The solid dark-blue line is the depth of the LAS in the K-band ($K = 18.0$).

3.3.2 Radio luminosities

Fig. 3.2 shows the 1.4-GHz radio luminosity ($L_{1.4\,\mathrm{GHz}}$) versus redshift for the two K-band luminosity separated radio samples. Since less than half of the radio sources at 1.4-GHz are detected at 330 MHz, I adopt $\alpha = 0.8$ when calculating the 1.4-GHz radio luminosity of *all* the radio sources; $\alpha = 0.8$ is a typical observed value for low-frequency selected objects, and I expect that the selection against point-like objects in the optical will tend to select against flat-spectrum radio sources. Indeed, the subset of sources with GMRT detections suggest that only $\sim 2\%$ of the radio sources have $\alpha < 0$ and that $\alpha = 0.8$ is a reasonable value for the sample. Note however that because the depth of the GMRT is lower than that of the NVSS, there is a bias against constraining flat spectrum sources.

It is clear from Fig. 3.2 that a wide range of radio luminosities is probed. At the low-luminosity, low redshift end (i.e. $z < 0.2$), I expect from existing analysis of the local 1.4-GHz luminosity function (e.g. Sadler et al. 2002; Mauch & Sadler 2007) that the population will be dominated by star-forming galaxies rather than radio AGN, although a few AGN may still be present. The starburst luminosity function cuts off steeply above $5 \times 10^{23}\,\mathrm{W\,Hz^{-1}}$ at 1.4-GHz, so I expect that most of the objects above this luminosity will be radio AGN. Thus, in the sub-1.5 L_K^* radio sample there exist two populations; the low redshift, low luminosity starburst population and the higher redshift, higher luminosity radio AGN population. The super-1.5 L_K^* radio sample contains fewer sources below $5 \times 10^{23}\,\mathrm{W\,Hz^{-1}}$ and are thus almost exclusively composed of radio AGN. As mentioned in Section 1.4.3.3, Best & Heckman [2012] calculated the HERG / LERG luminosity functions for the local Universe and found that HERGs begin to dominate above $10^{26}\,\mathrm{W\,Hz^{-1}}$. Thus, both samples will be dominated by LERGs, although significant numbers of HERGs may still be present.

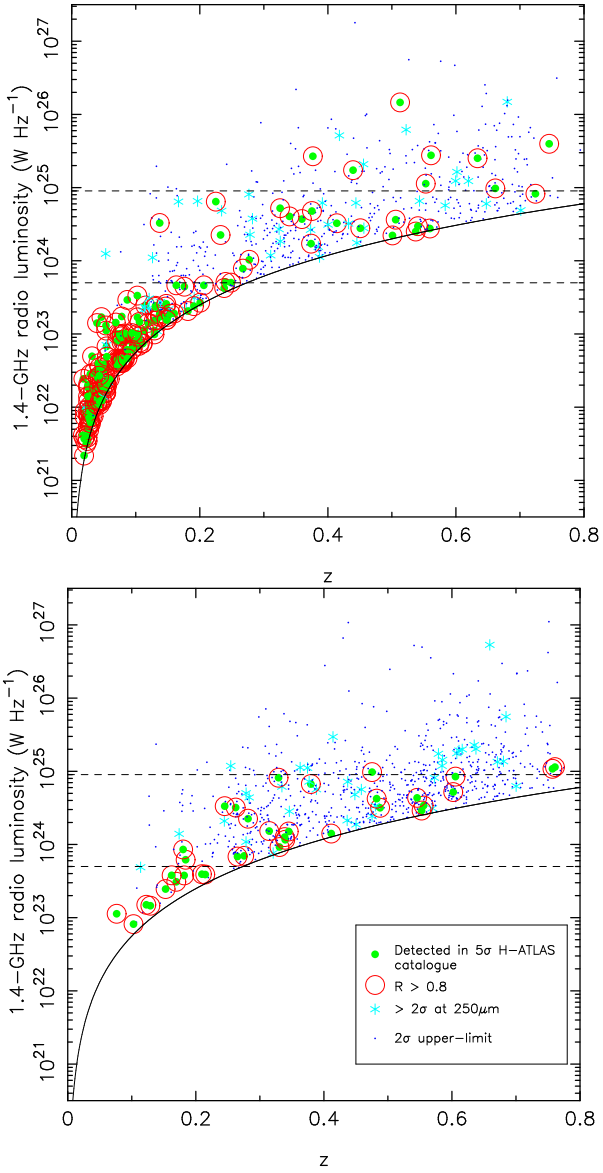

Figure 3.2: Radio luminosities of the radio-detected sample as a function of redshift split into the sub-1.5 L^*_K sample (top) and super-1.5 L^*_K (bottom) sample. Sources nominally detected by *Herschel* (i.e. sources identified with H-ATLAS objects) are marked as filled green circles. If the association with the LAS galaxy is deemed 'reliable', the object is also marked with a red open circle. Any source not identified with an H-ATLAS object in the catalogue, but which is detected down to the 2σ level (see Section 3.4.1 for how I define the 2σ level) in the 250-μm images, is shown as a light-blue star for illustrative purposes only. Non-detections are marked with blue dots. The solid line corresponds to the nominal 5σ flux cutoff in the NVSS (i.e. 2.25 mJy). Dashed horizontal lines show radio luminosities corresponding to; (from bottom to top) the point at which the starburst radio luminosity function cuts off steeply (Sadler et al. 2002) and the expected luminosity for a maximal (4000 $M_\odot$ yr^{-1}; Kennicutt 1998b) starburst.

3.4 The far-IR properties of the sample

3.4.1 *Herschel* flux density measurements

In this section I describe the properties of the sample in the FIR. Throughout this section, FIR flux densities in the SPIRE bands are measured directly from the background-subtracted, PSF-convolved H-ATLAS Phase 1 images described in Section 3.2, taking the best estimate of the flux density to be the value in the image at the pixel corresponding most closely to the LAS position of our targets, with errors estimated from the corresponding position in the noise map. As discussed in Pascale et al. [2010], PSF-convolved maps provide the maximum-likelihood estimate for the flux density of a single isolated point source at a given position in the presence of thermal noise. I also extracted PACS flux densities and corresponding errors from the images at 100 and 160 μm using circular apertures appropriate for the PACS beam ($15.0''$ and $22.5''$, respectively) and using the appropriate aperture corrections, which take account of whether any map-pixels have been masked during the process of high-pass filtering of the bolometer timelines. I add an estimated absolute flux calibration uncertainty of 10% (PACS) and 7% (SPIRE) in quadrature to the errors measured from the maps for the purposes of fitting and stacking, as recommended in H-ATLAS documentation. To account for bright, extended objects, I use the flux densities in the Phase 1 5σ catalogue where available, in preference to the measured flux densities, even though the measured flux densities correlate well with the catalogued fluxes. To correct for confusion in the SPIRE maps, I subtract the mean flux density level of the whole PSF-convolved map from the flux density measurements of each source. This ensures that the mean of a randomly selected sample will be zero within the uncertainties.

Approximately 13.6% of the radio sample (218 sources, which includes potential star-forming galaxies) is detected at the 5σ limit demanded by the H-ATLAS source catalogue. This is broadly similar to the detection fraction found in H10. Since the images at 250, 350

and 500 μm are seriously affected by confusion (as opposed to the PACS maps, which are not), I cannot use the 2σ limit defined by simple Gaussian statistics (i.e. twice the rms). Instead, I follow Hardcastle et al. [2013] (hereafter, H13) and randomly sample a large number of points in the 250, 350 and 500 μm maps, selecting the flux density value below which 97.7% of the random fluxes lie as the 2σ limit. This gives 2σ flux limits of 24.6, 26.5 and 25.6 mJy for the 250, 350 and 500-mm SPIRE maps respectively. Therefore, sources which have a $S/N > 2$ at 250, 350 and 500 μm make up 18.9, 16.6 and 12.6% of the sample, respectively.

I note that whether a source is 'detected' or not plays no part in the following analysis, since I am interested in the sample properties taken as a whole. However, in some of the following plots, the FIR luminosity of sources above 2σ are shown as individual points for illustrative purposes only.

3.4.2 250μm luminosity calculations; single temperature method

In H10, the integrated IR-luminosity of individual sources was calculated by assuming a spectral energy distribution (SED) with $T = 26$ K and $\beta = 1.5$ following Dye et al. [2010]. In this Chapter, I follow a similar method to that of H10 with some key differences. Firstly, I assume $T = 20$ K and $\beta = 1.8$, best-fitting values derived for a similarly selected sample of radio galaxies by H13. Secondly, I calculate the FIR luminosity at 250 μm, rather than the integrated IR luminosity. This means that the isothermal model, and hence the assumed temperature, only acts as a K-correction factor in the determination of the 250 μm luminosity (L_{250}) of each source. Further, I note that at low redshifts, the calculated K-correction should have almost no effect on the 250 μm luminosity. The disadvantage of switching to the 250 μm luminosity is that one is no longer able to estimate the SFR. However, the relations which convert the integrated IR luminosity to a SFR are calibrated for star-forming galaxies (e.g. Kennicutt 1998b; Kennicutt et al. 2009) and thus may not be applicable to the

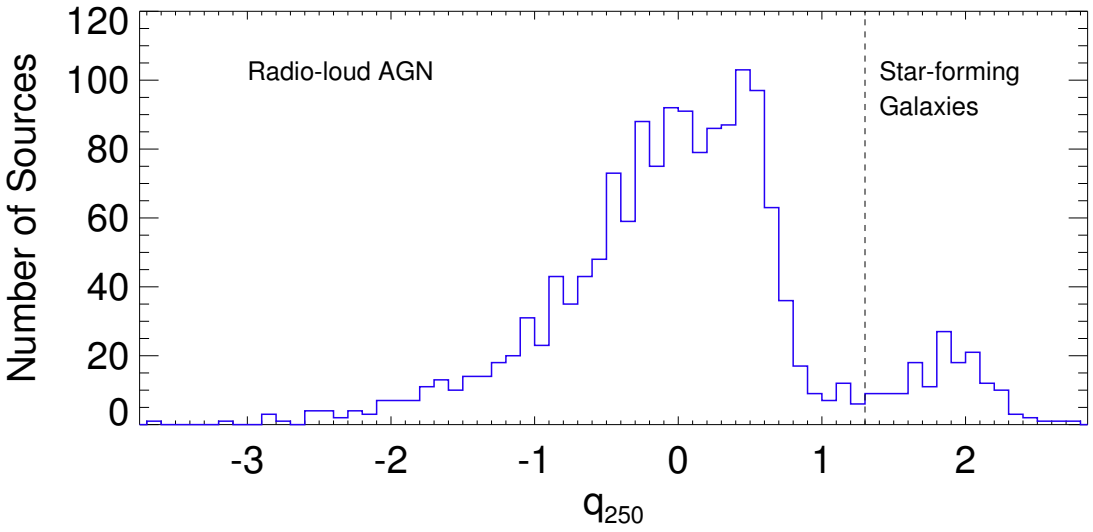

Figure 3.3: Histogram of q_{250} values, defined in Eq. 2. I remove all sources with $q_{250} > 1.3$ in order to ensure no star-forming objects are in the radio-loud AGN sample. I note that many of the values $q_{250} < 1.3$ are upper limits.

temperature and luminosity range occupied by radio galaxies.

The SPIRE PSF has a FWHM of $18''$ at 250 μm. This translates to linear sizes of $\sim$135 kpc at $z = 0.8$, the redshift of the most distant objects in the sample. Therefore, the corresponding FIR luminosities and temperatures one measures apply not only to the host of the radio source, but also to its immediate environment; this may include quiescent dust or star-formation in a companion or merging galaxy.

3.4.3 Removing star-forming galaxies

In order to present an analysis of radio AGN, radio-detected star-forming sources need removing. To do this, I calculate q_{250} as follows,

$$q_{250} = \log_{10}(L_{250}/L_{1.4\,\mathrm{GHz}}). \tag{3.2}$$

If a source has a q_{250} value between $1.4 < q_{250} < 2.1$, it is on the far-infrared radio correlation (FIRC) which holds for star-forming galaxies (Jarvis et al. 2010). q_{250} was calculated for all the radio sources in the sample. A histogram of the results is shown in Fig. 3.3. Using Fig. 3.3, I choose to remove all sources with $q_{250} > 1.3$ or where the upper limit on q_{250} is > 1.3, ensuring that no (or a negligible few) star-forming objects are in the subsequent radio AGN sample. Therefore, beyond this point star-forming objects play no further part in the catalogues / analysis unless explicitly stated.

3.4.4 Stacking analysis

Since the vast majority of the radio AGN ($\sim 95\%$) are undetected at the 5σ limit of the Phase 1 catalogue, I need to use statistical methods to calculate the properties of the source population. I elect to stack the sample using the 100, 160, 250, 350 and 500 μm H-ATLAS maps in bins of redshift and radio luminosity, which range from $0.01 < z < 0.8$ and $21.0 < \log_{10}(L_{1.4\,\mathrm{GHz}}) < 27.3$. I use constant bin sizes in radio luminosity and redshift, for both K-band luminosity separated samples in order to facilitate comparisons.

To establish quantitatively whether sources in the bins were significantly detected, I measured flux densities from 100,000 randomly chosen positions in the field; a Kolmogorov-Smirnov (K-S) test could then be used to see whether the sources from the sample were consistent with being drawn from a population defined by the random positions. Using a K-S test rather than simply considering the calculated uncertainties on the measured fluxes allows one to account for the non-Gaussian nature of the noise as a result of confusion. If the fluxes in any given bin are significantly distinguished from the background on a K-S test, and have a mean flux density higher than that of the underlying noise (which should be zero, see Section 3.4.1), one can calculate the *stacked luminosity* using all the objects in that bin, in the knowledge that the resulting value is not simply noise.

The results from this analysis are shown in Tables 3.1 and 3.2. Both tables show the

Radio Sample	z range	Objects in bin	Mean bin flux density (mJy)					K-S probability (%)				
			SPIRE bands			PACS bands		SPIRE bands			PACS bands	
			250 μm	350 μm	500 μm	100 μm	160 μm	250 μm	350 μm	500 μm	100 μm	160 μm
$<1.5\,L_K^*$	0.00 – 0.15	92	25.0 ± 0.8	9.8 ± 0.8	6.9 ± 0.9	36.7 ± 3.2	34.8 ± 3.9	$< 10^{-3}$	$< 10^{-3}$	0.02	0.04	0.3
	0.15 – 0.25	90	9.0 ± 0.7	3.1 ± 0.8	2.9 ± 0.9	12.8 ± 3.0	21.0 ± 3.8	$< 10^{-3}$	0.09	2.2	16.5	0.6
	0.25 – 0.40	182	7.0 ± 0.5	1.3 ± 0.5	2.4 ± 0.6	12.1 ± 2.2	6.4 ± 2.8	$< 10^{-3}$	1.4	5.8	1.5	82.7
	0.40 – 0.50	78	7.5 ± 0.7	2.8 ± 0.8	5.0 ± 1.0	1.6 ± 3.4	21.6 ± 4.2	$< 10^{-3}$	0.02	0.006	92.4	0.03
	0.50 – 0.60	75	9.1 ± 0.7	3.9 ± 0.8	4.9 ± 1.0	9.5 ± 3.6	19.8 ± 4.4	$< 10^{-3}$	0.2	0.5	42.1	12.2
	0.60 – 0.80	113	5.7 ± 0.6	2.2 ± 0.7	4.5 ± 0.8	1.7 ± 3.0	12.9 ± 3.8	$< 10^{-3}$	0.002	0.001	44.0	8.0
$>1.5\,L_K^*$	0.00 – 0.15	11	6.7 ± 1.9	4.6 ± 2.2	3.8 ± 2.5	3.2 ± 9.0	12.7 ± 11.0	4.3	9.0	22.4	70.7	88.9
	0.15 – 0.25	40	9.8 ± 1.0	3.2 ± 1.1	3.0 ± 1.3	25.4 ± 5.0	34.4 ± 6.3	1.2	2.4	29.6	8.8	0.9
	0.25 – 0.40	236	6.4 ± 0.4	2.3 ± 0.5	3.1 ± 0.5	6.6 ± 2.0	10.8 ± 2.5	$< 10^{-3}$	$< 10^{-3}$	0.2	37.0	6.1
	0.40 – 0.50	140	2.7 ± 0.5	-0.3 ± 0.6	1.1 ± 0.7	-1.5 ± 2.5	0.9 ± 3.1	0.04	15.5	40.4	83.2	42.0
	0.50 – 0.60	178	2.2 ± 0.5	-0.0 ± 0.5	1.3 ± 0.6	-4.6 ± 2.3	4.3 ± 2.9	0.2	1.1	4.7	41.8	85.2
	0.60 – 0.80	210	4.1 ± 0.4	1.3 ± 0.5	3.3 ± 0.6	3.1 ± 2.1	5.2 ± 2.7	$< 10^{-3}$	0.003	0.1	4.4	12.2

Table 3.1: Mean bin flux densities and K-S probabilities that the *Herschel* fluxes of radio-detected objects in redshift bins are drawn from the background distribution, as a function of wavelength. Low probabilities (below 1%) imply significant differences between the bin being considered and the distribution of flux densities measured from randomly selected positions in the sky, as described in the text. Sources on the FIRC are not included.

Radio Sample	Range in $\log_{10}(L_{1.4\,\mathrm{GHz}})$	Objects in bin	Mean bin flux density (mJy)					K-S probability (%)				
			SPIRE bands			PACS bands		SPIRE bands			PACS bands	
			250 μm	350 μm	500 μm	100 μm	160 μm	250 μm	350 μm	500 μm	100 μm	160 μm
$<1.5\,L_K^*$	21.0 – 23.7	114	22.3 ± 0.7	8.1 ± 0.7	5.1 ± 0.8	34.0 ± 2.8	30.1 ± 3.4	$< 10^{-3}$	$< 10^{-3}$	0.07	0.005	0.10
	23.7 – 24.3	140	4.3 ± 0.5	-0.7 ± 0.6	1.1 ± 0.7	7.8 ± 2.5	9.0 ± 3.2	$< 10^{-3}$	17.4	41.9	1.5	51.3
	24.3 – 24.6	115	9.2 ± 0.6	2.2 ± 0.7	3.3 ± 0.8	9.2 ± 2.8	21.5 ± 3.4	$< 10^{-3}$	0.8	0.6	56.4	3.0
	24.6 – 25.0	116	8.8 ± 0.6	5.1 ± 0.7	6.4 ± 0.8	8.0 ± 2.9	13.6 ± 3.7	$< 10^{-3}$	$< 10^{-3}$	0.002	38.4	20.5
	25.0 – 25.6	99	7.3 ± 0.6	2.9 ± 0.7	3.9 ± 0.8	3.7 ± 3.1	15.5 ± 3.8	$< 10^{-3}$	0.2	0.007	36.9	4.7
	25.6 – 27.3	46	7.7 ± 1.0	4.9 ± 1.1	7.7 ± 1.3	9.2 ± 4.4	13.4 ± 5.4	0.003	0.02	0.05	5.2	18.2
$>1.5\,L_K^*$	21.0 – 23.7	13	12.6 ± 1.8	6.4 ± 2.0	3.9 ± 2.3	7.3 ± 8.4	19.4 ± 10.2	1.2	8.0	7.5	59.3	25.9
	23.7 – 24.3	128	5.2 ± 0.6	1.2 ± 0.6	1.6 ± 0.7	6.8 ± 2.8	12.4 ± 3.4	0.002	0.3	13.2	8.4	5.9
	24.3 – 24.6	159	5.1 ± 0.5	3.0 ± 0.6	4.9 ± 0.7	1.6 ± 2.4	9.2 ± 3.0	0.009	$< 10^{-3}$	0.03	67.8	16.1
	24.6 – 25.0	268	3.2 ± 0.4	-0.3 ± 0.4	0.6 ± 0.5	3.0 ± 1.9	6.0 ± 2.4	0.006	0.9	34.0	56.0	51.2
	25.0 – 25.6	183	4.5 ± 0.5	1.5 ± 0.5	3.7 ± 0.6	-1.3 ± 2.2	5.3 ± 2.8	$< 10^{-3}$	0.06	0.2	56.6	1.3
	25.6 – 27.3	64	3.9 ± 0.8	0.8 ± 0.9	1.6 ± 1.0	7.1 ± 3.5	2.5 ± 4.6	0.008	0.2	36.3	0.9	57.0

Table 3.2: Mean bin flux densities and K-S probabilities that the *Herschel* fluxes of radio-detected objects in radio luminosity bins are drawn from the background distribution, as a function of wavelength. Low probabilities (below 1%) imply significant differences between the bin being considered and the distribution of flux densities measured from randomly selected positions in the sky, as described in the text. Sources on the FIRC are not included.

results for the K-band luminosity separated radio samples. Sources on the FIRC have been removed. As is evident from Tables 3.1 and 3.2, most of the SPIRE bins are detected at the 95% confidence level (i.e. there is a $< 5\%$ chance that the flux density distribution has been drawn from the same underlying distribution as the background). However, the PACS bins are mostly indistinguishable from the background. This is a result of the lower sensitivity of the PACS data. It is also clear that the K-S probabilities are almost always lower at 250 μm than at any other band, with all of the bins at 250 μm detected above the 99% confidence level or better, except for the lowest redshift bin of the super-1.5 L_K^* sample. The higher sensitivity and smaller beam size at 250 μm are likely explanations for this. Indeed, if one excludes those radio sources which are also in the 5σ H-ATLAS catalogue from the K-S test, all the SPIRE bins are detected at the 96% confidence level or better except the super-L_K^* $0.15 < z < 0.25$ bin, which is detected at the 83.8% confidence level. This provides further justification for choosing the 250 μm band for the luminosity calculations. The K-S probabilities produced by the comparison sample are not shown, but all the bins at 250 μm were detected above the 99% confidence level or better.

In order to calculate stacked luminosities, I calculate the weighted average of L_{250} for each radio luminosity or redshift bin. Individual sources are weighted using the reciprocal of the square of the error extracted from the 250 μm noise map. In order to calculate errors on the stacked luminosity, I use the bootstrap method with replacement. This involves randomly selecting a subsample from the relevant bin, while ensuring that the total number of sources in that bin remains constant. This implies that the same source may be selected more than once and others omitted completely. From this new sample, a new weighted L_{250} value is calculated and stored. I repeat the process 300 times in order to get a distribution of weighted L_{250} values. From this distribution, I select the 16^{th} and 84^{th} percentiles as the lower and upper limits, respectively. The advantage of bootstrapping is that no assumption is made on the shape of the luminosity distribution; instead, I use the distribution of the

sample to calculate 1σ errors. This automatically takes all sources of intrinsic dispersion, such as redshift and flux density errors, into account. The errors plotted in all subsequent FIR luminosity plots are the 1σ uncertainties derived from bootstrapping.

3.4.5 Best-fitting temperatures method

In Section 3.4.2, I calculated the luminosity at 250 μm using an isothermal method with $T = 20$ K. Obviously, such a method contains no information on the dust temperature. In order to gain some constraints on the dust temperature, I assume a modified black-body model with,

$$f_v \propto \frac{\nu^{3+\beta}}{e^{\frac{h\nu}{kT}} - 1}, \tag{3.3}$$

where T represents the isothermal temperature of the source in question, ν is the frequency, k is the Boltzmann constant, h is the Planck constant and β is the beta parameter. The best-fitting isothermal dust temperature may then be calculated for all the sources any given bin using the following method. I cycle through temperatures between 5-55 K and fit to all the five *Herschel* bands, allowing only the normalization of each source to vary (assuming $\beta = 1.8$). For each temperature step, I sum the χ^2 value produced by each source. This results in a χ^2 distribution as a function of temperature from which I pick the temperature with the lowest χ^2 value. The errors are calculated by finding the range where $\Delta\chi^2 = 1$. A much used alternative method involves fitting to the stacked fluxes from each bin. Although much simpler, such an approach was not used here because of the wide redshift range of the sources in the bins.

Although the primary aim is to extract temperature information for each bin, I can use this temperature to calculate a K-corrected luminosity at 250 μm for every source in the bin, again allowing the normalization of each source to vary. It is important to stress here that the normalization of each source is determined from all five *Herschel* bands, so the resulting

S_{250} value (and therefore the L_{250}) may differ substantially from the nominal S_{250} value in the 250 μm map. Confusion bias is likely to affect the 500 μm band more strongly than any other due to the increased size of the beam and the higher noise levels. To ensure that the temperatures were not strongly biased by the inclusion of this band, I computed all the temperature estimates presented in the chapter with and without the 500 μm band, and found that the derived temperatures were not significantly different. In the next section I compare the L_{250} output of the $T = 20$ K isothermal method to that of the best-fitting temperature method described above.

3.4.6 FIR luminosities: comparison of methods

In this section I compare the luminosities of the single temperature and best-fitting temperature methods. To do this, I calculate the stacked luminosity at 250 μm of the radio-detected samples as a function of redshift and radio luminosity, the results of which are shown in Fig. 3.4 (note that all the bins are significantly detected with respect to the background). The plots on the upper panels include the sources on the FIRC whilst the plots on the lower panels exclude such sources. The luminosities are calculated using the single temperature method are shown by the stacks in blue while the luminosities calculated via the best-fitting temperature method are shown by the stacks in magenta. All the plotted sources in Fig. 3.4 have had their luminosities calculated assuming the single temperature method, and are shown for illustrative purposes only. In the top-left panel of Fig. 3.4, it is clear that the sources on the FIRC are well separated from the radio AGN population. This is not surprising given the clean separation observed in Fig. 3.3, nevertheless, it is encouraging to observe this bi-modality as a function of radio luminosity.

Turning first to the upper plots in Fig. 3.4, which contain star-forming sources, one can see that the luminosities from both methods do not agree particularly well. The results of the best-fitting temperature method produces fitted temperatures ranging from 17-30 K,

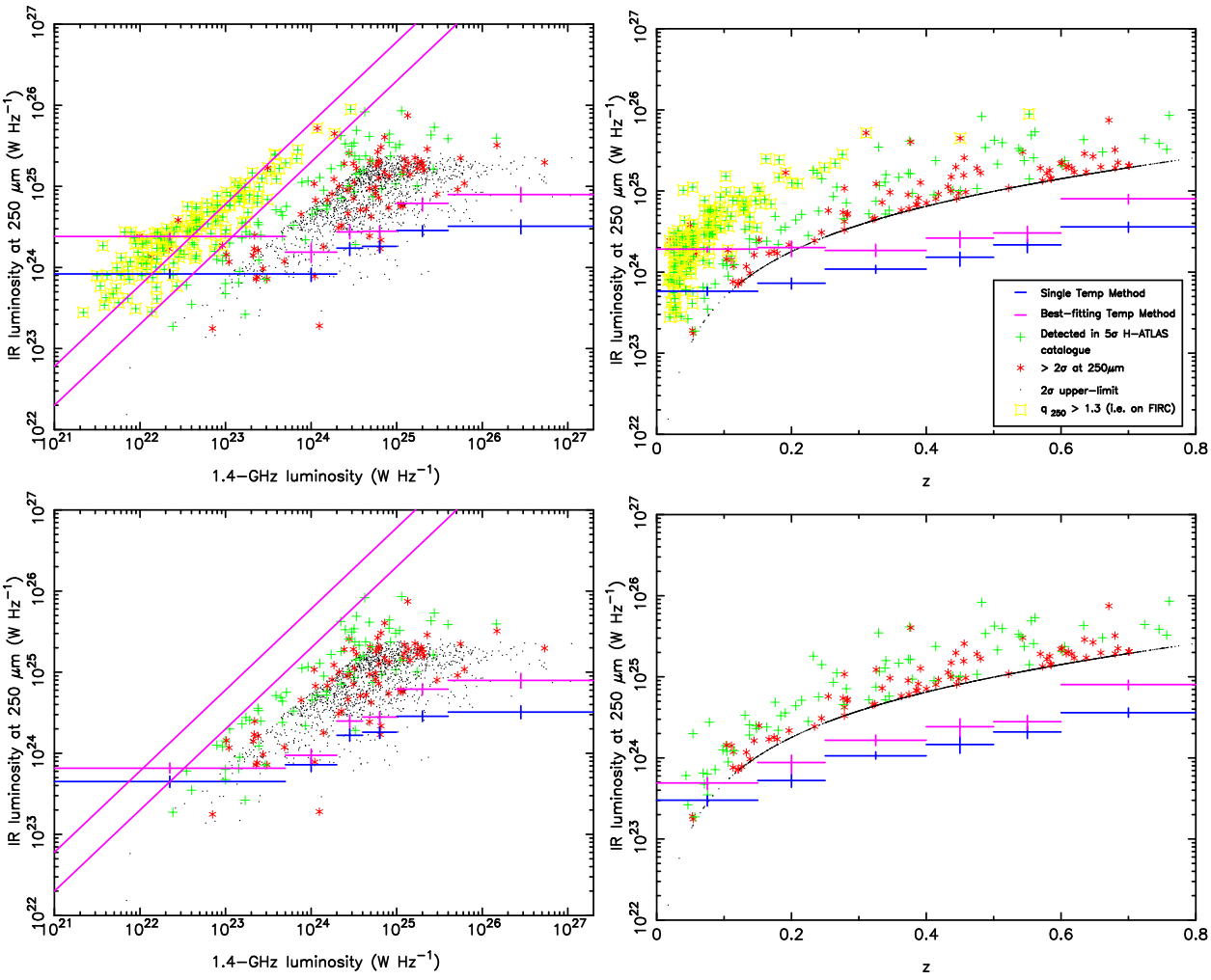

Figure 3.4: Stacked infrared luminosity at 250 μm as a function of (left panels) 1.4-GHz radio luminosity and (right panels) redshift. Radio sources on the FIRC are included (top panels); radio sources on the FIRC are not included (bottom panels). Plotted sources, which are shown for illustrative purposes only, have had their luminosities calculated using the single temperature method described in the text. FIR luminosities calculated via the single temperature method (best-fitting temperature method) are in blue (magenta). Green crosses represent the 5σ detected sources defined by the Phase 1 catalogue whilst the red stars and the black points represent the sources with $>2\sigma$ and 2σ upper-limits, respectively. Those sources with $q_{250} > 1.3$ are identified with yellow boxes. The upper and lower magenta lines are $q_{250} = 1.78$ (the FIRC) and $q_{250} = 1.3$, respectively.

with all but the highest redshift and radio luminosity stacks having fitted temperatures above $T = 20\,\mathrm{K}$. Furthermore, the luminosities derived from the best-fitting temperature method appear systematically higher than the ones observed for the single temperature method. This is because individual sources in the best-fitting temperature method are free to find their own normalisations based on the information in *all* the *Herschel* bands. This normalisation value is usually higher when star-forming objects are included, probably due to the flux contained in the PACS bands. If one removes the hot, bright low-redshift star-forming objects (Fig. 3.4: lower plots), the luminosity difference between both methods decreases significantly. Nevertheless, there are still some luminosity differences between both methods.

When investigating the FIR luminosities of the radio-detected and comparison samples, I will not use the best-fitting temperature method. This is because under this method, the 250 μm luminosity of any given source is dependent on the luminosities of the others in that bin through the temperature estimation. The single temperature method described above is not susceptible to such correlations, as a single temperature and an independent flux density value is used when calculating individual luminosities. The systematic luminosity differences observed between methods suggest that the errors on the absolute luminosities of both methods have probably been underestimated. However, the science conclusions will depend on the *relative* luminosities between samples (i.e. between the radio-detected and comparison samples). Therefore, in so far as $T = 20\,\mathrm{K}$ is a reasonable temperature estimate for the K-correction of our sample, the single temperature method described in Section 3.4.2 is sufficient for the investigation of luminosity differences between samples. All the following plots have had their IR luminosities calculated using the single temperature method, while the temperatures have been calculated using the best-fitting temperature method.

3.4.7 What does the luminosity at 250μm trace?

Using the rest-frame luminosity at 250 μm minimises the dispersion in the FIR luminosity calculations, but what does it physically trace? First, one must tackle the issue of AGN contamination from (1) synchrotron emission and (2) hot dusty-tori. The first of these points has largely been addressed in the text above; point sources which may be face-on quasars were filtered from the catalogue at an early stage. As for dusty tori surrounding AGN, they peak in the mid-IR. When the required mid-IR data are available, which is not the case for the sample at present, decompositions of the SEDs of radio-detected and non-radio-detected AGN tend to show that observer-frame *Herschel* SPIRE bands are dominated by cool dust rather than by the torus component, even for powerful AGN with luminous tori (e.g. Barthel et al. 2012; Del Moro et al. 2013). Since the luminosity calculations rely solely on the 250 μm band, little AGN contamination is expected. In our best-fitting temperature method, I use PACS 100 μm data which at $z = 0.8$ (the maximum redshift in the sample) corresponds to a rest-frame wavelength of 55.5 μm. Although there is some potential for AGN contamination here I note that broadly, torus luminosity scales with the radio luminosity (Hardcastle, Evans & Croston 2009), and the vast majority of our sources are below the threshold for 'powerful radio galaxies' ($> 1\times10^{26}$ WHz^{-1}) where bright tori might be expected. In addition, the noise in the PACS bands mean that PACS photometry is lightly weighted relative to the SPIRE bands in the temperature fitting method. Therefore, I do not believe that our luminosities or temperatures have been significantly affected by AGN components.

In reality, dust exists at a range of temperatures whose integrated luminosity is often fitted by one, or two, modified isothermal-blackbody spectrums (e.g. Dunne et al. 2011). This has been driven by an inability to determine, and thus constrain, the physical composition and / or temperature distribution of the dust, which would allow more sophisticated models to be used. Nevertheless, for the purposes of understanding what the luminosity at

250 μm represents in the sample, it is instructive to assume a two-temperature blackbody model. Such models attempt to separate warm dust, which is expected to dominate the IR luminosity output, from the cold dust, which is expected to dominate the dust mass (Dunne et al. 2011). In general, priors for the cold and warm components range from 10-25 K and 30-60 K respectively (e.g. da Cunha, Charlot & Elbaz 2008). At 250 μm, both components may contribute to the total luminosity. For example, assuming a warm dust component with a temperature of 32 K and a cold dust component with a temperature of 15 K, with the latter contributing 90% of the total dust mass (typical for sources detected in the H-ATLAS; Dunne et al. 2011), I find that both components would contribute equally to L_{250}. Although other temperature combinations are possible within the range of temperature priors quoted above, this demonstrates the inability to state unambiguously that L_{250} is dominated by either warm or cold dust. This degeneracy is important, as it is likely that the warm dust is being heated by on-going star-formation. Given the depth of the data, I make no attempt to partition L_{250} into a warm and cold component, although, in Section 3.5.2, I use the temperatures generated from the best-fitting temperature method to shed light on this degeneracy.

3.5 Results

3.5.1 FIR properties of radio-galaxies

Galaxy mass is a fundamental indicator of host galaxy properties. This is especially true of radio galaxies. For this reason, I investigate the luminosity at 250 μm of the radio AGN sample as a function of the K-band luminosity, as well as redshift, radio luminosity and radio source size.

In the lower left-hand panel of Fig. 3.4, it is clear that L_{250} increases with the 1.4-GHz radio luminosity. However, such a relation may be the result of observational selection effects. For example, the incompleteness that arises from the flux-limited nature of the NVSS means

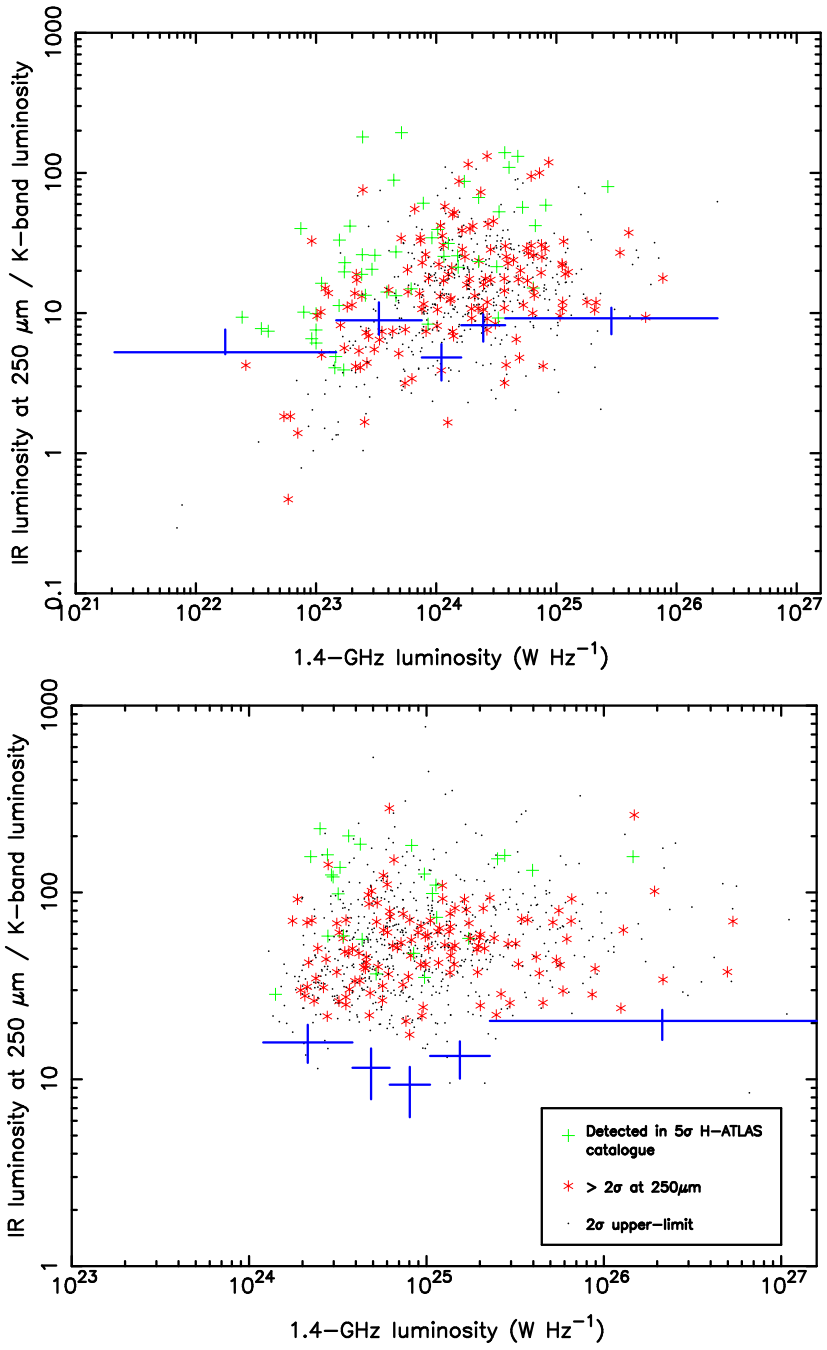

Figure 3.5: Stacked FIR luminosity at 250 μm (W Hz^{-1}) divided by the K-band luminosity (W Hz^{-1}), as a function of 1.4-GHz radio luminosity for sources $z < 0.4$ (top) and $z > 0.4$ (bottom). Note the different axial ranges present in both plots. Sources on the FIRC are not included.

that I cannot identify faint radio sources at high redshift. The inclusion of such sources would likely flatten the observed relation since I expect these sources to have systematically higher L_{250} values than their lower redshift counterparts (the FIR luminosity of the galaxy population as a whole increases with redshift for the redshift range under discussion; Dunne et al. 2011). A similar selection effect is at work with respect to the K-band magnitude-limited LAS data. Such a limit means that I do not detect low-luminosity (i.e. low-mass) radio sources at high redshift (see Fig. 3.1). In order to remove any stellar-mass bias, I divide L_{250} by L_K in Fig. 3.5. This new value can be thought of as the specific FIR luminosity at 250 μm. To limit the redshift bias, I plot the sources below and above $z = 0.4$ in the upper and lower-hand panels of Fig. 3.5, respectively. The sizes of the stacked bins are chosen so as to ensure that an equal number of radio sources were in each stack. The best fitting (assuming a line with a gradient of zero) specific FIR luminosities at 250 μm of the $z < 0.4$ and $z > 0.4$ samples are 6.5$\pm$1.7 and 13.4$\pm$3.9, respectively. Nevertheless, it is clear that any relation between L_{250} and 1.4-GHz radio luminosity disappears after the stellar-mass corrections, although the FIR luminosities of the $z > 0.4$ sources are systematically higher than that of the $z < 0.4$ sources. These results imply that the strength of a galaxy's radio emission has little or no bearing on its specific FIR luminosity at 250 μm.

Next, I compare the IR luminosities of the radio-detected sample to that of the comparison sample. The intension is to discover whether radio-AGN activity affects the FIR properties of the host. Therefore, it is important to ensure that the host properties of both samples are as similar as possible. In this section, I filter the comparison sample to ensure it has a similar optical colour distribution to that of the radio-detected sample. The average K-corrected g$'$ - r$'$ colours of the sub-1.5 L_K^* and super-1.5 L_K^* radio-detected samples are 0.83 and 0.90 respectively, while average colours of the sub and super-1.5 L_K^* comparison samples are 0.75 and 0.91, respectively. Thus, while the average colours of the super-1.5 L_K^* samples match up well, the sub-1.5 L_K^* radio-detected sample has redder colours than its comparison

sample. In order to take colour difference into account, I filter the sub and super-1.5 L_K^* comparison samples in the following manner. For each subsample I impose a global g′ - r′ colour cut, defined by the middle 98% of the radio galaxy colour distribution; this removes any outliers in the radio-detected and comparison samples. Next, I randomly discard 1% of the galaxies in the comparison sample and then run a K-S test to establish how well the new colour distribution matches the one from the radio-detected sample. Discarding a *different* 1% and repeating the process N times, where N is the number of comparison sources in the sample, allows one to select the best-matching *reduced* catalogue. After selecting the best matching catalogue, I again discard 1% of the remaining sources in the comparison sample and repeat the entire process. This is done until the probability returned by the K-S test exceeds 10% (i.e. sufficient for the null hypothesis to be met). This colour-matching process is performed separately for the sources in each redshift bin. The main disadvantage of such a method is the potential loss of large fractions of the original comparison sample. The sub-1.5 L_K^* comparison sample loses $\sim$55% of its sources; however, this still leaves it with over 136,000 sources. The super-1.5 L_K^* comparison sample loses only $\sim$6% of its sources, leaving it with over 26,000 sources. In Fig. 3.6, I plot L_{250} versus redshift for both the radio and comparison samples. The radio galaxy stacks are plotted in dark blue whilst the comparison galaxy stacks are plotted in cyan. The stacks shown in orange are generated using the colour-matched comparison samples. Hereafter, 'colour-matched' samples refer to the comparison samples which have undergone the matching process described above.

It is immediately apparent from Fig. 3.6 that both the stacked radio and comparison samples show an increase in L_{250} with redshift. This is consistent with the picture that dust masses and star-formation activity were higher in the past (e.g. Dunne et al. 2011). Turning to the differences between the K-band luminosity separated radio-galaxies, there is a suggestion that the sources in the sub-1.5 L_K^* sample have higher FIR luminosities than

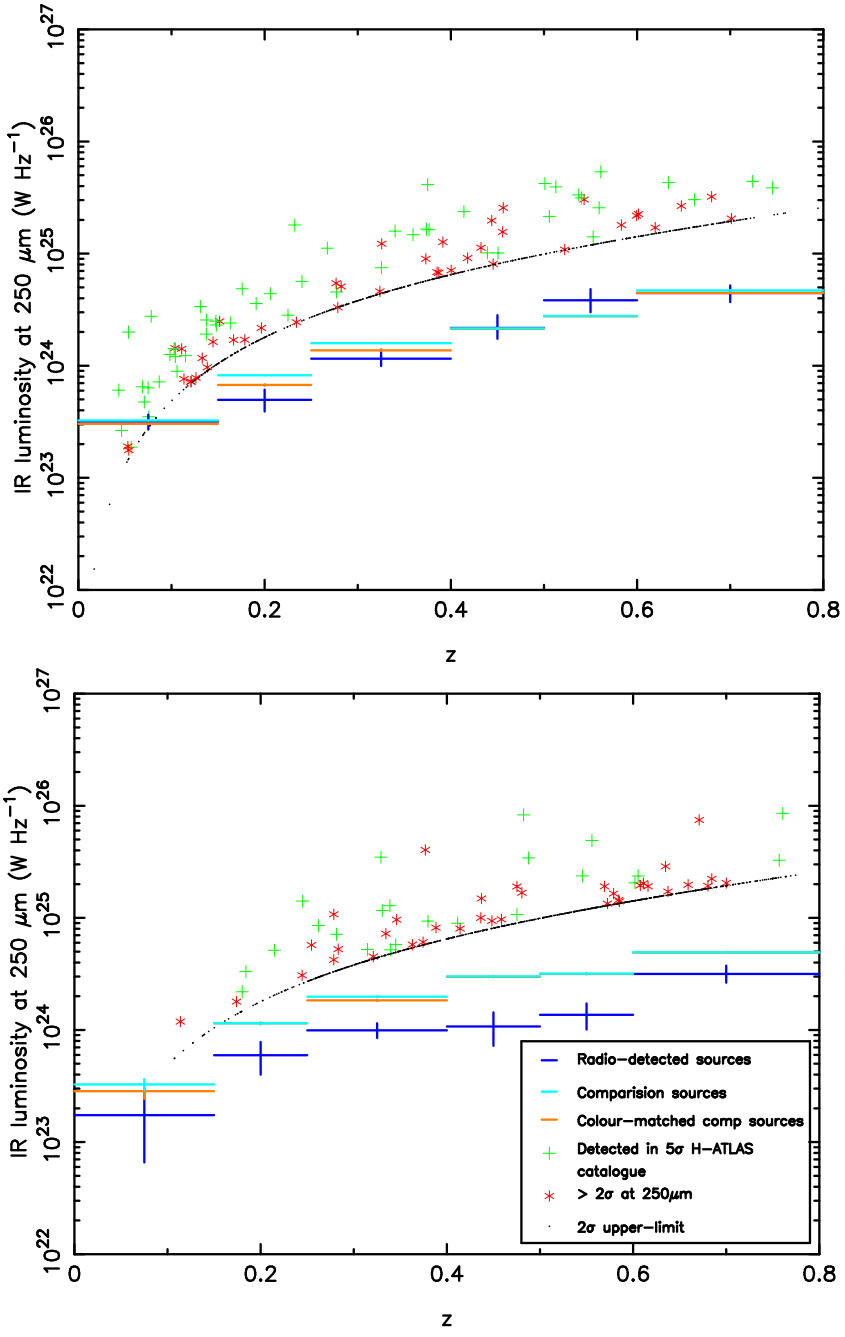

Figure 3.6: Stacked FIR luminosity at 250 μm as a function of redshift. Stacks shown in blue, cyan and orange represent the radio-detected, comparison and colour-matched comparison samples, respectively. Top and bottom plots contain the sub-1.5 L_K^* and super-1.5 L_K^* samples, respectively. In some redshift bins, the colour-matched comparison sample stacks are not clearly visible because the stacked luminosities are very similar to the unmatched comparison sample luminosities. Sources on the FIRC are not included.

those in the super-1.5 L_K^* sample. In order to quantify this difference, I divide the L_{250} values of the sub-1.5 L_K^* radio sample by the equivalent L_{250} values of the super-1.5 L_K^* radio sample. I find the sub-1.5 L_K^* radio sample to be 1.53$\pm$0.32 times as luminous at 250 μm as the super-1.5 L_K^* radio sample. Therefore, although there is some evidence for higher FIR luminosities in the sub-1.5 L_K^* sample, this result is not significant due to the large errors.

In order to judge, quantitatively, whether there is any difference between the radio-detected and comparison samples, I divide the L_{250} values of the radio-selected stacks by the 250 μm luminosity of the colour-matched comparison stacks, and show the results in Fig. 3.7. The sizes of the stacked bins were chosen so as to ensure an equal number of radio sources were in each stack. However, it is important to note several significant caveats before interpreting the results. Firstly, because the NVSS is a flux-limited survey, there are no high-redshift, low-luminosity radio sources in the sample: i.e, as I move to higher redshifts, one is preferentially selecting more powerful radio-AGN and placing any faint radio galaxies in the comparison sample. Secondly, since the base galaxy catalogue is magnitude limited in the K and r' bands, the catalogue becomes progressively incomplete with increasing redshift, losing faint and / or low-mass sources. Nonetheless, it is important to note that the radio and comparison samples have been selected from the same parent catalogue.

Fitting a line with a gradient of zero, I find that the best-fitting line for the sub-1.5 L_K^* radio-detected sample is 0.89 ± 0.18 times the FIR luminosity at 250 μm of the colour-matched comparison sample. Thus, being radio-loud is not associated with higher luminosities at 250 μm. This is markedly different from what one sees with the super-1.5 L_K^* radio sample, which is significantly better constrained due to better statistics. I find that the best-fitting line for this sample to be 0.49 ± 0.12 times the FIR luminosity at 250 μm of the colour-matched comparison sample. Thus, it is clear that super-1.5 L_K^* radio-galaxies show a strong 250 μm luminosity deficit with respect to their colour-matched comparison sample.

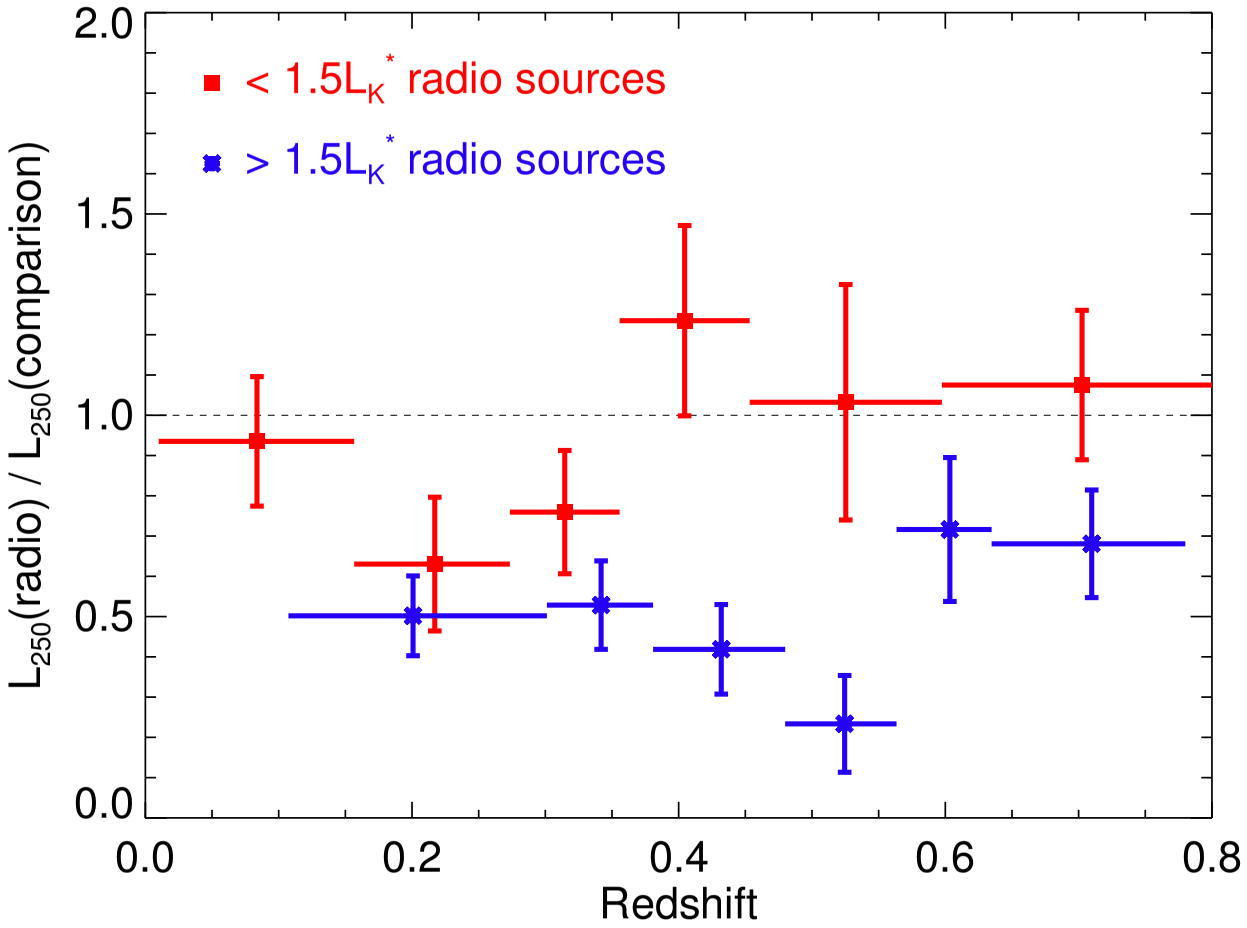

Figure 3.7: The ratio of the stacked L_{250} values of radio-detected and colour-matched comparison sample against redshift. The radio stacks are divided into sub (red) and super (blue) 1.5 L_K^* samples. Stack sizes are chosen to ensure each bin contains the same number of radio sources.

I discuss the significance of the above results in Section 3.6.

3.5.2 FIR emission as a function of radio source size

In Fig. 3.8 I plot L_{250} versus the projected radio source size. The size of the radio source can be thought of as a *rough* proxy for the age of the radio source (e.g. Kaiser, Dennett-Thorpe & Alexander 1997). The sizes of the stacked bins were chosen so as to keep all the radio sources with poorly constrained projected sizes in the first bin (i.e. < 30 kpc). All the signal in the bins are significantly detected on a K-S test with respect to the background. On the upper-hand panel of Fig. 3.8, I plot the results using the entire radio-detected sample with radio sizes. There is a clear indication that the luminosity at 250 μm falls with increasing source size. The null hypothesis, that L_{250} is independent of radio size, is rejected at the 95% confidence level. However, one must first discount the possibility that this fall in FIR luminosity is due to observational selection effects. Such an effect could be orchestrated if 'compact' radio sources (hereafter, compact refers to sources with projected sizes below 30 kpc) were at higher redshifts than their more 'extended' counterparts (hereafter, extended refers to sources with projected sizes above 30 kpc), during which FIR luminosities of all sources were higher, or at higher radio luminosities where the FIR luminosities of this sample are higher (see left-hand side of Fig. 3.4). I find that the sub-30 kpc radio sources are slightly biased towards the low-redshift and low radio-luminosity ends compared to the super-30 kpc sample.

To help elucidate the origin of the FIR excess at small radio source sizes, I calculate the best-fitting temperature, obtained using the best-fitting temperature method described in Section 3.4.5, for compact and extended radio sources. I find the fitted temperatures of compact and extended radio galaxies are 27.1 ± 0.3 K and 13.1 ± 0.3 K, respectively. The higher dust temperatures in compact radio sources are probably due to enhanced interstellar radiation fields heating the dust. The source of this heating is likely to be enhanced levels of,

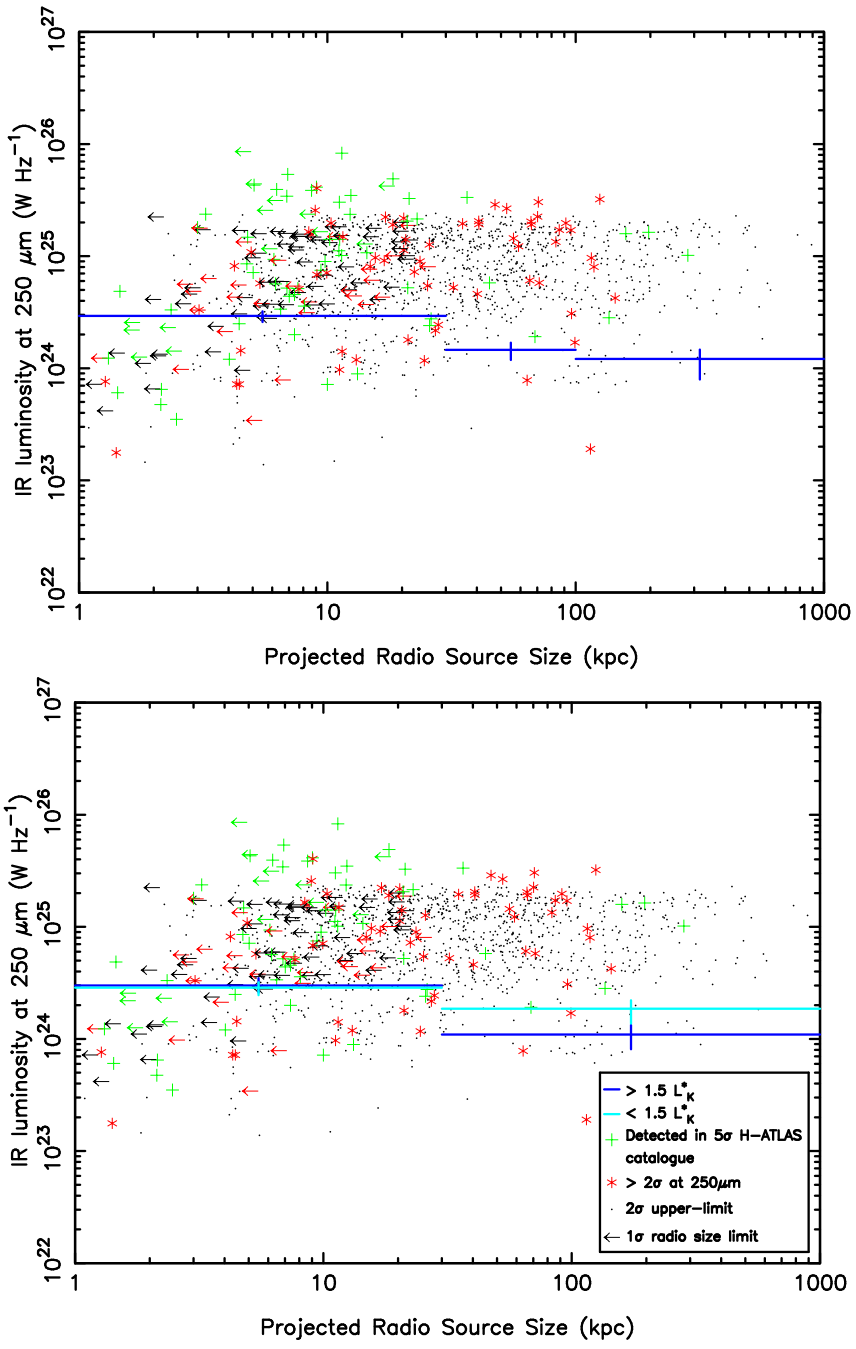

Figure 3.8: FIR luminosity at 250 μm versus the projected radio source size. On the top panel, I plot the stacked values for the entire radio-detected sample. On the bottom panel, I plot the stacked values for the sub (cyan) and super (blue) 1.5 L^*_K radio-detected samples. Plotted sources are shown for illustrative purposes only. Green crosses represent the 5σ detected sources defined by the H-ATLAS Phase 1 catalogue whilst red stars / black points represent the $> 2\sigma$ / 2σ upper limits respectively. The arrows represent the upper limits on the sizes of the radio sources. Radio sources on the FIRC have been excluded.

possibly jet-induced or merger associated, star-formation.

On the lower-hand panel of Fig. 3.8, I separate the sample using the K-band luminosity. The super-1.5 L_K^* and sub-1.5 L_K^* radio galaxy samples are shown in blue and cyan, respectively. Due to the sparsity of extended radio sources in the sub-1.5 L_K^* sample, I only plot two stacks divided at 30 kpc. It is clear that both samples show a fall in L_{250} with increasing radio source size, although the super-1.5 L_K^* sample dominates this trend. I discuss the implications of these results in Section 3.6.

3.5.3 FIR emission and spectral indices

The large survey at 330 MHz performed by the GMRT over the H-ATLAS Phase 1 fields (Mauch et al. 2013) allows one to determine whether spectral indices are somehow related to FIR luminosity. Spectral indices can be thought of as another *rough* proxy for radio source age. This is because, during the lifetime of a radio source, the electrons with the highest energies in a homogeneous magnetic field will radiate energy at a faster rate than their lower energy counterparts. This leads to a steepening of the spectral index at high frequencies. Thus, one might expect a negative relation between FIR luminosity and spectral index, if the radio source is somehow synchronised with the onset of star-forming activity.

In Fig. 3.9, I plot L_{250} versus radio spectral index for the subset of radio sources with detections at 330 MHz. Excluding flat-spectrum sources whose FIR emission may be contaminated by non-thermal emission ($\alpha < 0$), I find no evidence for any relation between spectral index and L_{250} in our sample of radio galaxies. The lack of a negative relation implies that either the star-forming and radio AGN activity are not well (or at all) synchronised in the current sample of radio galaxies (which would be somewhat at odds with what is seen in Section 3.5.2) or that this spectral index does not represent a good proxy for the age of these radio galaxies. It is also possible that the frequency range over which the spectral index is calculated is too low to see a relation between electron ageing and star formation. The ad-

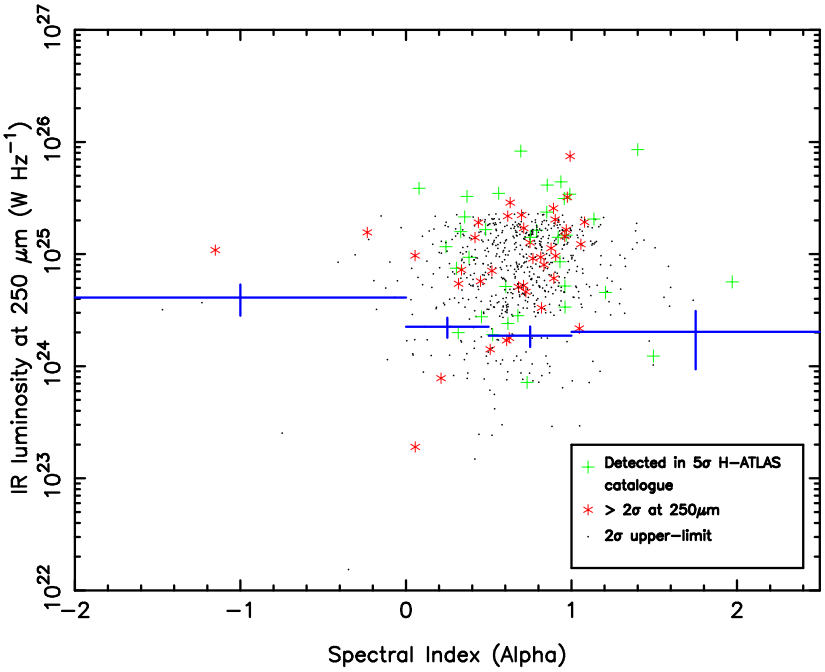

Figure 3.9: FIR luminosity at 250 μm versus the radio spectral index ($S \propto \nu^{-\alpha}$) for the subset of NVSS-detected sources (1.4-GHz) with GMRT detections (330 MHz).

dition of further data at radio frequencies, from which the shape of the spectral distribution could be reconstructed and thus modelled, may allow one to distinguish between the cases presented above.

3.6 Discussion

The most obvious trend observed in both the stacked radio-detected and comparison samples is the increase in the rest-frame luminosity at 250 μm with redshift. This is at least qualitatively consistent with previous results suggesting that dust masses and star-formation rates of radio galaxies evolve strongly with redshift (e.g. Archibald et al. 2001; Reuland et al. 2004). Perhaps the most interesting result from Section 3.5 is the different behaviour of the sub and super-1.5 L_K^* radio-detected samples with respect to their colour-matched comparison samples. While the 250 μm luminosity of the sub-1.5 L_K^* radio-detected sample is indis-

tinguishable from its comparison sample, the super-1.5 L_K^* radio-detected sample shows a strong FIR luminosity deficit with respect to its comparison sample. However, what does a deficit at 250 μm tell us about the physical properties of the host systems?

The answer may depend on the dust temperature. If the dust temperature of two matched samples are similar, any differences in the FIR luminosity will likely be due to differing dust masses. However, if the dust temperatures of both samples differ greatly, then any differences in the FIR luminosity will likely be due to differing SFRs. To calculate the dust temperature of the radio-detected and comparison samples, I use the temperatures generated by the best-fitting temperature method described in Section 3.4.5. The primary drawback of using this method is that a small number of bright, and possibly warm sources may dominate the χ^2 fitting, resulting in higher temperatures than one would expect by simple averaging. This implies that a minority of sources may be responsible for the majority of the temperature difference observed between samples.

Turning first to the results from the sub-1.5 L_K^* radio sample, I find that the fitted temperatures of the radio-detected and matched comparison samples are 20.5 ± 0.5 K and 19.0 ± 0.2 K, respectively. The combination of similar FIR luminosities and dust temperatures can be interpreted in several ways. For example it may simply mean that the radio jets, or the mechanism that leads to radio emission, are not strongly coupled to the dust reservoirs in all sub-1.5 L_K^* radio galaxies. Alternatively, it is possible the radio-detected sample contains at least two distinct populations, with different FIR luminosities, which are not well separated by stellar mass alone. As discussed in Section 3.1, HERGs are expected to be triggered as a result of on-going gas-rich major mergers. One might then expect the radio sources in this sample to show a strong 250 μm luminosity excess due to a combination of increased star-formation and higher dust masses. However, HERGs dominate the radio luminosity function only above $\sim 10^{26}$ WHz^{-1} (Best & Heckman 2012), well above the luminosity of most of

the sources in this sample. Thus, the sub-1.5 L_K^* radio-detected sample is likely to contain a mixture of HERGs and LERGs. This makes it difficult to be certain that the null result is due to similar dust masses and SFRs, as the presence of a small number of HERGs would render this interpretation invalid. Nevertheless, if one takes the sub-1.5 L_K^* radio-detected population as a whole, it is clear that there is no evidence for differing FIR luminosities or (at least isothermal) dust temperatures.

The super-1.5 L_K^* radio-detected sample shows a clear FIR luminosity deficit when compared to its colour-matched comparison sample. The suggestion here is that being radio-detected results in *lower* FIR luminosities. The fitted temperatures of the radio-detected and matched comparison sample are $16.2 \pm 0.5\,\mathrm{K}$ and $21.2 \pm 0.2\,\mathrm{K}$ respectively, implying that the observed differences may be due to a combination of lower dust masses and SFRs. One of the most obvious interpretations is that radio activity directly destroys dust or inhibit star formation in these galaxies. If this were the case, one might expect a negative relation between the mechanical heating of the ISM by the jets / lobes (which itself is dependent on the 1.4-GHz radio luminosity) and L_{250}. However, the relations converting 1.4-GHz radio luminosity to jet-power are calibrated for the halo of large clusters, not the ISM of galaxies in the field, making the use of such relations difficult (e.g. Bîrzan et al. 2004). The lack of a negative relation between the specific 250 μm luminosity and 1.4-GHz radio luminosity, suggests that a direct negative connection between the radio jet and the luminosity deficit at 250 μm is unlikely, although evolution in $L_{1.4\,\mathrm{GHz}}$ may have washed out any relation. In addition, using the total radio luminosity as opposed to the relevant part of the radio luminosity (i.e. that radiated from lobes in the ISM) may also mean that no relation is observed. If such a direct relation was real and ubiquitous, one might have expected to also see an L_{250} deficit in the sub-1.5 L_K^* radio-detected sample; that one does not, suggests we must look elsewhere for a potential solution.

All massive galaxies sit at the bottom of large, dense and hot potential wells. However, what distinguishes radio-detected systems from their non-radio-detected counterparts is that they inhabit the richest, hottest and densest of these environments. This is both because the radio activity is thought to be fuelled by the hot gas from the IGM and because hot gas is required to confine the radio lobes. This hot gas may ultimately lead to a suppression of the total dust content of any galaxy embedded in this environment. Radio lobes are known to drive shocks in the halos of their host galaxies, heating them (Boehringer et al. 1993; for a review see Fabian 2012). This heating has been used to solve the so called 'cooling flow problem', where only small amounts of cold gas are observed to condense out of hot-gas halos despite radiative cooling timescales which are much less than the age of the host (McNamara & Nulsen 2012). This leads to lower star-formation rates and therefore lower dust production rates. In addition, the hot gas may directly destroy, or simply suppress the formation of dust particles inside the galaxy though sputtering (Draine & Salpeter 1979). Further, any in-falling galaxy is likely to be ram-pressure stripped of its gas and dust content by the hot gas, limiting the alternative sources of cold gas and dust available to galaxies embedded in these environment (see Abramson et al. 2011 and Vollmer et al. 2012 for examples of ram stripping in the Virgo cluster). Thus, the tendency of massive ($>$1.5 L^*_K) radio galaxies to inhabit rich environments may explain the implied lower dust masses and SFRs observed in these systems, and the lack of such a result in the sub-1.5 L^*_K radio galaxies. However, there is a significant caveat to this interpretation: the non-radio detected sample must be overwhelmingly composed of sources which have not experienced radio-AGN activity for timescales greater or equal to the time it takes for any injected energy to cease influencing the FIR luminosity output of the galaxy. If this is not the case, then the comparison sample will contain sources which recently ceased to be radio detectable, but will still be experiencing quenching effects from the last episode of radio activity. Thus, one would expect little to no FIR luminosity differences to be observed between radio-detected and non-radio

detected galaxies. For the super-1.5 L_K^* sample, where IGM based feedback is expected to be at its most efficient, this is clearly not the case which either implies that the galaxies in the comparison sample have not experienced any radio-AGN activity for quite some time or that the observed FIR luminosity deficit is a short term phenomenon which lasts only as long as the radio AGN is switched on. In order to distinguish between both possibilities, it would be necessary to calculate the radio AGN duty cycle and compare it to the time it takes for the host's FIR to return to pre-triggering levels. This cannot be done with the current sample of radio AGN, as it is not complete.

Next, I turn to the results based on the radio source size. First, I note that the dust temperatures of compact radio sources, whether they are in the sub or super-1.5 L_K^* sample, are always higher than in their more extended counterparts. These higher temperatures are likely to be the result of increased star-formation activity in compact radio sources, a result reminiscent of the findings of Dicken et al. [2012], who showed that various indicators of star-formation activity were more likely to be seen in compact sources drawn from their small sample of powerful objects. There are two possible explanations for such a result. On the one hand, it may be that the small sources (< 30 kpc) are energetically coupled to the cold gas in their host galaxies, and drive star formation directly (i.e. the often invoked but poorly understood process of 'jet-induced star formation'; see Rees 1989, Begelman & Cioffi 1989, Gaibler et al. 2012). On the other hand, it may be that these young radio sources were triggered by an event, such as a merger, which also triggered a burst of star formation that will have died away by the time the sources are older and larger. Both models are somewhat at odds with the picture of LERGs (which are expected to make up the majority of sources in the both sample) as being quiescent systems with little cold gas available for star formation, but it is possible that the result is driven by a minority of compact HERGs. Further, the lack of a positive relation between the specific FIR luminosity and the 1.4-GHz radio

luminosity is surprising if radio-jet induced star-formation is occurring, although there are several reasons (mentioned above) why one might not expect to see a relation between these parameters. In any case, these results indicate an important relationship between radio-jet activity and star formation.

It is interesting to ask if the environmental explanation for the lower SFRs and dust masses of the super-1.5 L_K^* radio-detected sample can be strengthened using the results based on radio source sizes. This is a difficult question to answer as the relevant environmental parameters are gas temperature and density, not radio source size (although extended radio sources may simultaneously select more extended, hotter and possibly richer environments). Nevertheless, I attempt to combine both results in order to see whether a self-consistent picture can emerge. I combine the analysis by splitting the sub and super-1.5 L_K^* samples into two bins at 30 kpc (i.e. as a function of radio source size). On the top and bottom panels of Fig. 3.10, I plot the results for the sub and super-1.5 L_K^* samples relative to their colour-matched comparison samples. Stacks shown in red and blue represent compact and extended radio samples, respectively. Fitting a line with a gradient of zero to the sub-1.5 L_K^* subsamples, I find that compact and extended radio sources are 1.05 ± 0.19 and 0.68 ± 0.25 times as luminous at 250 μm as the colour matched comparison sample, with fitted temperatures of 22.2 ± 0.5 K and 13.5 ± 0.5 K respectively. Therefore, while the temperature difference is significant with high confidence, the luminosity difference is not due to large errors. Repeating the process with the super-1.5 L_K^* subsamples, I find that compact and extended radio sources are 0.66$\pm$0.15 and 0.26$\pm$0.12 times as bright at 250 μm as the colour-matched comparison sample, with fitted temperatures of 22.0$\pm$1.0 K and 12.2$\pm$0.5 K, respectively.

From these results, it is clear that the L_{250} deficiency in super-1.5 L_K^* radio-detected galaxies is driven primarily by extended sources with low dust temperatures. This is not altogether surprising, since it was obvious from the bottom panel of Fig. 3.8 that extended

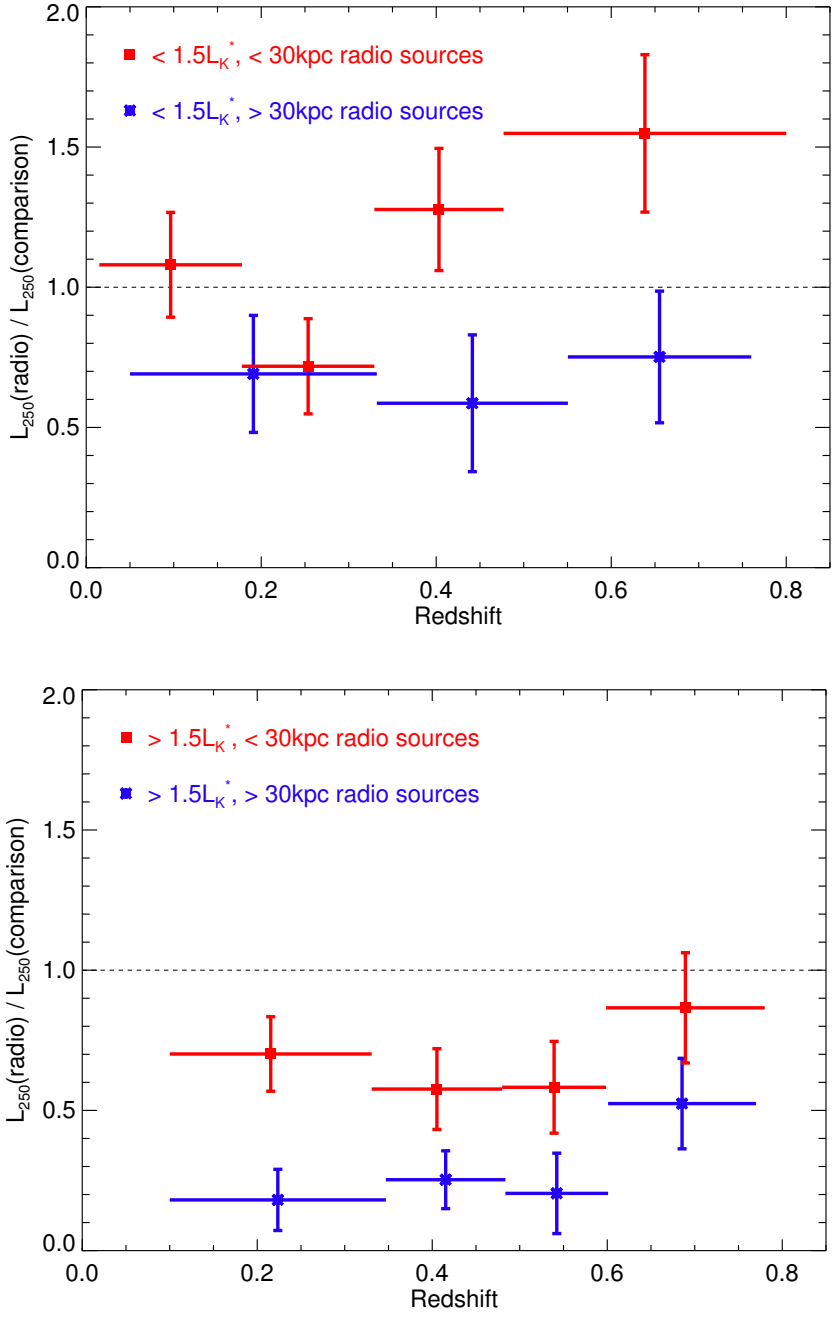

Figure 3.10: Stacked luminosities at 250 μm of the radio-detected samples divided by the colour-matched comparison samples. The sub-1.5 L_K^* (top) and super-1.5 L_K^* (bottom) radio-detected samples are separated into compact (<30 kpc) and extended (>30 kpc) radio galaxies. The red stacks represent the <30 kpc samples while the blue stacks represent the >30 kpc samples.

super-1.5 L_K^* radio-detected galaxies had lower FIR luminosities than their compact counterparts. Such a result is consistent with an environmental explanation for the suppression of L_{250}, as larger radio sources should, on average, select larger and denser halos than smaller radio sources. These results also suggest that if one accounts for the, presumably temporary jet-induced star-formation of compact radio sources, *all* massive radio sources have intrinsically lower FIR luminosities and temperatures, and therefore dust masses, than their non radio-detected counterparts. Our results suggest that massive radio-detected galaxies should have about 25% of the FIR luminosity of comparable non-radio-detected galaxies. This result is inconsistent with a direct causal link between the jet and the suppression of L_{250}, as one might expect lower 250 μm luminosities in compact sources relative to extended sources.

In order to verify that the environment regulates the FIR properties of radio galaxies, a careful study of the environment and its relation to the host's dust content and star-formation activity is needed. These results suggest that the FIR luminosities and temperatures of radio galaxies depend on the stellar mass as well as the radio source size. Understanding the origin of these dependencies will be useful for galaxy evolution models which often use the radio activity of galaxies to quench galaxy growth.

3.7 Conclusions

Using a large sample of radio galaxies selected in the *Herschel*-ATLAS Phase 1 area, I have investigated the FIR properties of the radio AGN population between $0.01 < z < 0.8$ by stacking the 100, 160, 250, 350 and 500 μm H-ATLAS maps in order to obtain stacked rest-frame luminosities at 250 μm and dust temperatures. The main results are:

1. I find no relation between the rest-frame luminosity at 250 μm divided by the K-band luminosity (i.e. the specific L_{250}), and the 1.4-GHz radio luminosity in this sample of radio-detected galaxies. This result implies that a galaxy's *nominal* radio luminosity

has little or no bearing on the star-formation rate and / or dust mass content of the host system. I stress that this does not imply that being radio-loud has no indirect or indeed direct effect on the FIR luminosity of the host system, just that the specific L_{250} has no dependence on the nominal value of the radio luminosity. A more suitable variable such as the work done on the ISM by the jet may yet show some sort of relation.

2. The rest-frame luminosity at 250 μm of radio-detected and comparison galaxies rises with increasing redshift. This is consistent with the view that most galaxies show signs of increased dust masses and star-formation activity at higher redshifts.

3. Compact radio sources (< 30 kpc) are associated with higher 250 μm luminosities than their more extended (> 30 kpc) counterparts. The fitted temperatures of compact and extended radio galaxies are 27.1 ± 0.3 K and 13.1 ± 0.3 K respectively, implying that an increased dust temperature in compact objects is responsible for this observation. The temperature difference suggests that there may be enhanced levels of star-formation in compact objects. However, whether this star-formation is directly (e.g. jet induced) or indirectly associated (e.g. merger driven) with radio-jets is not yet clear.

4. For matched samples in L_K and g′- r′, sub-1.5 L_K^* radio-detected galaxies have 0.89 ± 0.18 times the 250 μm luminosity of the matched-comparison sample, with fitted temperatures of 20.5 ± 0.5 K and 19.0 ± 0.2 K, respectively. Thus, taken as a whole, there is no evidence that sub-1.5 L_K^* radio-detected galaxies have different FIR properties to that of their non-radio-detected counterparts. Splitting the radio sample at 30 kpc, I find that compact and extended radio-detected galaxies have 1.05 ± 0.19 and 0.68 ± 0.25 times the 250 μm luminosity of the sub-1.5 L_K^* comparison sample, and have fitted temperatures of 22.2 ± 0.5 K and 13.5 ± 0.5 K respectively. Thus, although there is a suggestion of a FIR luminosity dependence on radio source size, large errors make it difficult to make this statement quantitatively. However, the observed temper-

ature difference does suggest that compact radio sources may have higher SFRs than their more extended counterparts.

5. For matched samples in L_K and g′- r′, super-1.5 L_K^* radio-detected galaxies have 0.49±0.12 times the 250 μm luminosity of the comparison sample, with fitted temperatures of 16.2 ± 0.5 K and 21.2 ± 0.2 K, respectively. These results imply that super-1.5 L_K^* radio-detected galaxies have lower dust masses and SFRs than their non-radio-detected counterparts. Splitting the radio sample at 30 kpc, I find that the compact and extended radio-detected galaxies have 0.66 ± 0.15 and 0.26 ± 0.12 times the 250 μm luminosity of the super-1.5 L_K^* comparison sample, and have fitted temperatures of 22.0 ± 1.0 K and 12.2 ± 0.5 K, respectively.

6. No relation between spectral index and the luminosity at 250 μm is found for the subset of 1.4-GHz radio sources with detections at 330 MHz. The lack of a negative relation implies that either star formation and radio AGN activity are not well (or at all) synchronised in the current sample of radio galaxies, or that spectral indices do not represent a good proxy for the age of our radio sources. Selecting a sample of merger-driven radio galaxies in which the FIR luminosity is dominated by on-going star formation (e.g. HERGs) may demonstrate whether any such relation exists in potentially 'synchronised' radio sources.

I explain the primary result, the L_{250} deficit seen only in the $> 1.5\,L_K^*$ radio galaxies, as an environmental phenomenon. Here, the suppression of L_{250} is likely due to the selection of LERG-like sources which are likely embedded in the hottest, densest and richest haloes, which the presence of radio jets and lobes selects for. The hot-gas environment acts to suppress the creation rate of dust particles in the ISM and / or actively destroy dust through sputtering. Ram-pressure stripping of any gas and dust rich galaxy falling into the halo would also limit external sources of gas and dust for these systems. This approach has the virtue of

explaining why an L_{250} deficit is seen in the $> 1.5\,L_K^*$ radio galaxies and not in the $< 1.5\,L_K^*$ radio galaxies, and why the L_{250} deficit might be more pronounced in extended rather than compact radio sources (i.e. there is a selection effect whereby the lobes of extended sources are confined and flux boosted in large, hot haloes, effectively selecting for such environments). In addition, it is consistent with the lack of a relation between the specific L_{250} and the 1.4-GHz radio luminosity, as the radio lobes will tend to keep the halo environment hot, with the long timescales for energy transfer washing out any direct relation. It also avoids timescale issues, which plague any attempt to directly link radio jets with positive or negative feedback, but assumes that the comparison sample is composed of objects which have not recently experienced radio AGN activity. One result which is difficult to account for is the systematically hotter temperatures in compact radio sources. This suggests enhanced SFRs in compact vs extended radio sources. However, under an environmental explanation, there is no reason to suppose a small amount of SF may be stimulated by the radio jets for short periods of time. Thus, the environment of radio galaxies is presented as a possible explanation for these results as it is the most consistent explanation. If one assumes that the higher FIR luminosities of compact radio galaxies are transient, as the FIR luminosities of extended radio galaxies suggest they are, then the FIR luminosity of *all* massive radio galaxies must be intrinsically lower than that of their non-radio-detected counterparts, implying systematically lower dust masses and SFRs. Thus, massive radio-detected galaxies may have only about 25% of the FIR luminosity of their non-radio-detected counterparts.

In this work, I have clearly demonstrated that the FIR properties of radio galaxies are not identical to that of the non radio-detected population. There is a strong FIR luminosity dependence on the stellar mass and a strong FIR luminosity and temperature dependence on the radio-source size. These conclusions are in disagreement with our earlier results from H10, where the FIR luminosities of radio-detected and non-radio-detected galaxies

were found to be indistinguishable. However, the small sample used in H10 (the present sample is more than eight times larger) prevented an analysis of the FIR properties of radio-galaxies as a function of stellar mass or radio source size. In addition, I have added best-fitting temperature estimates and PACS data in order to better interpret the origin of the FIR luminosity at 250 μm. I have attempted to explain our observations in terms of the special halo environment likely to be present around massive radio galaxies. If the environment plays a determinant role, I suggest that this is partly because of the continuous heating provided by multiple bursts of radio activity. This may ultimately create the conditions for systematically lower dust masses in radio galaxies. In order to prove this, a detailed study of the halo environment of radio galaxies and how it relates to the FIR properties of the host system, is required. The answer to these questions will be of great importance for models which use the radio activity of galaxies to quench galaxy growth.

The work presented here is only able to investigate sources between redshifts of $0.01 < z < 0.8$ because of the constraints imposed via the optical and NIR limits from the SDSS and LAS. In the near future, VISTA VIKING data, which is $\sim$1.4 mag. deeper than the LAS in the K-band, will become available, allowing more radio galaxies to be classified, increasing the sample size and extending the redshift range. Spectroscopic redshift campaigns, which target many of the sources not detected in the NIR, will help characterise the FIR / sub-mm properties of powerful high-z radio galaxies. The work presented here uses less than 25% of the full H-ATLAS survey area, implying that large gains in statistics can still be made.

Chapter 4

The dust temperatures of radio galaxies

4.1 Introduction

In this chapter, the dust temperature and the β parameter of radio galaxies will be examined in detail. Typical values for β vary between $1.0 < \beta < 2.0$. Since most far-infrared observations of galaxies sample the dust SED sparsely (e.g. 60 and 100 μm with IRAS, or 450 and 850 μm with SCUBA), the β parameter is often assumed. In this chapter, I calculate the best-fitting β value marginalised over temperature and normalisation for a large sample of radio galaxies, so that it may be assumed by those with sparse dust SED coverage for their samples of radio galaxies.

In this chapter, I also look for evidence of evolution in the dust temperature of radio galaxies. Previous studies of the dust temperature as a function of redshift indicate some level of positive evolution (e.g. Amblard et al. 2010; Hwang et al. 2010; Smith et al. *submitted* - hereafter S13), although bias resulting from the incomplete coverage of the dust SED has made it difficult to uniformly probe the temperature parameter space. In this chapter, I determine what constraints may be placed on the dust temperature of radio galaxies as a function of redshift, and whether the resulting temperatures differ from that of the general

H-ATLAS population.

In Chapter 3, 'compact' radio sources (< 30 kpc) were found to have both higher FIR luminosities and dust temperatures than 'extended' sources (> 30 kpc). These results suggested that the radio-jets may be inducing star-formation. In this chapter, I investigate this temperature dependency in more detail, and attempt to determine whether radio-jet induced star-formation is a plausible interpretation for these results.

In order to achieve these aims, I use the sample described in Section 3.3, with some differences. S13 showed that in the absence of 100 and 160 μm photometry, the derived dust temperatures from isothermal modified-blackbody χ^2 fitting are significantly biased towards colder temperatures. Therefore, sources without flux density information at 100 and 160 μm (71 - glitches in the PACS maps result in some sources not having flux density estimates) are excluded from the sample used here, leaving the sample with 1528 radio sources with photometry in all 5 *Herschel* bands (1389 radio galaxies after star-forming galaxies are removed using the same method as the one described in Section 3.4.3, i.e. sources with $q_{250} > 1.4$). Throughout this chapter, the flux densities from the PACS and SPIRE bands are extracted using the same method described in Section 3.4.1. I add an absolute flux calibration uncertainty of 10% (PACS) and 7% (SPIRE) in quadrature to the errors measured from the maps for the purposes of fitting. I also make an approximate correction for source confusion in the SPIRE bands by subtracting the mean, derived from the maps, from the flux density measurements. This is a sufficient correction for random source confusion as long as any of the derived results are not based on a few sources. Correlated confusion is not corrected for, and as such, the temperatures which follow may be affected by clustering around radio galaxies.

The outline of this chapter is as follows. In Section 4.2 I describe the method used to calculate the best-fitting β and dust temperature for the sample of radio galaxies. In Section 4.3, I search for evolution in the dust temperature of radio galaxies. In Section 4.4, I determine

whether incompleteness in the K-band causes temperature bias in the sample. In Section 4.5 and 4.6, I try to determine whether jet-induced star-formation is a plausible explanation for the temperature and luminosity vs radio-size trends found in Chapter 3. Finally, in Section 4.7, I summarise the main results and conclude.

4.2 Characteristic β and T values for radio galaxies

4.2.1 Choosing a beta parameter

In this section, I detail the method used to calculate the β parameter and the dust temperatures. For the sources in the sample, modified isothermal blackbody-fitting was performed using the following equation,

$$f_v \propto \frac{\nu^{3+\beta}}{e^{\frac{h\nu}{kT}} - 1}, \tag{4.1}$$

where T represents the isothermal temperature of the source in question, ν is the frequency, k is the Boltzmann constant, h is the Planck constant and β is the beta parameter. This model differs from the traditional Planck law in that it incorporates information related to the dust grain composition (e.g. grain composition and size) via the β parameter. Ideally, one would allow β and T to vary simultaneously, however, a strong anti-correlation exists between the two parameters. This anti-correlation is thought to be driven by noise in the photometric data (see Shetty et al. 2009a,b & S13). For a sample of simulated sources with known β and T values, and with the same flux density criteria used to select sources for the formal H-ATLAS 5σ catalogue, S13 found a strong anti-correlation between both parameters (see Fig. 4.1). The sample presented here has fewer sources, and flux densities with lower signal-to-noise ratios than the one presented in S13. Therefore, allowing β and T to vary simultaneously would likely result in extremely poor constraints. To solve this problem, an

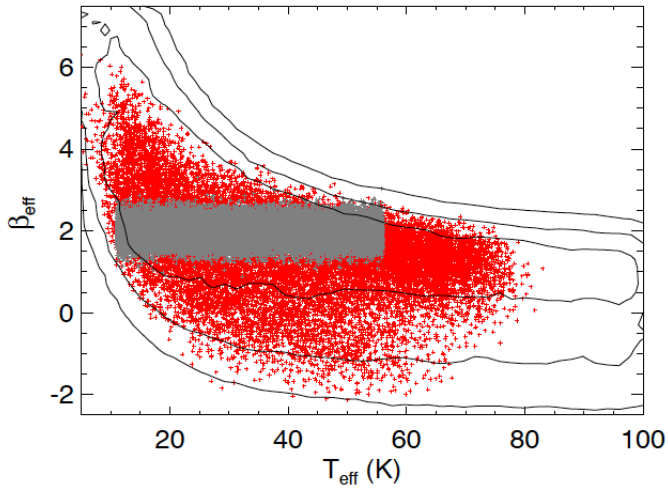

Figure 4.1: Beta versus the effective dust temperature. Grey points are the input β and $T_{\rm eff}$ values from the 5σ simulated H-ATLAS catalogue. Red points are the median likelihood estimate after χ^2 fitting where β and T are allowed to vary simultaneously. The contours denote the 68, 95 and 99% confidence levels (Fig. 4 of Smith et al. *submitted*).

alternative method developed in S13 and Hardcastle et al. [2013] (hereafter, H13) may be used, where β is estimated by marginalising over the normalisation and temperature of all the sources in the sample, and then fixed.

This was done using the following method. At every beta between 1.0-2.5 (in steps of 0.025), I calculate and sum the χ^2 values from all the sources in the sample, using the best-fitting temperatures for that beta value (i.e. I marginalise over temperature; T is allowed to vary between 5-60 K as in S13). This results in a χ^2 distribution as a function of β, from which one can pick the β with the lowest χ^2 value. The errors are calculated by finding the values of the 16^{th} and 84^{th} percentile limits, after converting the χ^2 distribution to a probability distribution function (PDF) assuming $P(\beta) \propto \exp^{(\frac{-\chi^2}{2})}$.

Such an approach led S13 to calculate a best-fitting β value of 1.98 ± 0.02 for the 5σ H-ATLAS sample and H13 to calculate a best-fitting β value of 1.8 for a similarly selected sample of radio galaxies to the one presented here. The β PDF for this sample is shown in Fig. 4.2. The best-fitting β value is 2.05 ± 0.07. The β PDF in Fig. 4.2 is not completely

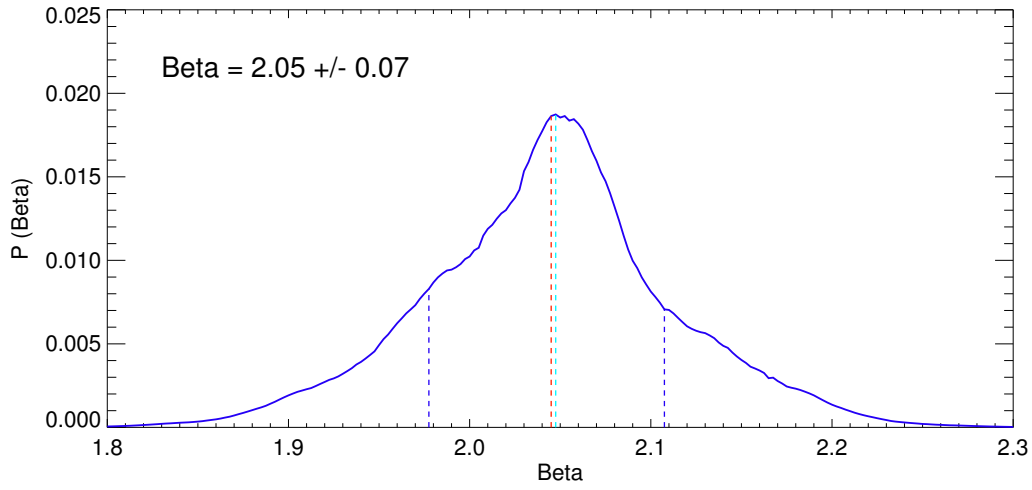

Figure 4.2: PDF of the β parameter marginalised over temperature and normalisation for the radio galaxy sample (star-forming sources have been excluded). Dashed blue lines represent the 16^{th} and 84^{th} percentile limits. The best-fitting and median values are shown via the cyan and red lines, respectively.

Gaussian; this is probably because relatively few sources contribute disproportionally to the β constraints. Nevertheless, the fact that the best-fitting and median values are indistinguishable indicates that this is not a significant problem. More importantly, a β value of 2.05 ± 0.07 is in agreement with the results of S13, H13 and from other major *Herschel* surveys such as Hi-GAL[1] (Paradis et al. 2010), KINGFISH[2] (Galametz et al. 2012b) and HeViCS[3] (Davies et al. 2012).

4.2.2 The dust temperature of radio galaxies

Having established the best-fitting β value for the radio sample ($\beta = 2.05$), I now calculate the characteristic dust temperature of the whole sample, fixing β and marginalising over the normalisation. Total χ^2 values were calculated for temperatures between 5 and 60 K in steps of 0.01 K. The results are shown in Fig. 4.3. The best-fitting temperature is $24.84^{+0.21}_{-0.18}$ K with

[1]The *Herschel* Infrared GALactic plane survey; Molinari et al. 2010
[2]Key Insights on Nearby Galaxies: a Far-Infrared Survey with *Herschel*; Kennicutt et al. 2011
[3]The *Herschel* Virgo Cluster Survey; Davies et al. 2010

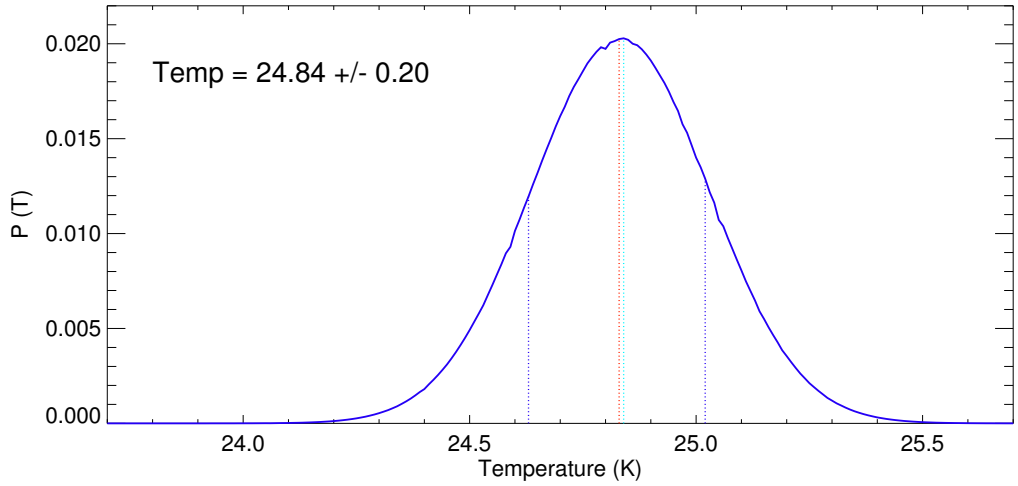

Figure 4.3: PDF of the dust temperature of radio-selected AGN. Dashed blue lines are the 16^{th} and 84^{th} percentile limits. The best-fitting and median values are shown via the cyan and red lines, respectively.

a reduced χ^2 of 1.58. It is important to note that the temperature error is not the dispersion (i.e. the spread one might get if the temperature of individual sources were constrained), but rather the error on the best-fitting temperature which represents all the sources in that bin. The median is temperature is 24.83 K. This is a few kelvin hotter than the observed temperatures for the general 250 μm selected H-ATLAS population (22.3 ± 0.1 K; S13), which mostly consists of star-forming galaxies. This might be expected if AGN heating of the ISM plays a role. However, this sample is expected to be predominantly made up of LERGs, and as such, little AGN emission is expected except at radio wavelengths. This leaves the radio jets themselves as the most likely source of heating. However, the samples do cover different redshift ranges, making this temperature difference difficult to interpret without an analysis of the redshift dependence.

The characteristic isothermal modified-blackbody values for this sample of radio galaxies are $\beta = 2.05$ and $T = 24.84$ K. The β parameter is constrained using the largest sample of radio galaxies to date. The characteristic temperature, which assumed $\beta = 2.05$, may

be assumed for the purposes of K-correcting single band FIR luminosities. However, the validity of assuming such a value for the K-correction depends on the extent to which there is temperature evolution in radio galaxies. Therefore, in the following section, I investigate the dust temperature as a function of redshift.

4.3 The dust temperature as a function of redshift

It is interesting to determine whether the dust temperature of radio galaxies evolves with redshift. If it does, it would help determine which temperature(s) to assume for the K-correction of single band FIR luminosities. In general, the dust temperatures of most galaxies are expected to increase with redshift, as the SFR of most galaxies were higher in the past (e.g. Madau et al. 1996). To investigate this, the radio-detected sample is split into 6 bins in redshift, each containing roughly the same number of sources (~ 230), and the dust temperatures calculated. The K-S probabilities of the sample in each of the 5 *Herschel* bands are shown in Table 4.1. Nearly all the fluxes in the SPIRE bands are well distinguished from a sample of fluxes drawn randomly from the maps (i.e. the K-S probability is $< 1\%$), however, most of the fluxes in the PACS bands are not well distinguished from the background. As noted by S13, the presence of PACS data - even non-detections - is important to avoid temperature bias in the temperature fitting algorithm used here. The PDF of each redshift bin is shown in Fig. 4.4, and the temperatures of all the stacks as a function of redshift are shown in Fig. 4.5. To help interpret these values, the temperature evolution relation found by S13 for the H-ATLAS detected population is shown as a solid red line, with the dispersion shown by the dotted red-lines. For the radio galaxies, the dust temperature increases steadily with redshift with the exception of the last redshift bin.

In combination with the results from Chapter 3, where it was shown that the 250 μm

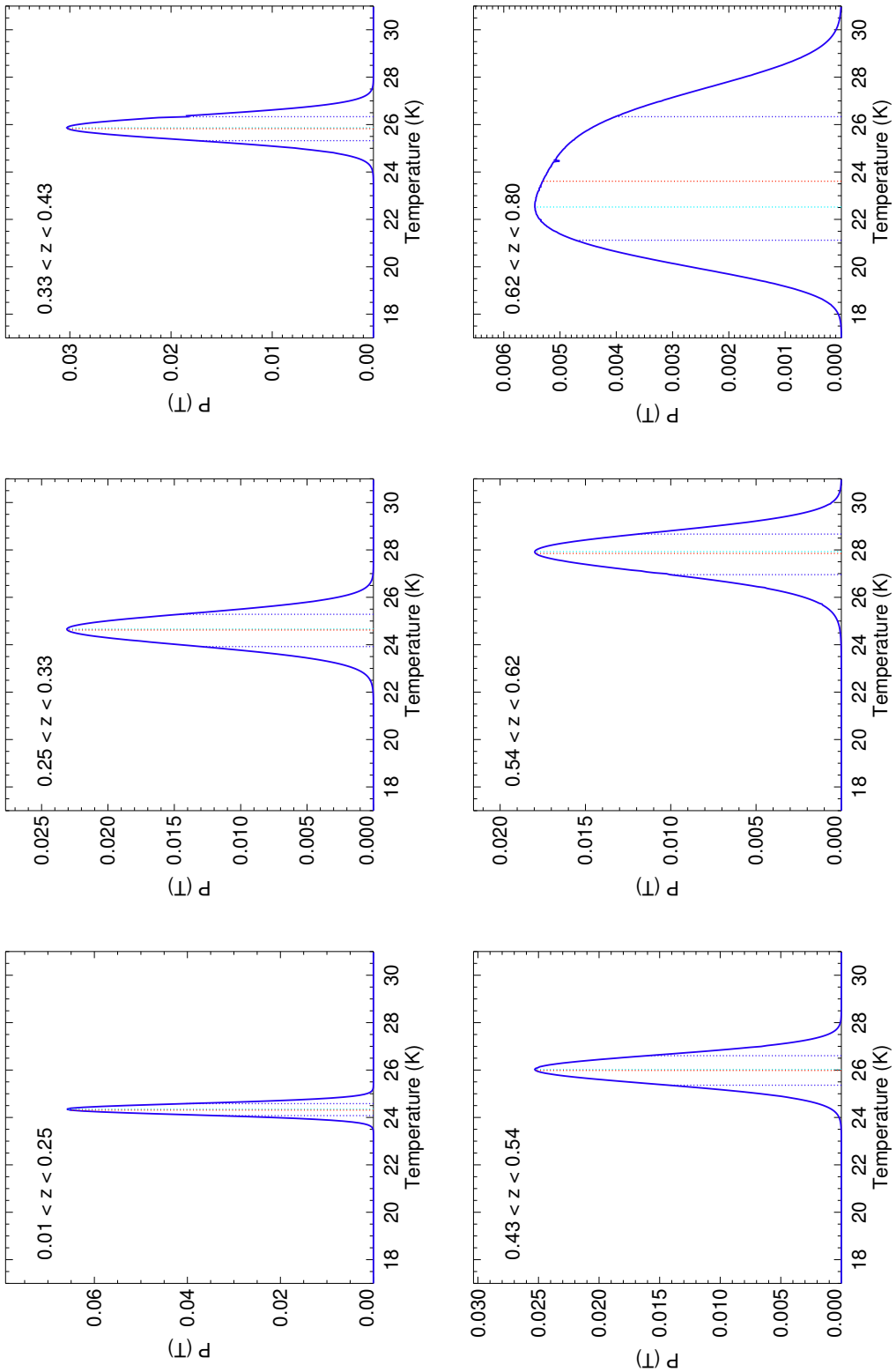

Figure 4.4: PDFs of the dust temperature for each redshift bin. Colour coding is the same as Fig. 4.3.

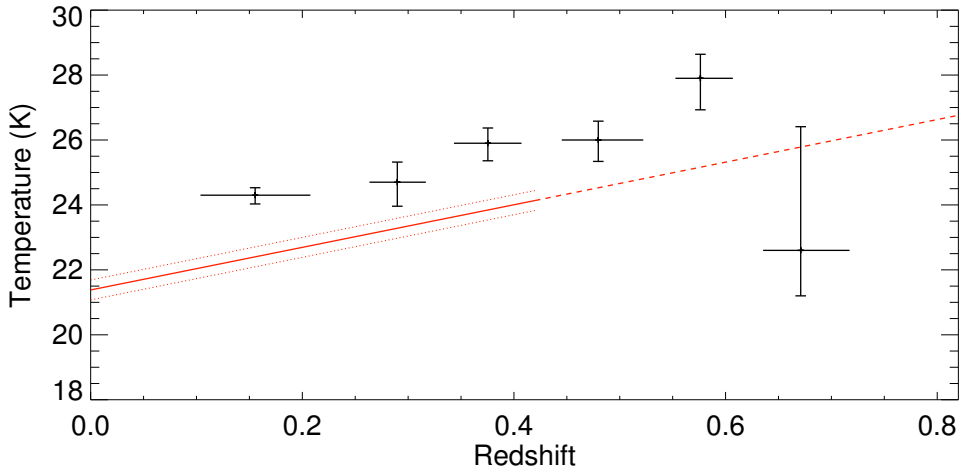

Figure 4.5: The temperature of radio-detected (shown in black) galaxies shown as a function of redshift. The solid red line is the relation from S13 and the dotted red line is the dispersion. The relation from S13 has only been calculated to $z = 0.42$, therefore, the dashed red line is the extrapolation of the relation.

luminosity increases with redshift, one can infer that radio galaxies had more gas and dust and higher SFRs in the past. It is also apparent that radio galaxies are consistently warmer than the star-forming sample presented in S13. This is somewhat surprising, given that this sample is expected to be dominated by 'traditional' elliptical radio galaxies (e.g. LERGs) which are not expected to host much star-formation. Since LERGs show little evidence for AGN emission except at radio wavelengths, it is reasonable to assume that the radio jets and lobes may be heating the ISM, and possibly stimulating small amounts of star formation. To help determine whether this is the case, in Section 4.5 and Section 4.6, I investigate how the dust temperature varies with projected radio source size and 1.4-GHz radio luminosity. However, it is first important to determine whether the sample contains biases which are affecting the results. In the next section, I investigate the dust temperature as a function of K-band luminosity to see if incompleteness in stellar mass is biasing the derived dust temperatures.

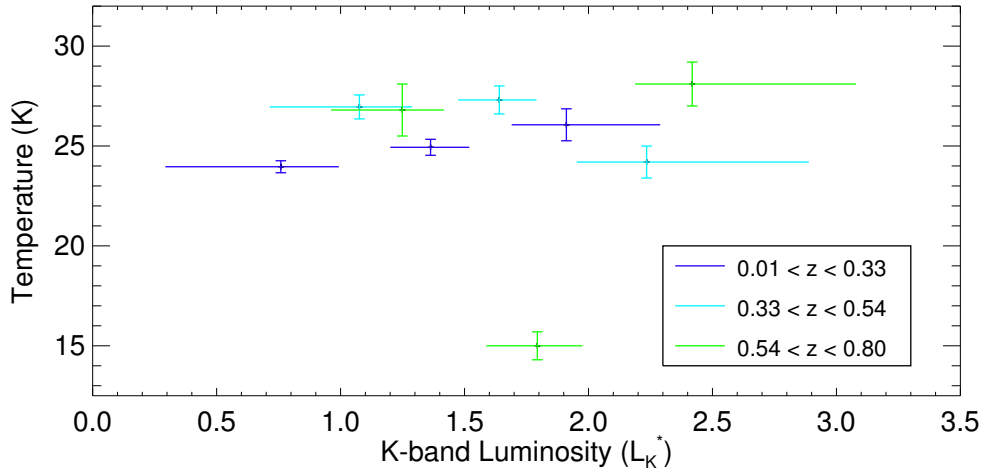

Figure 4.6: The temperature of radio galaxies shown as a function of K-band luminosity. The radio sample has been split into three redshift bins.

4.4 The dust temperature as a function K-band luminosity

The radio sample used in this chapter is K-band magnitude limited. In other words, faint K-band luminosity galaxies drop out as we move to higher redshift. This may cause subtle, but significant temperature biases in the sample of radio galaxies. In this section, the dust temperature is plotted against the K-band luminosity for three redshift bins in order to understand this bias. The redshift bins are: $0.01 < z < 0.33$, $0.33 < z < 0.54$ and $0.54 < z < 0.80$. The redshift bins are chosen so that approximately the same number of sources are present in each bin (~ 465). In addition, each redshift bin is split into 3 K-band luminosity separated sub-bins each also containing approximately the same number of sources (~ 155). The K-S statistics for the bins, shown in Table 4.2, reveal that the SPIRE bands are generally well-distinguished from a sample of randomly selected flux densities whereas the PACS bands are not.

In Fig. 4.6, the dust temperature is plotted against K-band luminosity normalised by $L^*_K = 7.87 \times 10^{10} L_\odot$ (see Section 3.3.1 for how this value was calculated). First, it is clear that the temperatures are mainly situated between 24 K and 29 K, consistent with the

temperature-redshift results of Section 4.3. Somewhat surprisingly, the 2^{nd} stack of the highest redshift bin has a temperature of 15 K, though this may be due to a lack of bright FIR/sub-mm sources in that bin. Indeed, the flux density averages of all the *Herschel* bands of that bin are particularly low when compared to those of the other samples (see Table 4.2). In terms of temperature bias due to selection effects, the redshift and K-band luminosity binning does not suggest that this is a serious problem. The average from all the three stacks is: 25.0 ± 1.5, 26.2 ± 2.4 and 23.3 ± 10.2 (where the error is calculated by finding the value which is the square-root of the sum of the squared differences from the mean).

These temperatures are consistent with the results of Bourne et al. [2012], who find that optically red and green galaxies show no evidence for a temperature relation with stellar mass. However, their temperatures cluster around 15 K for red galaxies and 15-25 K for green galaxies. It seems clear that radio-detected galaxies have higher temperatures than that of non-radio-detected galaxies, and that these temperatures are consistent with Bourne et al. [2012]'s green galaxies. In the following sections, I try to understand why this is using the projected radio size and the radio luminosity.

z range	Objects in bin	Mean bin flux density (mJy)					K-S probability (%)				
		SPIRE bands			PACS bands		SPIRE bands			PACS bands	
		250 μm	350 μm	500 μm	100 μm	160 μm	250 μm	350 μm	500 μm	100 μm	160 μm
0.00 – 0.25	234	18.5 ± 0.4	7.2 ± 0.5	4.7 ± 0.6	31.8 ± 2.0	34.5 ± 2.5	$< 10^{-3}$	$< 10^{-3}$	$< 10^{-3}$	$< 10^{-3}$	$< 10^{-3}$
0.25 – 0.33	221	5.7 ± 0.4	1.5 ± 0.5	3.0 ± 0.6	7.2 ± 2.0	2.7 ± 2.5	$< 10^{-3}$	0.02	1.7	8.4	69.6
0.33 – 0.43	241	7.0 ± 0.4	1.5 ± 0.5	2.4 ± 0.5	5.1 ± 2.0	9.7 ± 2.5	$< 10^{-3}$	0.002	0.2	36.4	0.6
0.43 – 0.54	224	6.3 ± 0.4	2.5 ± 0.5	3.1 ± 0.6	-0.3 ± 2.0	6.0 ± 2.5	$< 10^{-3}$	0.004	0.4	68.4	18.5
0.54 – 0.62	220	4.8 ± 0.4	1.6 ± 0.5	2.8 ± 0.6	0.4 ± 2.1	5.4 ± 2.6	$< 10^{-3}$	0.002	0.1	60.9	31.2
0.62 – 0.80	248	4.9 ± 0.4	2.0 ± 0.5	4.0 ± 0.5	0.9 ± 2.0	3.7 ± 2.6	$< 10^{-3}$	$< 10^{-3}$	$< 10^{-3}$	8.9	3.8

Table 4.1: Mean bin flux densities and K-S probabilities that the *Herschel* fluxes of radio-loud objects in redshift bins are drawn from the background distribution, as a function of wavelength. Low probabilities (below 1%) imply significant differences between the bin being considered and the distribution of flux densities measured from randomly selected positions in the sky, as described in the text. Redshift bins are identical to the stacks used in Fig. 4.5.

L_K range	Objects in bin	Mean bin flux density (mJy)					K-S probability (%)				
		SPIRE bands			PACS bands		SPIRE bands			PACS bands	
		250 μm	350 μm	500 μm	100 μm	160 μm	250 μm	350 μm	500 μm	100 μm	160 μm
$0.01 < z < 0.33$											
0.00 – 1.10	155	20.1 ± 0.5	7.4 ± 0.6	4.4 ± 0.7	36.1 ± 2.4	38.4 ± 3.1	$< 10^{-3}$	$< 10^{-3}$	0.05	$< 10^{-3}$	$< 10^{-3}$
1.10 – 1.60	153	11.7 ± 0.5	4.4 ± 0.6	4.0 ± 0.7	18.6 ± 2.4	12.1 ± 3.0	$< 10^{-3}$	$< 10^{-3}$	0.1	0.9	3.4
1.60 – 4.70	154	5.0 ± 0.5	1.3 ± 0.6	3.0 ± 0.7	4.7 ± 2.4	5.3 ± 3.0	0.03	0.03	0.4	11.9	33.8
$0.33 < z < 0.54$											
0.00 – 1.40	149	9.5 ± 0.5	2.6 ± 0.6	4.1 ± 0.7	7.0 ± 2.4	10.6 ± 3.0	$< 10^{-3}$	0.03	$< 10^{-3}$	15.0	1.7
1.40 – 1.85	152	5.5 ± 0.5	1.9 ± 0.6	2.5 ± 0.7	3.2 ± 2.5	14.5 ± 3.1	0.1	0.1	4.0	86.0	0.2
1.85 – 4.70	163	5.3 ± 0.5	1.7 ± 0.6	2.0 ± 0.7	-1.2 ± 2.4	-0.3 ± 3.0	$< 10^{-3}$	0.02	9.8	92.3	68.6
$0.54 < z < 0.80$											
0.00 – 1.50	159	6.5 ± 0.5	3.0 ± 0.6	4.8 ± 0.7	0.5 ± 2.5	10.0 ± 3.2	$< 10^{-3}$	$< 10^{-3}$	$< 10^{-3}$	33.5	9.6
1.50 – 2.05	154	2.6 ± 0.5	0.3 ± 0.6	2.6 ± 0.7	-1.9 ± 2.6	-0.1 ± 3.2	0.003	0.3	0.4	55.6	34.7
2.05 – 4.70	150	4.9 ± 0.5	1.9 ± 0.6	2.7 ± 0.7	1.4 ± 2.5	3.1 ± 3.2	$< 10^{-3}$	$< 10^{-3}$	2.2	65.2	26.2

Table 4.2: Mean bin flux densities and K-S probabilities that the *Herschel* fluxes of radio-loud objects in redshift bins are drawn from the background distribution, as a function of wavelength. The binning is identical to the stack sizes used in Fig. 4.6.

4.5 The dust temperature as a function of radio source size

In this section, I explore whether there is any evidence for radio-jet feedback on the dust temperature of radio galaxies. If the ISM properties are independent of radio jets, no relation between the ISM properties and radio sizes is expected. However, in Chapter 3 the FIR luminosity was found to weakly depend on the projected radio size. Furthermore, the temperatures of 'extended' radio sources (> 30 kpc; 13.1 ± 0.3 K) were found to be significantly lower than those of 'compact' radio sources (< 30 kpc; 27.1 ± 0.3 K) (for comparison, the half-light radius of massive ellipticals is ~ 20 kpc; McLure et al. 2004). The origin of this relation was unclear. It was suggested that a small number of compact HERGs drove the trends. In H13, the FIR luminosities and temperatures of a well selected sample of HERGs and LERGs was studied (see Appendix A for an overview of the author's contribution to this work - and an in-depth discussion of the FIR luminosities and temperatures of HERGs and LERGs). H13 found that HERGs might well contribute to the luminosity dependence; however, the temperature dependence on radio sizes was found for both HERGs and LERGs. This indicated that HERGs were not solely responsible for the temperature differences observed between 'compact' and 'extended' radio galaxies. In the case of HERGs, it is plausible to link the falling dust temperatures with declining SFRs after some event which triggers both radio activity and star formation. However, recent results suggest such triggering scenarios are not particularly well synchronised (e.g. Tadhunter et al. 2011; Dicken et al. 2012). In the case of LERGs, where little AGN emission is expected other than at radio wavelengths, the existence of a temperature dependence on projected radio size suggests that the radio jets themselves are the source of the heating. In other words, while the radio jets are in the ISM, they mechanically heat it. In order to understand the dust temperature dependence on radio sizes more fully, the current radio sample is split into 6 bins each containing approximately the same number of sources (~ 204). Sources with limits on their radio sizes are excluded

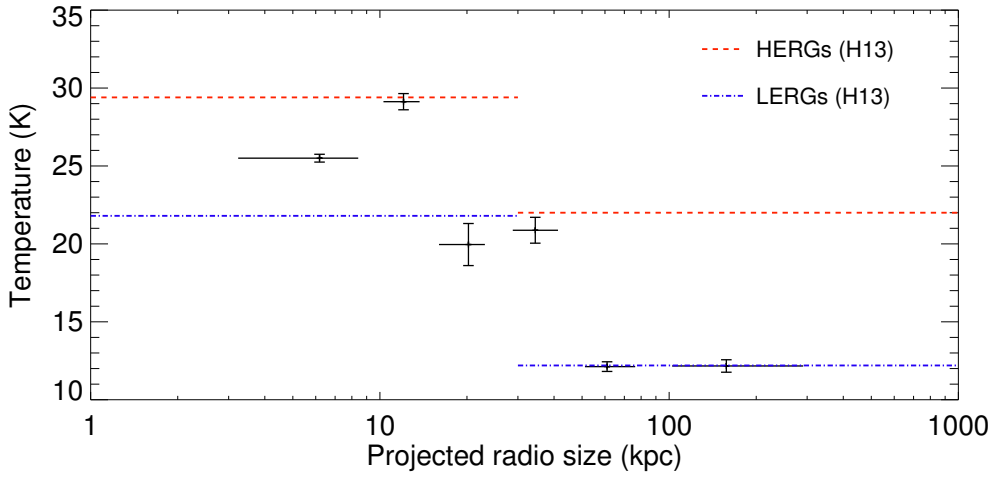

Figure 4.7: Dust temperature versus radio source size (excluding sources with length limits). Black points represent the temperatures generated from the radio sample presented in this chapter. Temperature estimates for LERGs (blue) and HERGs (red) from H13 are also plotted.

from the analysis (i.e. 167 sources were excluded). In Fig. 4.7, the dust temperature is shown as a function of projected radio size. The PDFs of the stacks is shown in Fig. 4.8 and the K-S statistics for the radio galaxy sample is shown in Table 4.3.

It is clear from Fig. 4.7 that the dust temperature falls steadily from $\sim 25 - 30\,\mathrm{K}$ at small radio sizes ($\sim 10\,\mathrm{kpc}$) to $\sim 12\,\mathrm{K}$ at large radio sizes ($\gtrsim 50\,\mathrm{kpc}$). The temperatures of the two smallest radio size bins are higher than that of the LERG population, suggesting the presence of a few HERGs in those bins. In contrast, the two largest radio size bins are fully consistent with a LERG-only population. The higher dust temperatures point to higher SFRs in compact radio galaxies. Finding evidence for jet-induced star-formation in a LERG dominated sample is somewhat surprising, and does not fit well with our picture of LERGs as hot-gas fuelled AGN with little or no star-formation activity. However, simulations of radio jet / lobe - ISM interactions suggest that clumps of gas can be compressed (stimulating star-formation) or destroyed (quenching star-formation) (Gaibler et al. 2012). Irrespective

of whether large amounts of star-formation is induced, the energy injected into the ISM probably leads to significant heating. A 'back of the envelope' timescale for this heating may be calculated if one assumes that that the radio lobes travel at approximately $0.01c$, and that the any heating effects disappear after the lobes are $\sim$40 kpc from one another (see Fig. 4.7). This implies feedback durations of $\sim 10 - 20$ Myr. To help understand whether radio activity is responsible for the observed trends, in the next section I investigate the temperature dependence of radio sources as a function of radio luminosity in combination with radio sizes.

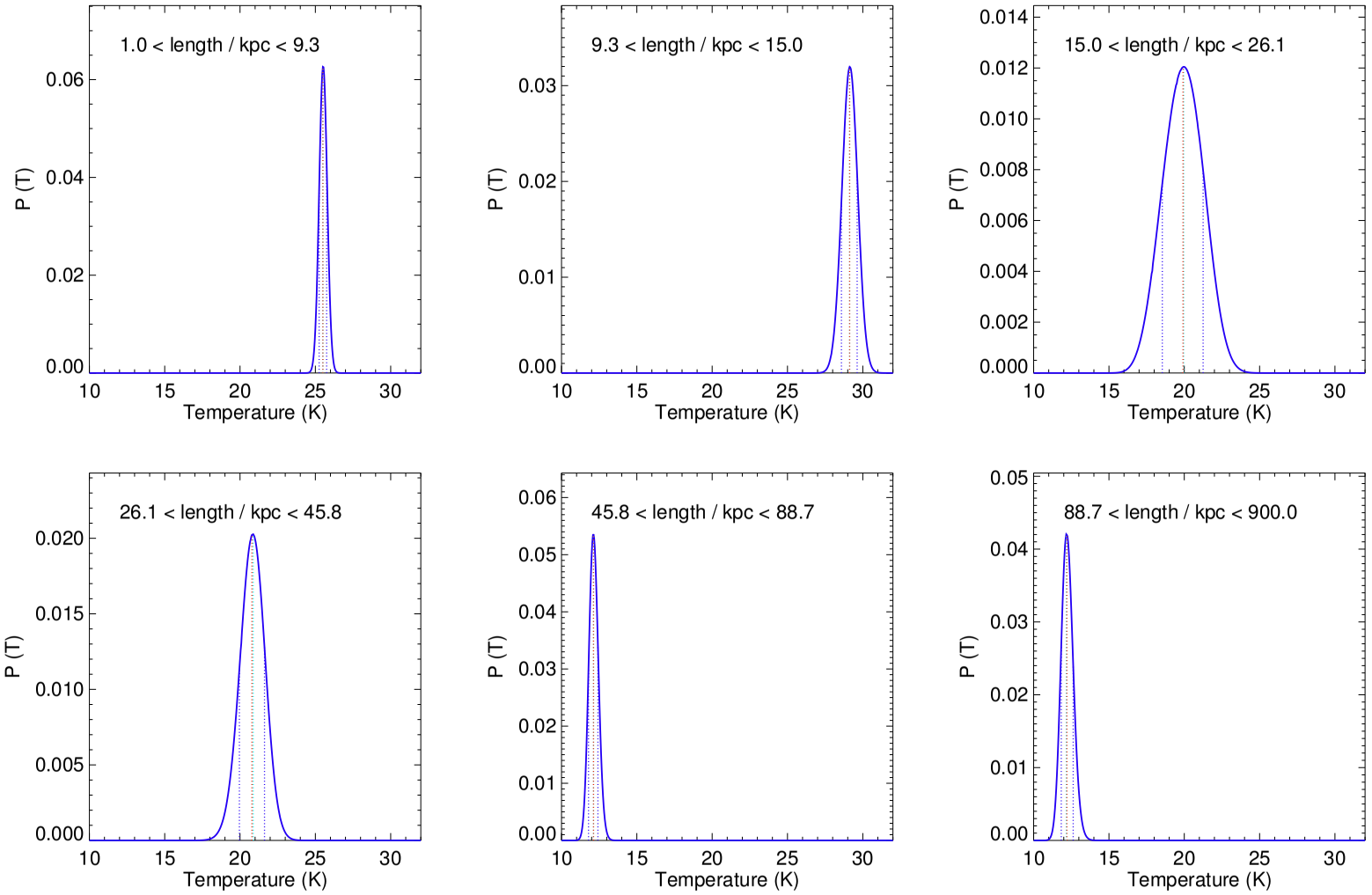

Figure 4.8: Dust temperature PDF of each bin as a function of projected radio size. Colour code is identical to that of Fig. 4.3.

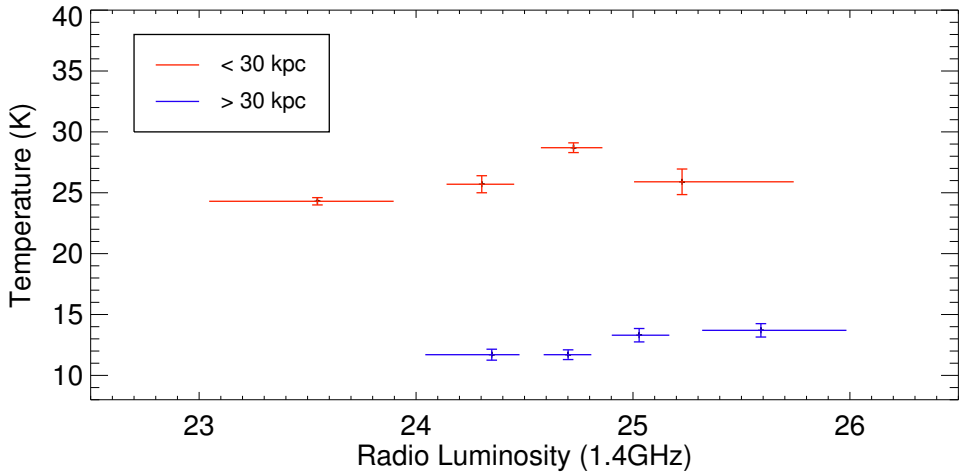

Figure 4.9: The dust temperature of compact (red) and extended (blue) radio-detected galaxies shown as a function of 1.4-GHz radio luminosity.

4.6 The dust temperature as a function radio luminosity

If the ISM is mechanically heated by radio jets / lobes, the dust temperature might be expected to increase with radio luminosity, since jet power is related to radio luminosity.

The radio sample is split into compact and extended radio sources, defined as being those which are above and below 30 kpc, respectively. Next, the dust temperature is calculated as a function of 1.4-GHz radio luminosity, with each sub-sample being split into 4 bins with roughly the same number of sources ($\sim$ 150). If ISM heating is due to radio jets, a relatively strong positive temperature trend should be observed in the compact sample and no trend observed in the extended sample. The results are shown in Fig. 4.9. The K-S statistics for the bins in Fig. 4.9 are shown in Table 4.4. Firstly, it is clear that, as expected, compact sources have systematically higher temperatures than extended sources. However, no strong positive trend is observed as a function of 1.4-GHz radio luminosity for the 'compact' sample, presenting a problem for a positive feedback scenario. Fitting a straight line to the compact and extended radio samples gives a gradient of 2.9 ± 0.4 and 1.9 ± 0.6 kelvin per unit redshift, respectively. However, the reduced χ^2 for the compact

and extended radio samples is 5.62 and 0.82, respectively. Therefore, a straight line is not a good model for the compact radio source data. Furthermore, even though the gradient from the compact radio sample is higher than that of the extended sample, the difference is only 1.0 ± 0.7, making this difference statistically insignificant. However, it is known that the radio luminosity is not necessarily a good tracer of jet power, as the radio luminosity undergoes significant luminosity evolution even for a source of fixed kinetic power (e.g. Kaiser, Dennett-Thorpe & Alexander 1997). In addition, the total radio luminosity has been used, whereas ideally, one should only use that part of the radio emission confined within the ISM (i.e. radio lobes). In Chapter 5, I show that the core component (emission restricted to a few pc) of the radio luminosity in a small sample of high redshift radio AGN varies from 0-100%. For these reasons, it is perhaps not surprising that no strong positive temperature trend is found in the sample of compact radio galaxies. Nevertheless, it is clear that the dust temperature is linked to radio AGN emission.

4.7 Conclusions

I have investigated the dust temperatures of 1389 radio sources over the *Herschel*-ATLAS Phase 1 area have been investigated using PACS and SPIRE photometry. The main results are:

1. The best-fitting β parameter, calculated by marginalising over the temperature and normalisation of all the radio galaxies in the sample, is $\beta = 2.05 \pm 0.07$. Using this β value, the best-fitting temperature is calculated, and is found to be $T = 24.84 \pm 0.20$ K.

2. The dust temperatures of radio sources increase with redshift, and are consistently higher than the temperatures of the H-ATLAS population presented in S13. This implies that radio jets may be heating the ISM through AGN feedback.

Radio Size (kilo-parsec)	Objects in bin	Mean bin flux density (mJy)					K-S probability (%)				
		SPIRE bands			PACS bands		SPIRE bands			PACS bands	
		250 μm	350 μm	500 μm	100 μm	160 μm	250 μm	350 μm	500 μm	100 μm	160 μm
0.0 – 9.3	202	22.2 ± 0.4	8.5 ± 0.5	5.7 ± 0.6	36.3 ± 2.1	34.9 ± 2.6	$< 10^{-3}$	$< 10^{-3}$	$< 10^{-3}$	$< 10^{-3}$	$< 10^{-3}$
9.3 – 15.0	202	8.3 ± 0.4	2.5 ± 0.5	3.4 ± 0.6	10.0 ± 2.2	10.5 ± 2.7	$< 10^{-3}$	$< 10^{-3}$	0.003	10.2	1.0
15.0 – 26.1	204	5.7 ± 0.4	2.1 ± 0.5	3.3 ± 0.6	-3.2 ± 2.2	7.0 ± 2.7	$< 10^{-3}$	$< 10^{-3}$	0.09	58.2	1.4
26.1 – 45.8	204	2.2 ± 0.4	-0.9 ± 0.5	0.5 ± 0.6	-1.2 ± 2.1	-0.3 ± 2.7	0.1	12.7	31.0	73.7	87.6
45.8 – 88.7	202	2.9 ± 0.5	2.3 ± 0.5	4.4 ± 0.6	-1.4 ± 2.2	4.5 ± 2.7	$< 10^{-3}$	0.001	0.004	53.7	0.3
88.7 – 900	208	3.2 ± 0.4	0.9 ± 0.5	2.7 ± 0.6	2.4 ± 2.0	2.1 ± 2.6	$< 10^{-3}$	0.09	1.7	0.6	10.1

Table 4.3: Mean bin flux densities and K-S probabilities that the *Herschel* fluxes of radio-loud objects in redshift bins are drawn from the background distribution, as a function of wavelength. Size bins are the identical to those shown in Fig. 4.7.

$L_{1.4}$ range	Objects in bin	Mean bin flux density (mJy)					K-S probability (%)				
		SPIRE bands			PACS bands		SPIRE bands			PACS bands	
		250 μm	350 μm	500 μm	100 μm	160 μm	250 μm	350 μm	500 μm	100 μm	160 μm
< 30 kpc											
21.00 – 24.05	166	19.0 ± 0.5	6.8 ± 0.6	4.5 ± 0.7	31.3 ± 2.3	33.0 ± 3.0	$< 10^{-3}$	$< 10^{-3}$	0.002	0.002	$< 10^{-3}$
24.05 – 24.51	164	5.6 ± 0.5	0.8 ± 0.6	2.1 ± 0.7	3.6 ± 2.3	9.7 ± 2.9	$< 10^{-3}$	9.6	2.2	81.5	1.8
24.51 – 24.92	166	12.7 ± 0.5	5.0 ± 0.6	4.1 ± 0.7	13.5 ± 2.4	13.8 ± 3.0	$< 10^{-3}$	$< 10^{-3}$	0.005	33.6	27.2
24.92 – 27.20	160	8.6 ± 0.5	3.7 ± 0.6	5.8 ± 0.7	3.2 ± 2.5	9.7 ± 3.1	$< 10^{-3}$	$< 10^{-3}$	$< 10^{-3}$	24.7	1.1
> 30 kpc											
21.00 – 24.55	144	3.2 ± 0.5	1.3 ± 0.6	3.3 ± 0.7	-2.4 ± 2.6	2.7 ± 3.2	0.01	0.07	1.1	97.8	5.4
24.55 – 24.85	143	1.4 ± 0.5	-0.8 ± 0.6	2.2 ± 0.7	3.2 ± 2.5	4.4 ± 3.1	5.1	9.0	2.7	10.9	4.1
24.85 – 25.25	142	2.4 ± 0.5	1.7 ± 0.6	2.1 ± 0.7	0.1 ± 2.7	-1.9 ± 3.3	0.010	0.004	0.7	65.0	67.0
25.25 – 27.20	136	3.0 ± 0.5	0.6 ± 0.6	2.1 ± 0.7	0.0 ± 2.5	1.8 ± 3.2	0.006	0.3	29.7	2.3	12.1

Table 4.4: Mean bin flux densities and K-S probabilities that the *Herschel* fluxes of radio-loud objects in redshift bins are drawn from the background distribution, as a function of wavelength. Luminosity bins are the identical to those shown in Fig. 4.9.

3. The dust temperatures of the radio galaxies show little to no relation with the K-band luminosity. This implies that stellar mass is relatively unimportant in determining the dust temperature of radio galaxies.

4. The dust temperatures of radio galaxies show a strong negative dependence with the projected radio size. This suggests that while the radio jet is inside the ISM, it is mechanically heating it. This heating may result in increased SFRs for $\sim 10-20$ Myrs.

5. The dust temperature of radio galaxies is investigated as a function of 1.4-GHz radio luminosity. Since the radio luminosity is expected to be related to the kinetic jet power, the sample is first sub-divided into compact and extended radio galaxies. I find that the increase in temperature as a function of redshift for compact and extended radio galaxies are statistically indistinguishable.

The aims of this chapter were two fold. First, to calculate β and T values which could be assumed for dust SED fitting and / or K-correcting single band FIR luminosities for similarly selected samples of radio galaxies. Secondly, to look for evolution and / or evidence of radio-jet induced star-formation. Temperature evolution as a function of redshift is found, in agreement with the result of S13. The dust temperature is found to depend strongly on the projected size of the radio source, in the sense that compact sources have much higher temperatures than extended ones. A potential explanation for this is jet-induced star-formation, although an analysis of the rate of increase of the dust temperature as a function of radio luminosity for the compact and extended samples did not reveal any significant differences between the samples. To conclusively show whether jet-induced star-formation is real, the ISM confined radio luminosity (e.g. lobe luminosity) should be investigated as a function of dust temperature and luminosity. Better statistics will also help lower errors in any future analysis of the kind undertaken here.

From the analysis presented in this chapter, it is clear that the that radio jets and lobes may well alter ISM properties on a population-wide level. High resolution studies of the ISM properties of a few galaxies with and without radio jets is needed to help clarify the situation. Such studies may help establish if the work done by the radio jets on the ISM has a transitory or permanent effect.

Chapter 5

The FIR properties of a pilot sample high-redshift radio-detected AGN

5.1 Introduction

In this chapter, I discuss the properties of seven high-z ($z \gtrsim 1$) radio-loud AGN. There are two primary goals: first, to demonstrate a methodology for identifying some of the highest redshift, and therefore most luminous objects in the *Herschel*-ATLAS data set, and second, to search for evidence of direct radio-jet feedback.

In order to select high-redshift objects, I use a combination of near-IR K-band data from the LAS, and 1.4-GHz radio data from the NVSS and FIRST. This involves selecting radio sources with no associated K-band counterpart. Through the $K - z$ relation, described in detail in Section 1.4.3.2, radio sources which are not detected in the K-band are likely to be at higher redshift rather than simply faint, low-redshift objects. This chapter aims to show that it is viable to create a sample of high-z radio sources with reliable 5-sigma H-ATLAS detections.

Additionally, evidence for radio-jet induced star-formation will be investigated. As it stands, it is unclear how jet propagation through the ISM affects important parameters such as the SFR, FIR luminosity and dust temperature. With regard to positive feedback, there is some theoretical (e.g Begelman & Cioffi 1989, Mellema, Kurk & Röttgering 2002, Gaibler et al. 2012) and some observational (e.g. van Breugel & Dey 1993, Dey et al. 1997) evidence for a process whereby the lobes stimulate star-formation by compressing clumps of gas and dust, providing the conditions for gravitational collapse. However, negative feedback is expected if the leading edge of the lobe simply scatters dense clumps of gas. The contribution, and thus importance of radio-jet induced star formation to the total stellar mass of a galaxy is uncertain. The hosts of traditional elliptical radio-galaxies are not expected to show much evidence for star formation, let alone jet-induced star formation. However, at higher redshifts, radio-loud quasars do show evidence for systematically higher SFRs than radio-quiet quasars (e.g. Kalfountzou et al. 2012). Nevertheless, determining whether the higher SFRs are the result of radio activity and confirming whether positive feedback is ubiquitous in radio galaxies may help clarify the nature of the 'starburst radio-AGN' connection found in other studies (Archibald et al. 2001; De Breuck & Reuland 2003; Reuland et al. 2004; Hickox et al. 2013). To investigate the possibility of radio-jet induced star formation, I calculate the radio AGN luminosity, that is, the radio luminosity after contributions from the star-formation process has been removed, and compare it to the SFR. Such an analysis will also reveal how important it is to account for the star-formation component of the radio luminosity.

In summary, with FIR data from the H-ATLAS and optical spectroscopy, in this chapter I look for evidence of feedback, or the lack thereof, by calculating the dust temperatures and SFRs of seven high-redshift sources. Sources at high-redshift are chosen so that an

investigation of the most extreme FIR emitting radio-AGN may be undertaken. If feedback is real and ubiquitous, then one might expect to see some evidence for it in these sources.

5.2 Sample selection

To select a sample of high-redshift radio-loud AGN, I use the radio catalogue described in Chapter 2 as the parent catalogue. Below, key features of the catalogue are described.

The catalogue was generated by cross-matching K-band LAS images with all the NVSS sources in the *Herschel*-ATLAS phase 1 area. The positional accuracy of the matches was improved by using FIRST data (c.f. FWHM of the FIRST and NVSS beams are $5''$ and $45''$, respectively). This resulted in the accurate classification of 5426 radio sources, with $S_{1.4\,\mathrm{GHz}} > 3\,\mathrm{mJy}$. Since the sources presented here are drawn exclusively from the 9^{hr} and 15^{hr} phase 1 fields, the targets are actually drawn from a smaller subset of 4485 NVSS sources. The depth of the LAS is $K = 18.0$ magnitude which, assuming the $K - z$ relation (Willott et al. 2003), implies that radio sources fainter than this are at $z \gtrsim 1.3$. Therefore, to ensure that the objects are at high-z, radio sources which were matched to LAS sources with $K > 18.0$[1] magnitude or were not matched to the LAS at all (i.e. undetected), were selected. This reduced the parent sample from 4485 to 2452 radio sources. Next, I cross-matched the sample with the 5σ H-ATLAS point source catalogue on a $4''$ best-match basis (c.f. the 1σ positional error for H-ATLAS sources detected at 5σ is $2.4''$; Rigby et al. 2011b). This resulted in 54 matches.

The next step was to calculate the probability / expected number of spurious matches in the sample. Using the H-ATLAS catalogue, I calculated that there are 636.55 sources per sq degree, which translates to 4.911702×10^{-5} sources per sq arcsec. Assuming an area of

[1] The depth of the LAS is not uniform across all the images, meaning that a few sources with $K > 18.0$ will be detected

50.26 sq arcsec (i.e. a circle with a radius of $4''$), I find the probability of a single spurious match to be 2.468×10^{-3} (or 0.25%). The size of the input catalogue used to generate the matched sample was 2452, meaning that one can expect ~ 6 random associations. The matched sample has 54 sources, therefore approximately 11% of the sources are expected to be spurious matches. I attempted to remove spurious matches by eyeballing the K-band / radio overlays of each match. In particular, I attempted to determine if the H-ATLAS association in each of the overlays was in fact related to a non-radio-detected LAS source. I did this using the reliability criterion developed in Smith et al. [2011] (see Section 3.2). I found this to be the case for 3 sources, implying that $\sim 5.6\%$ of the remaining sample (or ~ 3 sources) might have been spuriously matched.

Of the remaining 51 sources, 18 were targeted with the *Intermediate dispersion Spectrograph and Imaging System* (ISIS) on the *William Herschel Telescope* (WHT) in order to gain optical spectra for redshift determination. The brightest radio sources were observed first, although time and visibility constraints meant this was not always possible. During the data reduction procedure, I identified a subset of 9 sources with emission lines and therefore redshifts. Of these nine, only seven are presented here due to legacy reasons[1]. If available, I include NIR-radio overlays using VISTA[2] VIKING[3] data. Although it is possible that one or more of the radio sources may have been erroneously matched to the FIR emission, I consider this to be unlikely as the probability of a spurious match is only 1 in 20 (i.e. 5.6%).

The properties of the sample are shown in Table 5.1. Flux densities at 330-MHz from the GMRT are included (Mauch et al. 2013). Where available, I use these fluxes to calculate the spectral index[4] of the radio sources. If no GMRT flux is present (i.e. undetected by the

[1]The remaining two sources were not fully reduced since they were not targets of a VLBI observation campaign, the results of which were originally included in this chapter

[2]Visible and Infrared Survey Telescope for Astronomy

[3]VISTA Kilo-Degree Infrared Galaxy Survey

[4]Where the spectral index is defined as $S \propto \nu^{-\alpha}$

Name	H-ATLAS ID	RA [J2000]	DEC [J2000]	z	$S_{1.4\mathrm{GHz}}$ (mJy)	$S_{0.33\mathrm{GHz}}$ (mJy)	$\alpha_{0.33}^{1.4}$	$L_{1.4\mathrm{GHz}}$ ($\mathrm{W\,Hz^{-1}}$)
JV09_386	G09.v2.11402	09:04:26.791	+01:54:48.730	2.372	2.16±0.14	10.51±1.96	1.09	9.22×10^{25}
JV09_627	SDP_6345.0	09:08:11.974	-00:21:10.240	1.123	6.10±0.15	10.88±1.77	0.40	2.34×10^{25}
JV15_307	G15.v3.17345	14:09:30.229	+00:38:04.540	2.044	19.45±0.16	38.31±6.93	0.47	2.75×10^{26}
JV15_1825	G15.v3.2158	14:34:05.215	-00:23:04.216	1.565	159.82±0.21	602.6±20.93	0.92	1.91×10^{27}
JV15_2441	G15.v3.21609	14:45:19.210	+00:55:28.160	0.923	8.35±0.14	-	0.8	2.98×10^{25}
JV15_2513	G15.v3.1183	14:46:08.873	+02:17:47.010	3.084	6.71±0.14	22.32±7.69	0.83	4.36×10^{26}
JV15_2527	G15.v3.24249	14:46:18.463	-00:42:53.490	1.029	6.69±0.14	-	0.8	2.92×10^{25}

Table 5.1: Properties of the sample. The RA and DEC correspond to the yellow crosses in Figs. 5.1 to Figs. 5.7. Spectral indices are calculated using the 1.4-GHz and 330-MHz fluxes where available. In the absence of 330-MHz data, a spectral index of 0.8 is assumed.

survey), I assume a spectral index of 0.8, a value which is representative of the general radio source population. This was the case for two sources, JV15_2441 and JV15_2527. A value of 0.8 is consistent with GMRT non-detections as the region occupied by both sources was particularly noisy.

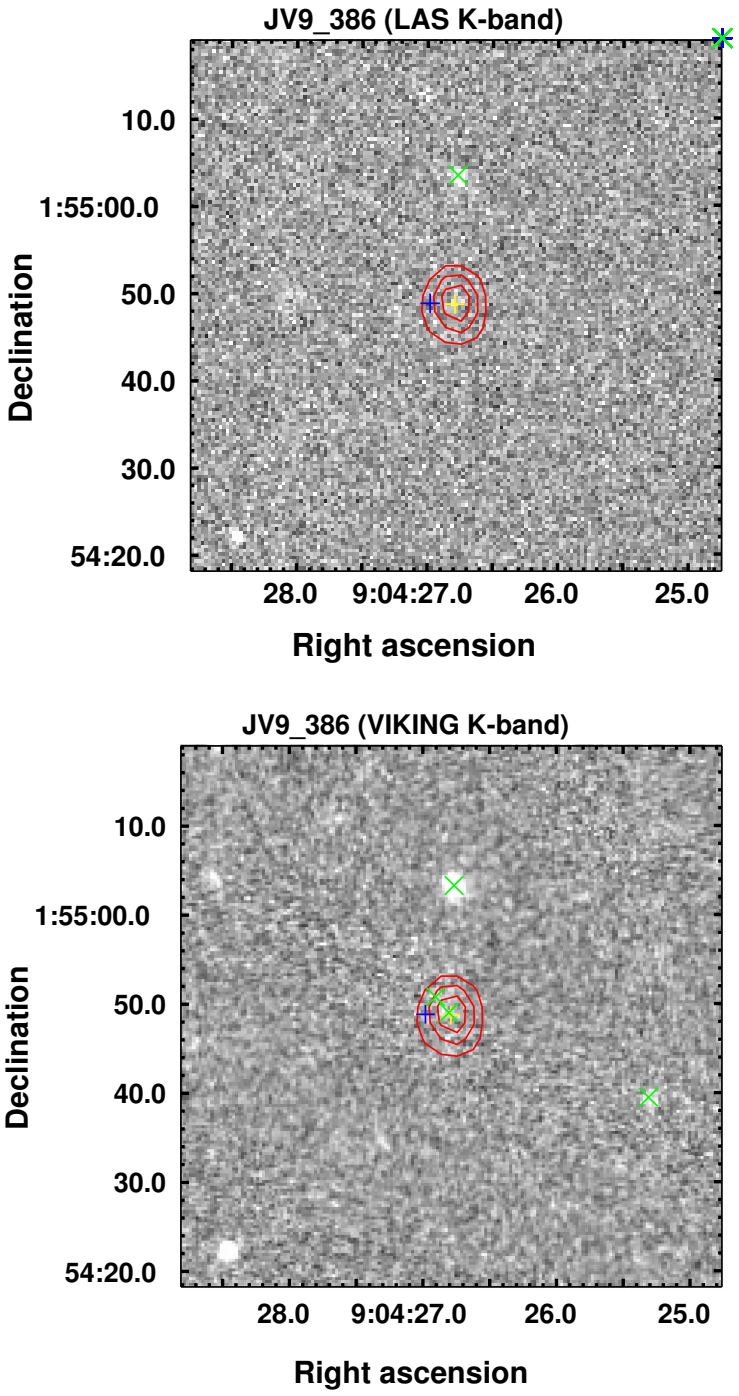

Figure 5.1: K-band LAS (top) / VIKING (bottom) - radio overlays for source JV09_386. Contours in red are from FIRST and are at (0.5, 1, 1.5, 2, 5, 10, 20, 50) mJy / beam (the rms of FIRST is 0.2 mJy / beam). Formal H-ATLAS and LAS / VIKING detections are represented as blue '+' and green 'X' marks, respectively. The yellow '+' sign represents catalogued FIRST position of the radio source.

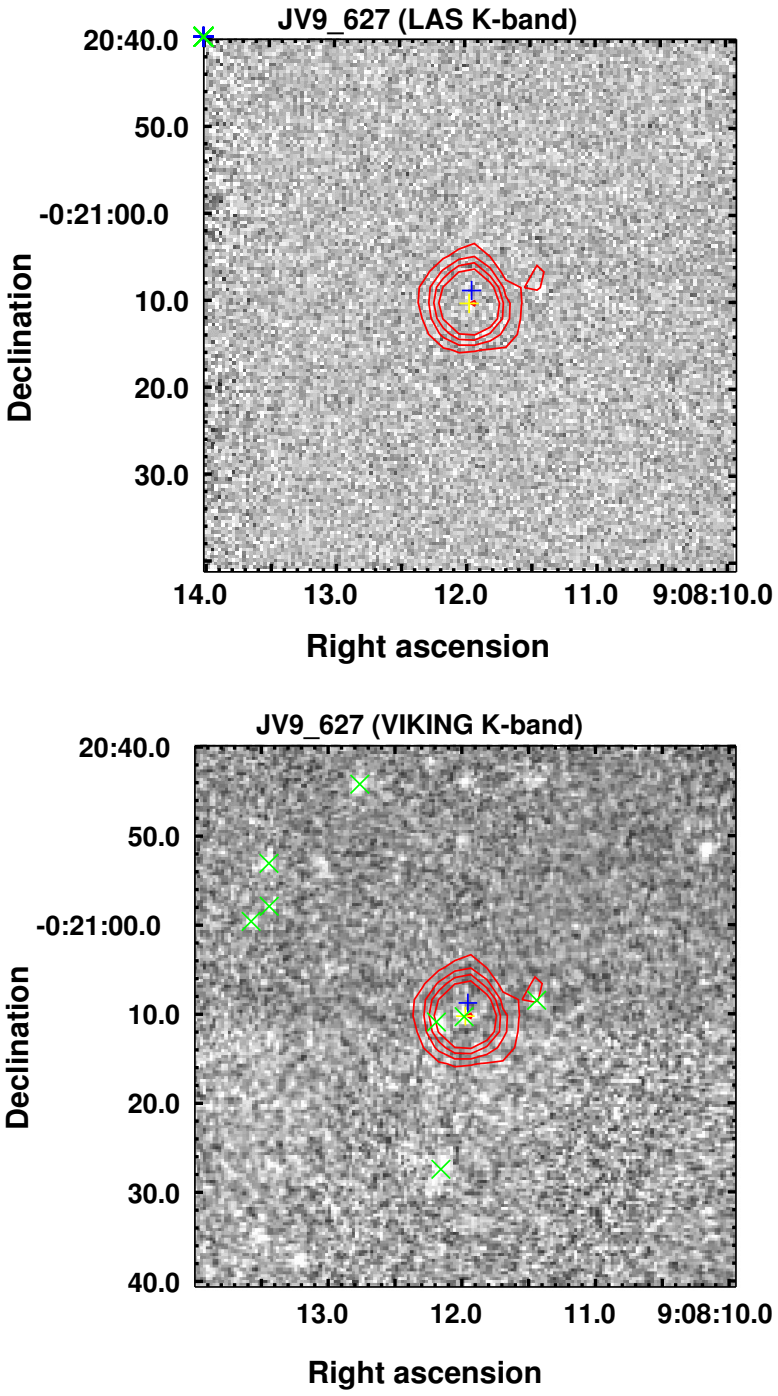

Figure 5.2: K-band LAS (top) / VIKING (bottom) - radio overlays for source JV09_627. Contours in red are from FIRST and are at (0.5, 1, 1.5, 2, 5, 10, 20, 50) mJy / beam (the rms of FIRST is 0.2 mJy / beam). Formal H-ATLAS and LAS / VIKING detections are represented as blue '+' and green 'X' marks, respectively. The yellow '+' sign represents catalogued FIRST position of the radio source.

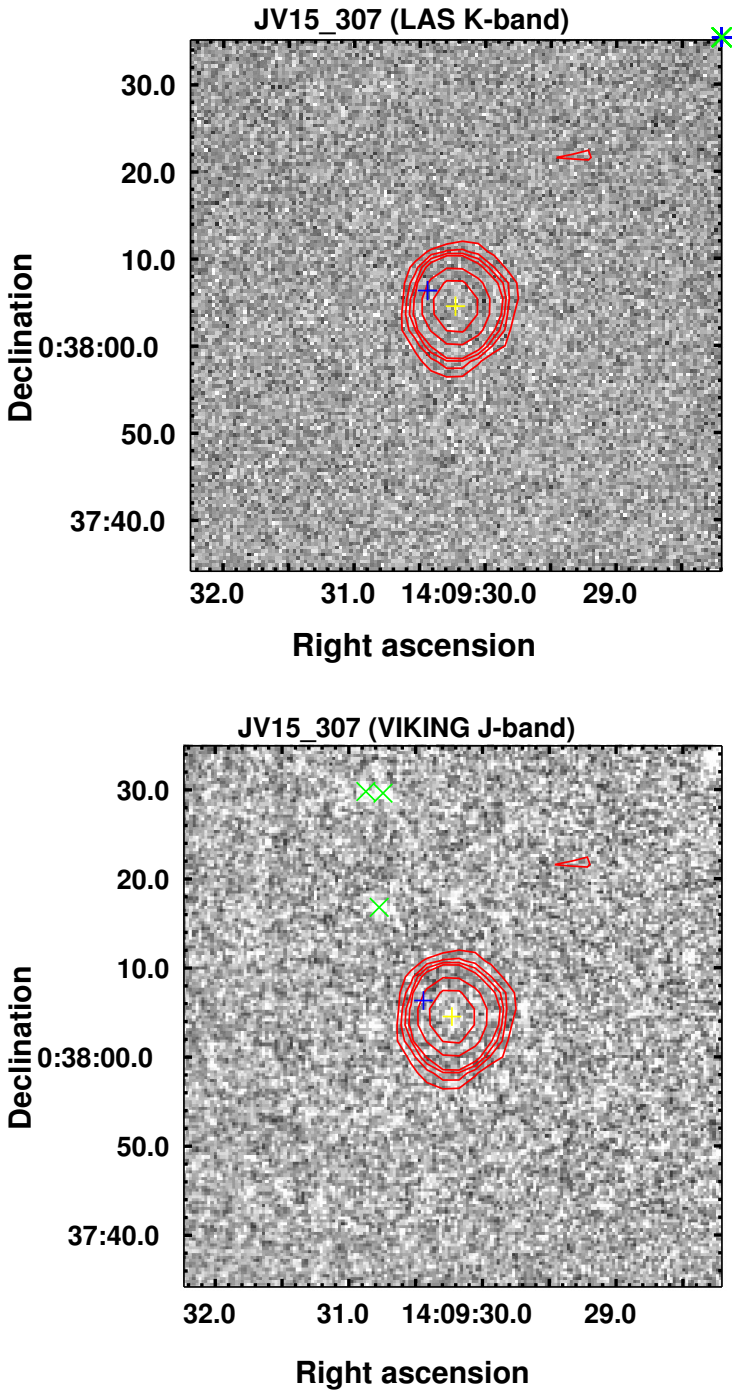

Figure 5.3: K-band LAS (top) / J-band VIKING (bottom) - radio overlays for source JV15_307. Contours in red are from FIRST and are at (0.5, 1, 1.5, 2, 5, 10, 20, 50) mJy / beam (the rms of FIRST is 0.2 mJy / beam). Formal H-ATLAS and LAS / VIKING detections are represented as blue '+' and green 'X' marks, respectively. The yellow '+' sign represents catalogued FIRST position of the radio source.

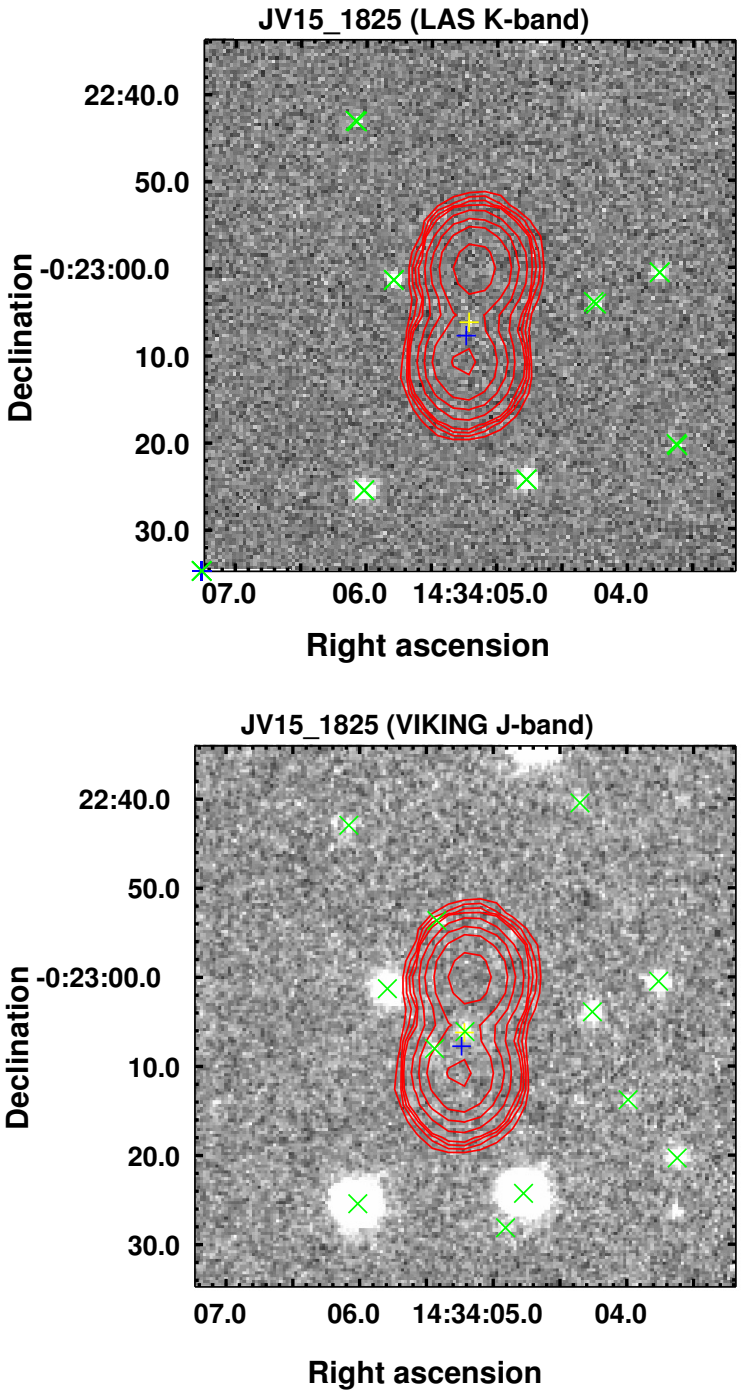

Figure 5.4: K-band LAS (top) / J-band VIKING (bottom) - radio overlays for source JV15_1825. Contours in red are from FIRST and are at $(0.5, 1, 1.5, 2, 5, 10, 20, 50)$ mJy / beam (the rms of FIRST is 0.2 mJy / beam). Formal H-ATLAS and LAS / VIKING detections are represented as blue '+' and green 'X' marks, respectively. The yellow '+' sign represents the best guess as to the position of the radio source.

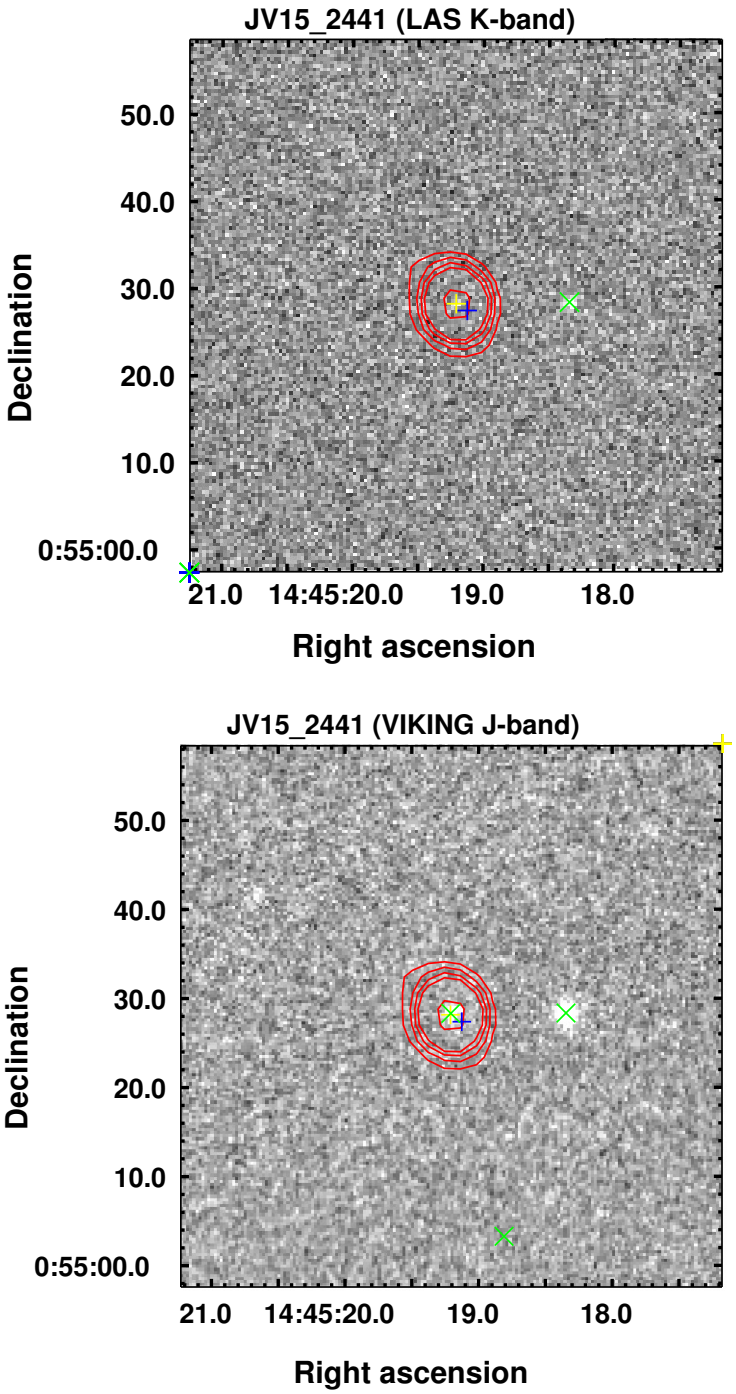

Figure 5.5: K-band LAS (top) / J-band VIKING (bottom) - radio overlays for source JV15_2441. Contours in red are from FIRST and are at $(0.5, 1, 1.5, 2, 5, 10, 20, 50)$ mJy / beam (the rms of FIRST is 0.2 mJy / beam). Formal H-ATLAS and LAS / VIKING detections are represented as blue '+' and green 'X' marks, respectively. The yellow '+' sign represents catalogued VKING position of the presumed radio source host.

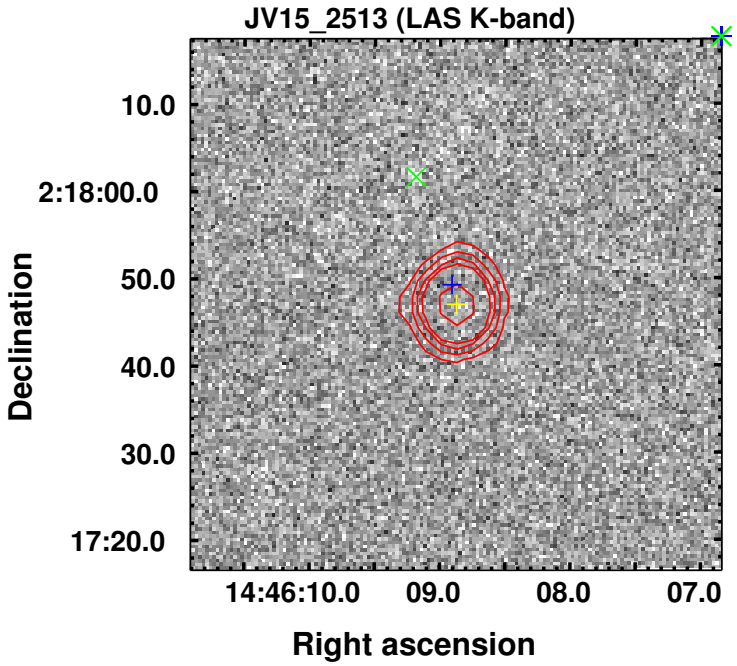

Figure 5.6: K-band LAS - radio overlay for source JV15_2513. Contours in red are from FIRST and are at $(0.5, 1, 1.5, 2, 5, 10, 20, 50)$ mJy / beam (the rms of FIRST is 0.2 mJy / beam). Formal H-ATLAS and LAS detections are represented as blue '+' and green 'X' marks, respectively. The yellow '+' sign represents catalogued FIRST position of the radio source.

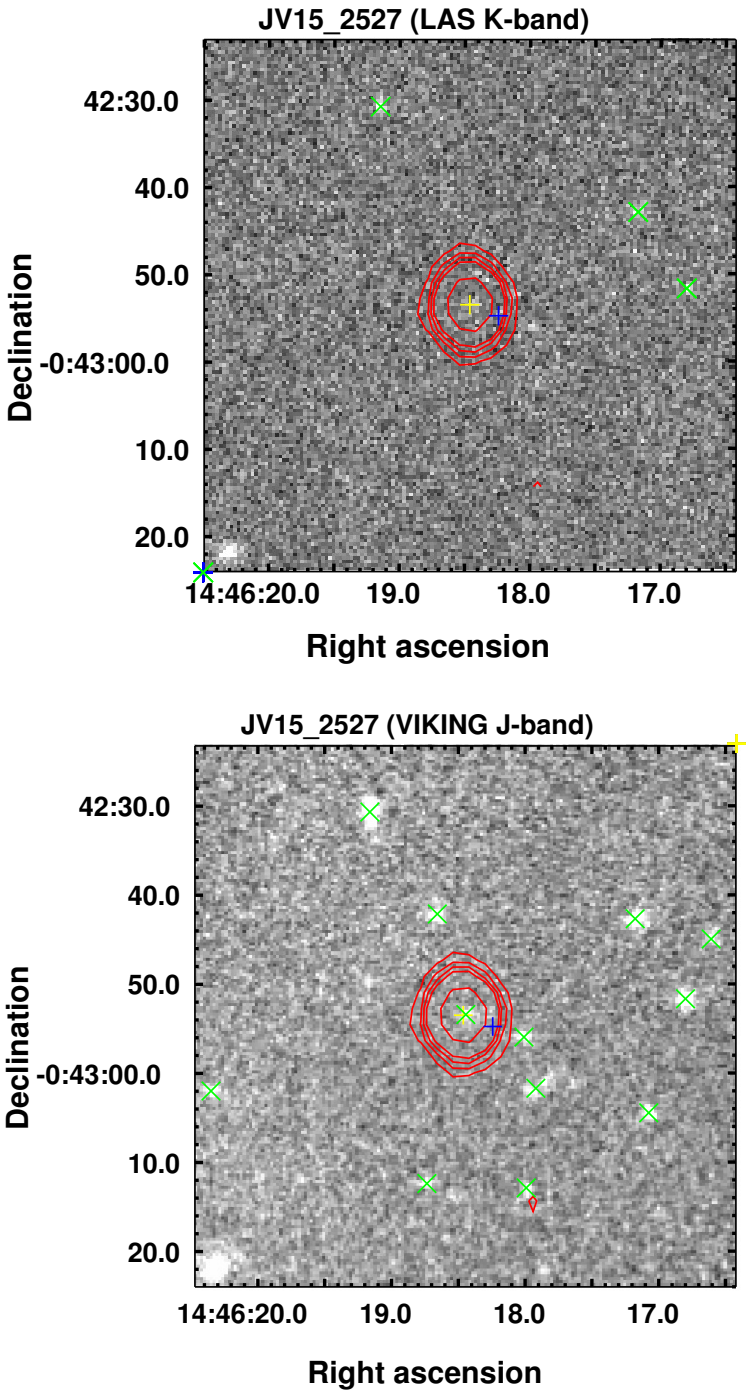

Figure 5.7: K-band LAS (top) / J-band VIKING (bottom) - radio overlays for source JV15_2527. Contours in red are from FIRST and are at $(0.5, 1, 1.5, 2, 5, 10, 20, 50)$ mJy / beam (the rms of FIRST is 0.2 mJy / beam). Formal H-ATLAS and LAS / VIKING detections are represented as blue '+' and green 'X' marks, respectively. The yellow '+' sign represents catalogued FIRST position of the radio source.

5.3 Optical spectroscopy

In the following section I report on the redshift determination of the seven radio sources. I discuss the reduction method, the redshifts and the line properties of the sources.

5.3.1 Data reduction

The 7 radio sources were observed with both arms of the ISIS instrument at the WHT in February 2011 over the course of 3 nights[1]. Long-slit spectroscopy was preformed across the entire visible band (3200-9900 Å) using gratings R158R and R300B, and the REDPLUS and EEV12 detectors respectively. The spectra were all reduced using the Image Reduction and Analysis Facility[2] (IRAF) package TWODSPEC LONGSLIT. The red frames consisted of two 15 minute exposures which were combined after being reduced separately. The blue frames consisted of a single 30 minute exposure. A single 30min exposure is needed because the sky is fainter at the blue end of the optical spectrum. Therefore, it takes longer for the CCD to become sky limited. Using a slit width of $1.5''$, we obtained spectral resolutions of ~ 3.5 Å for both arms. The slit was placed on the radio positions, without optical identification, by 'blindly' offsetting from a nearby guide star.

Multiple bias, lamp-flat, sky-flat, arc and standard-star frames were taken at the beginning and end of the night to ensure reliable calibration. Bias frames are dark exposures with 'zero' (i.e. very short) exposure time. The bias is added to the pixels in the CCD to allow noise values to remain positive and thus be recorded. Several frames for both the red and the blue arms were taken, and subsequently averaged into a 'combined' bias frame. During the data reduction, the combined bias frame was subtracted from all the calibration and source frames. Lamp-flats are images of the CCD illuminated by a white-light source. This shows how light illuminates the CCD. During the data reduction, lamp-flats were normalised and

[1] Priority and the majority of the observing time was given to other sources on an unrelated project
[2] For the official website, go to http://iraf.noao.edu/

averaged into a 'combined' lamp-flat frame. Using the combined lamp-flat, I found the coordinates of the sections of the image which are not well illuminated. In the case of ISIS data, the x and y-axis are the spatial and spectral directions, respectively. Therefore, to ensure that the wavelength calibration is not affected by sections of the frame which will contain mostly noise, the upper and lower sections of all the calibration and source frames were trimmed. Next, the RESPONSE task was run on the combined lamp-flat. This task corrects for the fact that the instrument may distribute light unevenly in the spectral direction (i.e. along the y-direction). RESPONSE corrects for this by collapsing and averaging the pixel values in the spectral direction, resulting in a single curve. The output is the reciprocal of this curve. Next, the combined sky-flat (an image of the sky at dusk or dawn), is divided by the output of RESPONSE. The output of this procedure is then passed to the task ILLUMINATION, which performs the same operation as RESPONSE, but in the orthogonal sense (e.g. the pixel values in the x-direction are collapsed and fitted to). It is important to use the sky-flat for this procedure, since the telescope should be focused at infinity. The output of illumination is subsequently multiplied by the output of RESPONSE. The new frame may be referred to as the 'super-flat', as it contains dispersion corrections for both axes. Therefore, all the remaining frames are divided by the super-flat.

For wavelength calibration, arc frames were used. These are frames illuminated by CuAr+CuNe lamps, whose emission line wavelengths are known. The IDENTIFY and REIDENTIFY tasks were used to assign wavelengths to the emission lines. Next the task FITCOORDS was run on the arc frames to find the curvature in the x and y directions (this is done manually, by fitting a polynomial to multiple emission lines). The task TRANSFORM was then used to apply the curvature corrections to all the frames. Next, the task BACKGROUND was run on all the science sources and spectro-photometric standard stars. BACKGROUND removes the sky lines which are assumed to be stable in the spatial direction; this is done by fitting multiple lines across the spatial direction and subtracting them. Next, flux calibration

was undertaken. First, the task APSUM was used on the spectro-photometric standard stars to extract the 1D spectrum. Next STANDARD, which includes calibrated photometry for that specific standard star, was executed. This task allows the user to select which regions (or bandpasses) should be used for flux calibration. The output is then used by SENSFUNC which calculates the sensitivity function for flux calibration. The actual flux calibration is performed by FLUXCALIB, and was applied to all the science sources. The 1D spectrum at the position of the radio source was extracted using APSUM in the interactive mode. In the red frame, cosmic rays were removed by flipping between frames to confirm the recored flux was indeed a cosmic ray event. Since data from the blue arm only consisted of one frame, cosmic rays were identified manually by their particular flux density profile (i.e. a bright delta-function like profile in both the x and y-directions).

5.3.2 Redshift determination

To determine redshifts, candidate lines were fitted to the peak of the brightest line in the optical spectra for each source. The trial lines which were fitted to the data were: Ly-α λ1216, N V λ1241, Si V λ1403, C IV λ1549, He II λ1640, C III] λ1909, C II] λ2323, Ne IV λ2424, Mg II] λ2799, [Ne V] λ3346, [Ne V] λ3425, [O II] λ3727, [Ne III] λ3869, [Ne III] λ3967, H-β λ4861, [O III] λ4959, [O III] λ5007 and H-α λ6562[1]. Confirmation lines were then searched for by overlaying the positions of the lines quoted above. Several of the spectra contain only one emission line. For these sources, line identification was carried out via a process of elimination. Special attention was paid to known bright-lines such as: Ly-α λ1216, C IV λ1549, Mg II] λ2799, [O II] λ3727, [O III] λ5007 and H-α. Ly-α tends to be the brightest line in the optical spectra of most galaxies (e.g. Leighly et al. 2007). Therefore, if bright lines such as C IV λ1549 or [O II] λ3727 were fitted to the single emission

[1]Forbidden lines have two square brackets e.g. [O III], while semi-forbidden lines have one on the right-hand side e.g. C II]

line and Ly-α was still between 3000-9900 Å in the observed frame, the line identification was rejected. This logic was applied to other lines which might be expected to be observed, such as [O II] $\lambda 3727$ and H-α. To further inform the redshift determination, I include, where available, VISTA VIKING photometry which may be used to calculated *rough* photometric redshifts using the $K - z$ relation. Each source is discussed in detail below. The prefix 'JV09' or 'JV15' indicates which H-ATLAS phase 1 field the source belongs to.

JV09_0386: The area around source JV09_0386 is covered by VISTA VIKING, which finds a K-band source $0.36''$ away from the FIRST position with $K_s = 19.09 \pm 0.19$ (see Fig. 5.1). This is probably the host of the radio emission. The FIR source detected in the H-ATLAS is $2.8''$ from the radio source. The WHT spectrum shows very faint red continuum and an emission line which was identified as Ly-α, implying a redshift of 2.372 (see Fig. 5.8). A line ID of C IV $\lambda 1549$ is rejected on the basis that Lyα should be detected in the frame. A line ID of [O II] $\lambda 3727$ is rejected on the basis that H-α should be detected in the frame. The $K - z$ relation estimates a redshift of 2.45 ± 0.69, in line with the spectroscopic estimate (c.f. the error on the redshift estimate is from the dispersion in the $K - z$ relation calculated by Jarvis et al. 2001).

JV09_0627: The area around source JV09_0627 is covered by VISTA VIKING, which finds a K-band source $0.14''$ away from the FIRST position with $K_s = 18.58 \pm 0.11$ (see Fig. 5.2). The $K - z$ relation estimates a redshift of 1.87 ± 0.5. The FIR source detected in the H-ATLAS is $1.6''$ from the radio source. Only one definite emission line at 7911 Å is detected from this object (see Fig. 5.8). A line ID of Ly-α is rejected on the basis that that the redshift would be 5.507. Although not impossible, such a high redshift is considered improbable given the disagreement with the redshift estimate from the $K - z$ relation. A line identification of C IV $\lambda 1549$ and Mg II] $\lambda 2799$ are rejected on the basis that Lyα should still

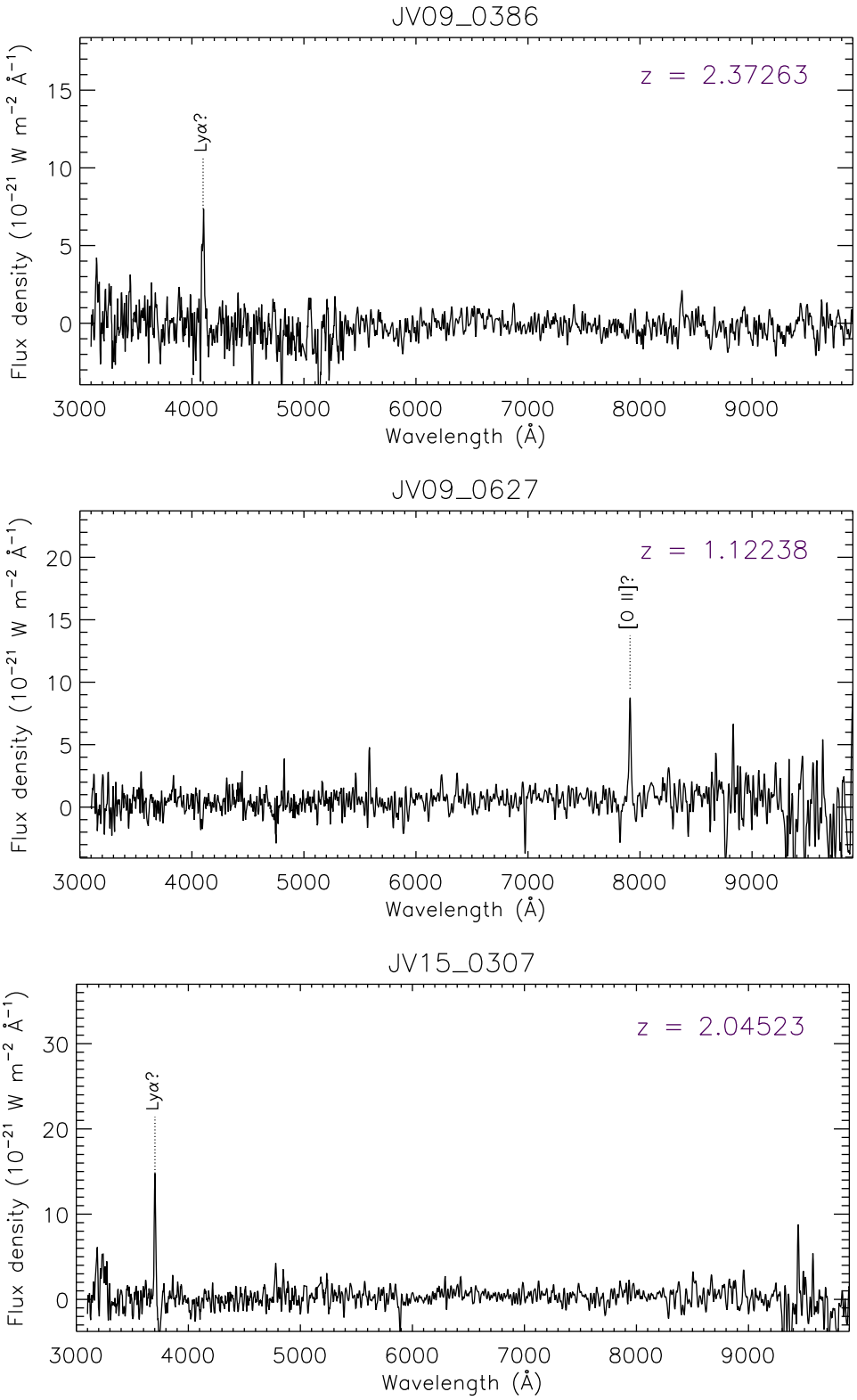

Figure 5.8: Optical spectra from the WHT for sources JV09_386, JV09_627 and JV15_307. The wavelength is in the observed frame.

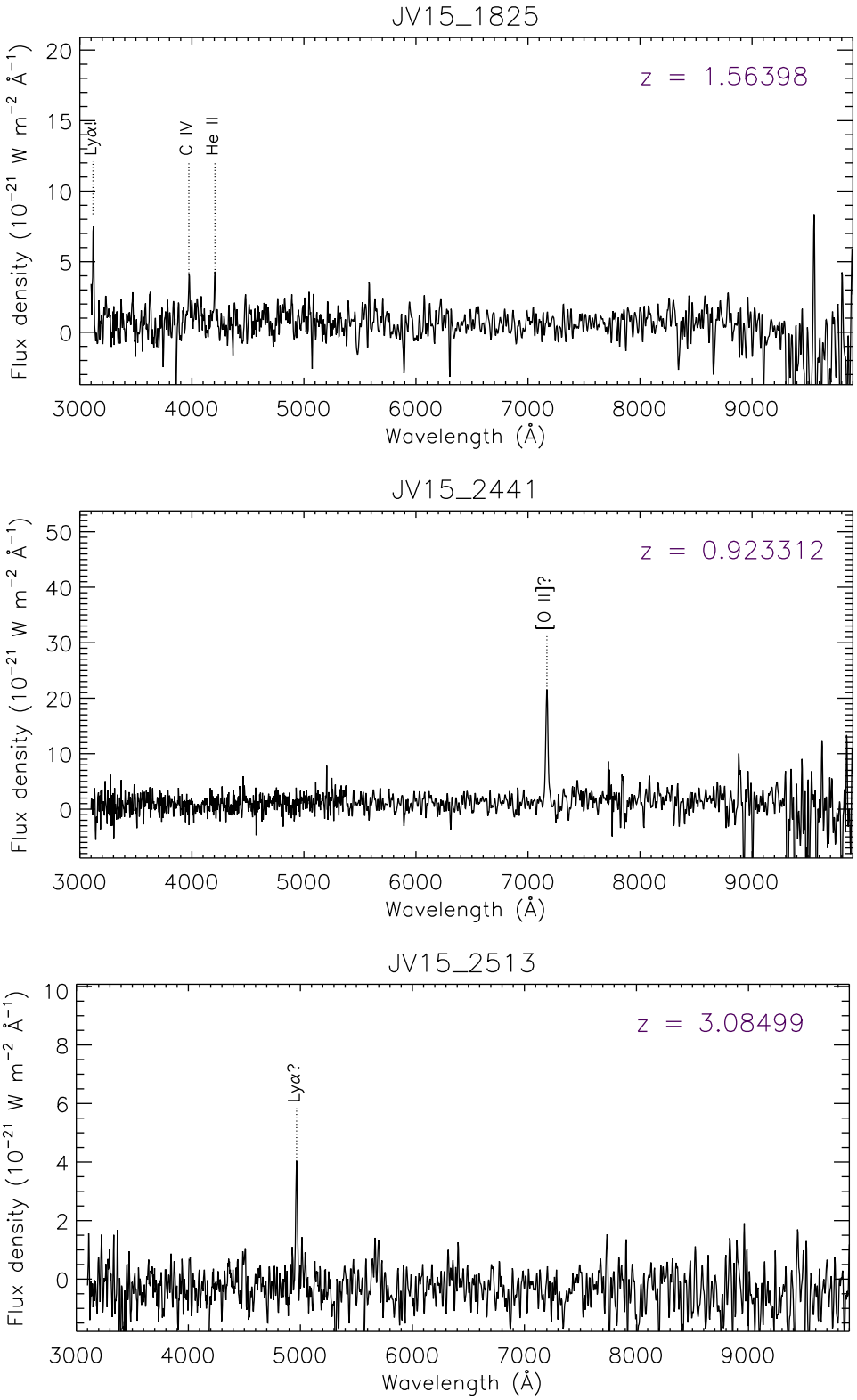

Figure 5.9: Optical spectra from the WHT for sources JV15_1825, JV15_2441 and JV15_2513. The wavelength is in the observed frame.

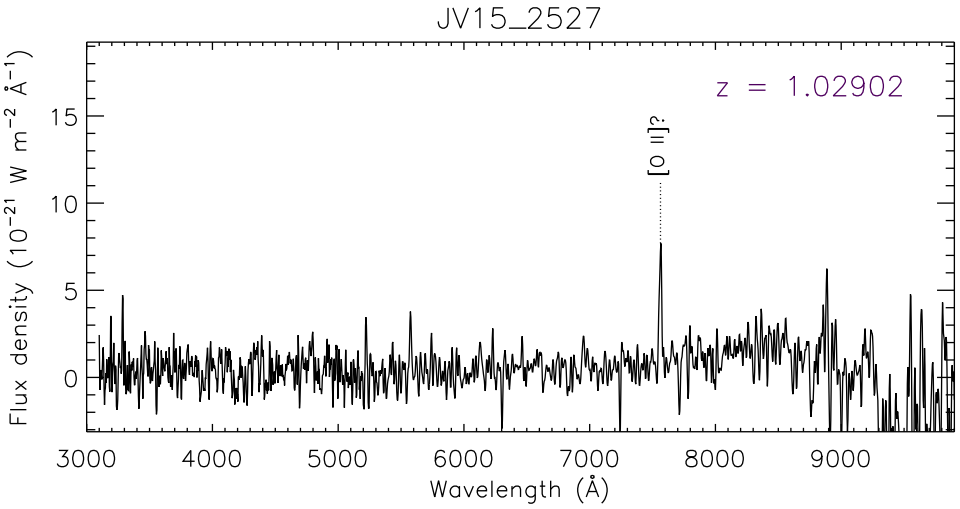

Figure 5.10: Optical spectra from the WHT for source JV15_2527. The wavelength is in the observed frame.

be detected in the frame. A line identification of H-α is rejected on the basis that H-β should also be detected. This leaves [O II] $\lambda3727$ as the most probably ID for the emission line, although no confirmation lines are found. Therefore, a redshift of $z = 1.123$ is calculated.

JV15_0307: The radio source in Fig. 5.3 is $3.67''$ away from the source detected in the H-ATLAS. VIKING J-band data were available, but no K-band data. Only one definite emission line is detected from this object along with continuum in the red frame (see Fig. 5.8). Identification of this single line with Ly-α implies a redshift of 2.044. Line identifications of C IV $\lambda1549$ and C III] $\lambda1909$ are rejected on the basis that [O II] $\lambda3727$ should also be detected. A line identification of [O II] $\lambda3727$ leads to a negative redshift.

JV15_1825: The radio source in Fig. 5.4 is $1.57''$ away from the source detected in the H-ATLAS. VIKING J-band data were available, but no K-band data. A NIR source, presumed to be the host of the radio emission, is detected $0.12''$ away from the predicted position. Two weak but definite lines are seen clearly in the 1D spectrum yielding $z = 1.565$ (C IV $\lambda1549$

and He II $\lambda 1640$); the Ly-α emission is too close to the atmospheric cut-off to be securely detected (see Fig. 5.9).

JV15_2441: The radio source in Fig. 5.5 is $1.49''$ away from the source detected in the H-ATLAS. VIKING J-band data were available, but no K-band data. A NIR source, presumed to be the host of the radio emission, is $0.16''$ away from the predicted position. Only one definite emission line at 7169 Å is detected from this object (see Fig. 5.9). A line ID of Ly-α is rejected on the basis that that the redshift would be 4.896. Although not impossible, such a high redshift would imply an unreasonably large FIR luminosity for an H-ATLAS detected object, and is thus considered improbable. A line identification of C IV $\lambda 1549$ and C III] $\lambda 1909$ are rejected on the basis that Lyα should be detected in the 1D spectra. This leaves [O II] $\lambda 3727$ as the most probable ID for the emission line, although no confirmation lines are found. Therefore, a redshift of $z = 0.923$ is calculated.

JV15_2513: The radio source in Fig. 5.6 is $2.31''$ away from the source detected in the H-ATLAS. No VIKING data were available. A single emission line is seen in both of two blue exposures taken on nights two and three, probably Ly-α at $z = 3.084$ (see Fig. 5.9). No continuum is detected in either frame. A line identification of C IV $\lambda 1549$ and C III] $\lambda 1909$ are rejected on the basis that Ly-α should still be detected in the frame. A line identification of [O II] $\lambda 3727$ is rejected on the basis that H-α should be detected in the frame.

JV15_2527: The radio source in Fig. 5.7 is $3.54''$ away from the source detected in the H-ATLAS. VIKING J-band data were available, but no K-band data. A NIR source, presumed to be the host of the radio emission, is $0.29''$ away from predicted position. A single emission line and continuum in the red frame are detected (see Fig. 5.10). A line identification of Ly-α is rejected on the basis that the implied redshift is too high ($z = 5.221$). Although not

Object	Line	λ_{rest} (Å)	λ_{meas} (Å)	Continuum (10^{-22} W m^{-2} Å^{-1})	Flux (10^{-19} W m^{-2})
JV09_0386	Ly-α?	1216	4100	< 10.0	1.7
JV09_0627	[O II]?	3727	7911	6.0	1.8
JV15_0307	Ly-α?	1216	3702	7.7	2.1
JV15_1825	Ly-α!	1216	3121		
	C IV	1549	3976	14.0	0.4
	He II	1640	4206	13.0	0.4
JV15_2441	[O II]?	3727	7169	16.0	5.0
JV15_2513	Ly-α?	1216	4966	< 10.0	1.7
JV15_2527	[O II]?	3727	7563	< 10.0	0.70

Table 5.2: Measurements obtained from the WHT spectra of the radio sources. The '?' denotes an uncertain line identification and the '!' denotes a feature which is plausibly spurious.

impossible, such a high redshift would imply an unreasonably large FIR luminosity for an H-ATLAS detected object, and is thus considered improbable. In addition, the space density of radio-loud sources is very low at $z \sim 5$ (see Rigby et al. 2011a). A line identification of C IV $\lambda1549$ and Mg II] $\lambda2799$ are rejected on the basis that Ly-α should still be detected in the frame. This leaves [O II] $\lambda3727$ as the most probable ID for the emission line, although no supporting emission lines are found. Therefore, a redshift of $z = 1.029$ is calculated.

The redshifts of the seven sources are between 0.9 and 3.1. Six of the seven sources only have a single emission line. In most cases, this was identified as Ly-α or [O II] $\lambda3727$. All the lines are narrow, suggesting that these sources are obscured narrow line galaxies. The (likely) [O II] $\lambda3727$ emission detected in sources JV15_2441 and JV15_2527 may plausibly be from star-formation, and not AGN activity. Further, dust temperature and luminosity estimates for the line identifications implying high redshifts are unphysical, strengthening the case for the above line IDs. Since most of the radio structures are compact, the AGN are also likely to be relatively young.

5.3.3 VIKING - ATLAS matches

It is clear that some of the sources targeted are revealed to be embedded in more crowded fields when looked at using deeper VISTA VIKING data. On the surface, this might make it more difficult to unambiguously match the observed FIR emission to the radio source in question. However, the NIR bands probe old stellar light, which is not expected to correlate well with FIR emission. This is not the case for powerful radio-AGN, particularly at high redshifts, as they are often associated with high FIR / sub-mm luminosities (Archibald et al. 2001; Reuland et al. 2004). Therefore on average, one would expect the hosts of radio sources to be the origin of any H-ATLAS emission even if one or more K-band counterparts were found nearby.

In order to quantify this expectation, I use the results of Fleuren et al. [2012] who matched K-band VISTA VIKING sources to H-ATLAS sources in the GAMA 9^{hr} field. Their matching process involved accepting any K-band source which fell within a $10''$ radius of any H-ATLAS source as a 'candidate match' (there were 35,800 such sources). Next, they calculated the likelihood ratio of every 'candidate match' using the likelihood analysis developed by Smith et al. [2011]. If a source had a likelihood ratio of $R > 0.8$, it was considered a 'reliable' counterpart. They found that of the 35,800 candidate matches, 11,294 (or 31.5%) were 'reliable' matches. This implies that if any K-band VIKING source falls within $10''$ of an H-ATLAS source, it only has a 31.5% chance of being a 'reliable' match (i.e. the host of the FIR emission). This is compared to the 94.4% chance assigned to the radio sources *in this* sample (see Section 5.2), although this is not strictly a fair comparison, as my sources were matched with a $4''$ matching criterion instead of $10''$. However, it must be noted that Fleuren et al. [2012] find that the fraction of reliable matches falls with fainter K-band magnitudes, partially offsetting this bias. Using this logic, we determine that the host of the radio source is *far* more likely to be the source of the FIR emission than any other counterparts detected within $10''$ of the FIR position.

5.4 The FIR data

One of the unique aspects of this sample is the FIR data provided by *Herschel*. As discussed in Section 1, the H-ATLAS provides data at 100, 160, 250, 350 and 500 μm. In combination with redshifts, these photometric data allow one to constrain the isothermal dust temperature (T). The dust temperature is a useful parameter, as it allows one to infer the source of the interstellar radiation field heating the ISM. In order to calculate the dust temperature, we follow the method established in Chapter 4. In other words, we fit to a modified isothermal-blackbody of the following form,

$$f_v \propto \frac{\nu^{3+\beta}}{e^{\frac{h\nu}{kT}} - 1}, \tag{5.1}$$

where T represents the isothermal temperature of the source in question, ν is the frequency, k is the Boltzmann constant, h is the Planck constant and β is the beta parameter. A β value of 2.05 is assumed, as this was the best-fitting β value for the radio sample in Chapter 4. The errors are calculated by finding the values of the 16^{th} and 84^{th} percentile limits, after converting the χ^2 distribution to a probability distribution function (PDF) assuming $P(\beta) \propto \exp^{(\frac{-\chi^2}{2})}$. The fluxes and errors come from the 5-σ H-ATLAS catalogue. A calibration error of 10% and 7% is added to the PACS and SPIRE data as recommended by the documentation. PDFs as a function of temperature, and observed-frame SEDs are shown in Figs. 5.11 to 5.13 for all the sources. The results are also summarised in Table 5.3.

The FIR luminosity allows one to estimate another important quantity, the SFR. The SFR may be calculated using the relation developed in Hardcastle et al. [2013], defined as,

$$\log_{10}\left(L_{250} \,/\, \mathrm{W\,Hz^{-1}}\right) = 23.64 + 0.96\log_{10}(\mathrm{SFR} \,/\, \mathrm{M_{\odot}yr^{-1}}), \tag{5.2}$$

Source	S_{100} (mJy)	S_{160} (mJy)	S_{250} (mJy)	S_{350} (mJy)	S_{500} (mJy)	Temperature (K)	Reduced χ^2
JV09_386	2.68±46.75	-57.69±66.81	45.8±6.9	51.1±8.0	45.1±8.8	$28.5^{+3.3}_{-2.0}$	0.54
JV09_627	-28.42±31.16	—	33.5±6.6	20.1±7.2	16.6±8.9	$25.7^{+8.9}_{-3.4}$	0.26
JV15_307	113.14±52.38	-50.07± 70.11	38.5±6.8	47.1±8.1	22.9±8.9	$28.3^{+5.0}_{-2.2}$	0.43
JV15_1825	27.35±47.10	36.86±62.65	73.4±6.4	70.0±7.7	42.0±8.4	$25.7^{+2.8}_{-1.5}$	0.01
JV15_2441	57.91±37.45	119.00±62.85	38.4±6.9	17.8±8.0	8.6±8.8	$40.5^{+5.5}_{-7.8}$	0.92
JV15_2513	36.87±43.23	30.66±66.01	95.8±6.9	103.1±8.1	65.2±9.0	$38.3^{+2.8}_{-1.9}$	0.01
JV15_2527	15.90±47.50	115.38± 68.32	33.3±6.6	22.3±7.9	1.2±8.7	$36.3^{+8.6}_{-8.1}$	0.42

Table 5.3: FIR fluxes and fitted dust temperatures for the 7 radio galaxies.

where, L_{250} is the luminosity at 250 μm (here, the fitted dust temperature provides a model for the calculation of the K-correction). This relation was calibrated using radio sources with $T > 25$ K, therefore, it should only be used if the dust temperature of any given source is above this. In the cases where it is not, it may be used to calculate an upper-limit on the SFR. The errors on the SFRs quoted in this chapter are calculated by recalculating L_{250} (and therefore the SFR), using the upper and lower temperature bounds (i.e. $T \pm \delta T$) for every source. This ensures that the non-Gaussian distributions of many of the temperature PDFs shown in Figs. 5.11 to 5.13 are carried though to the SFR errors.

It was also possible to calculate radio flux-density contribution from star formation using the far-infrared radio-correlation (FIRC), defined as,

$$q_{250} = \log_{10}\left[\frac{L_{250}}{L_{1.4\,\mathrm{GHz(SF)}}}\right] \tag{5.3}$$

where $q_{250} = 1.78 \pm 0.04$ (Jarvis et al. 2010) and $L_{1.4\,\mathrm{GHz(SF)}}$ is the radio luminosity from star-formation. However, to do this one must assume that all the FIR emission is the result of star formation. The validity of this assumption increases as the fitted isothermal dust-temperature goes up. A wider discussion of the caveats of such an assumption is provided in section 3.4.7. The results of the calculations for the rest-frame luminosities at 250 μm, the inferred radio luminosities and flux densities from star formation is provided in Table 5.4.

Source	$\log_{10}(L_{250})$ $\log_{10}(\mathrm{W\,Hz^{-1}})$	$\log_{10}(L^{SF}_{1.4\mathrm{GHz}})$ $\log_{10}(\mathrm{W\,Hz^{-1}})$	$\mathrm{S}^{SF}_{1.4\mathrm{GHz}}$ (μJy)	SF Fraction (%)	SFR $\mathrm{M_\odot\,/\,yr^{-1}}$
JV09_386	26.8 ± 0.2	25.0	220.7	10.22	1761^{+1145}_{-694}
JV09_627	25.8 ± 0.4	24.1	297.0	4.87	194^{+302}_{-118}
JV15_307	26.5 ± 0.3	24.7	374.7	1.93	964^{+860}_{-455}
JV15_1825	26.6 ± 0.2	24.8	515.8	0.32	1123^{+564}_{-376}
JV15_2441	25.5 ± 0.2	23.7	133.8	1.60	78^{+61}_{-34}
JV15_2513	26.9 ± 0.1	25.2	221.4	3.30	2731^{+1007}_{-736}
JV15_2527	25.5 ± 0.3	23.8	130.0	1.94	94^{+120}_{-53}

Table 5.4: The luminosity at 250 μm is listed, along with the inferred radio luminosity and flux density from SF, the fraction of the radio emission due to SF and the SFR. The inferred radio fluxes and luminosities are from *Herschel* data.

Also included in Table 5.4 is the fraction of the radio emission due to star formation and the SFR itself. Below, the properties of each source are discussed.

JV09_386: The temperature PDF and SED of this source are shown in Fig. 5.11. The 100 μm band has a rest-frame wavelength below 45 μm, and as such, is excluded from the temperature and SED fitting due to the possibility of AGN contamination. The fitted isothermal dust temperature is $28.5^{+3.3}_{-2.0}$ K with a reduced χ^2 value of 0.54, implying that the dust temperature is well constrained. Using the FIRC, the flux-density contribution at 1.4-GHz due to star-formation is found to be 220.7 μJy. This implies that 10.22% of the radio emission of this source is star-formation related. The star-formation rate is estimated to be 1761^{+1145}_{-694} $\mathrm{M_\odot\ yr^{-1}}$.

JV09_627: The temperature PDF and SED of this source are shown in Fig. 5.11. The 160 μm band is excluded from the temperature and SED fitting because of artefacts in the map at this position. The fitted isothermal dust temperature is $25.7^{+8.9}_{-3.4}$ K with a reduced χ^2 value of 0.26. The flux-density contribution at 1.4-GHz due to star-formation is 297.0 μJy. This implies that 4.87% of the radio emission of this source is star-formation related. The

star-formation rate is estimated to be $194^{+302}_{-188}\,\mathrm{M}_{\odot}\,\mathrm{yr}^{-1}$.

JV15_0307: The temperature PDF and SED of this source are shown in Fig. 5.11. The 100 μm band has a rest-frame wavelength below 45 μm; therefore, it is excluded from the temperature and SED fitting due to the possibility of AGN contamination. The fitted isothermal dust temperature is $28.3^{+5.0}_{-2.2}$ K with a reduced χ^2 value of 0.43, implying that the dust temperature is well constrained. The flux-density contribution at 1.4-GHz due to star formation is 374.7 μJy. This implies that 1.93% of the radio emission of this source is star-formation related. The star-formation rate is estimated to be $964^{+860}_{-455}\,\mathrm{M}_{\odot}\,\mathrm{yr}^{-1}$.

JV15_1825: The temperature PDF and SED of this source are shown in Fig. 5.12. The 100 μm band has a rest-frame wavelength below 45 μm and is therefore omitted from the temperature and SED fitting. The fitted isothermal dust temperature is $25.7^{+2.8}_{-1.5}$ K with a very low reduced χ^2 value of 0.01. The flux-density contribution at 1.4-GHz due to star formation is 515.8 μJy. This implies the 0.32% of the radio emission of this source is star-formation related. The star-formation rate is estimated to be $1123^{+564}_{-376}\,\mathrm{M}_{\odot}\,\mathrm{yr}^{-1}$.

JV15_2441: The temperature PDF and SED of this source are shown in Fig. 5.12. All the PACS and SPIRE bands are used in the temperature and SED fitting. The fitted isothermal dust temperature is $40.5^{+5.5}_{-7.8}$ K with a reduced χ^2 value of 0.92. The flux-density contribution at 1.4-GHz due to star-formation is 133.8 μJy. This implies that 1.60% of the radio emission of this source is star formation related. The star-formation rate is estimated to be $78^{+61}_{-34}\,\mathrm{M}_{\odot}\,\mathrm{yr}^{-1}$.

JV15_2513: The temperature PDF and SED of this source are shown in Fig. 5.12. Both PACS bands have rest-frame wavelengths below 45 μm and are therefore excluded from the

temperature and SED fitting due to the possibility of AGN contamination. S13 showed that in the absence of PACS data, the fitted temperature is liable to be biased towards colder temperatures. Nevertheless, the fitted isothermal dust temperature is $38.3^{+2.8}_{-1.9}$ K with a reduced χ^2 value of 0.01, implying that the dust temperature is well constrained. The flux-density contribution at 1.4-GHz due to star formation is 221.4 μJy. This implies that 3.30% of the radio emission of this source is star-formation related. The star-formation rate is estimated to be 2731^{+1007}_{-736} $M_\odot$ yr^{-1}.

JV15_2527: The temperature PDF and SED of this source are shown in Fig. 5.13. All the PACS and SPIRE bands are used in the temperature and SED fitting. The fitted isothermal dust temperature is $36.3^{+8.6}_{-8.1}$ K with a reduced χ^2 value of 0.42. Inspection of the FIR SED suggests this is mainly due to the high flux-density detected at 160.0 μm. The flux-density contribution at 1.4-GHz due to star-formation is 130.0 μJy. This implies that 1.94% of the radio emission of this source is star formation related. The star-formation rate is estimated to be 94^{+120}_{-53} $M_\odot$ yr^{-1}.

The dust temperatures of the radio sources vary from $\sim 25 - 40$ K. This means that one may use the relation from Hardcastle et al. [2013] to calculate SFRs for all the sources. Nevertheless, the assumption that all the FIR emission is the result of star-formation is a caveat.

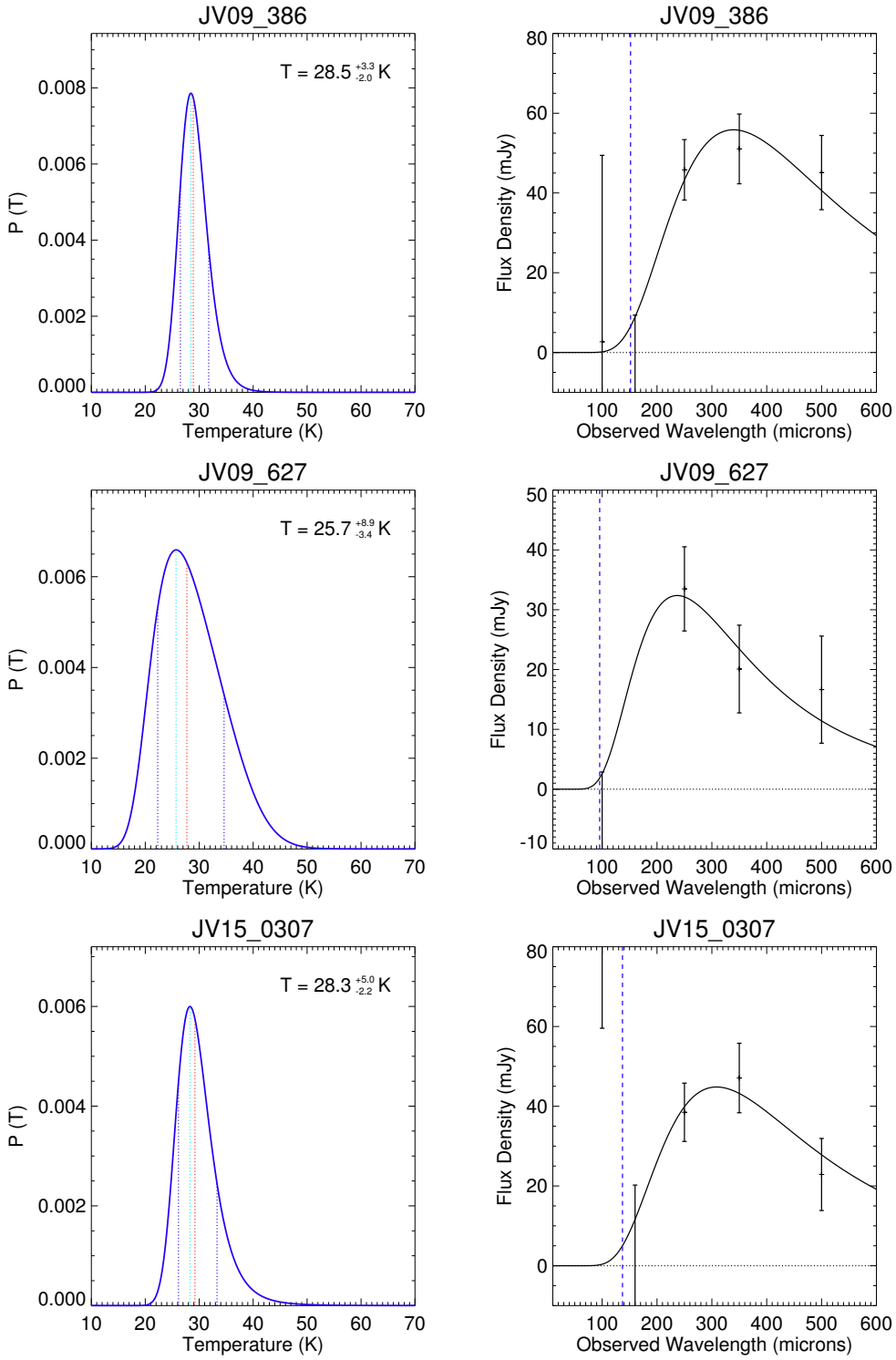

Figure 5.11: Left: PDFs of the dust temperature. The dashed cyan and red lines represent the best-fitting and median temperatures, with the dashed dark blue lines representing the 16^{th} and 84^{th} percentile limits. Right: Observed-frame SEDs with the PACS and SPIRE data overlaid. Photometry below rest-frame 45 μm (blue dashed-line) is not included in the temperature and SED fitting due to the possibility of AGN contamination.

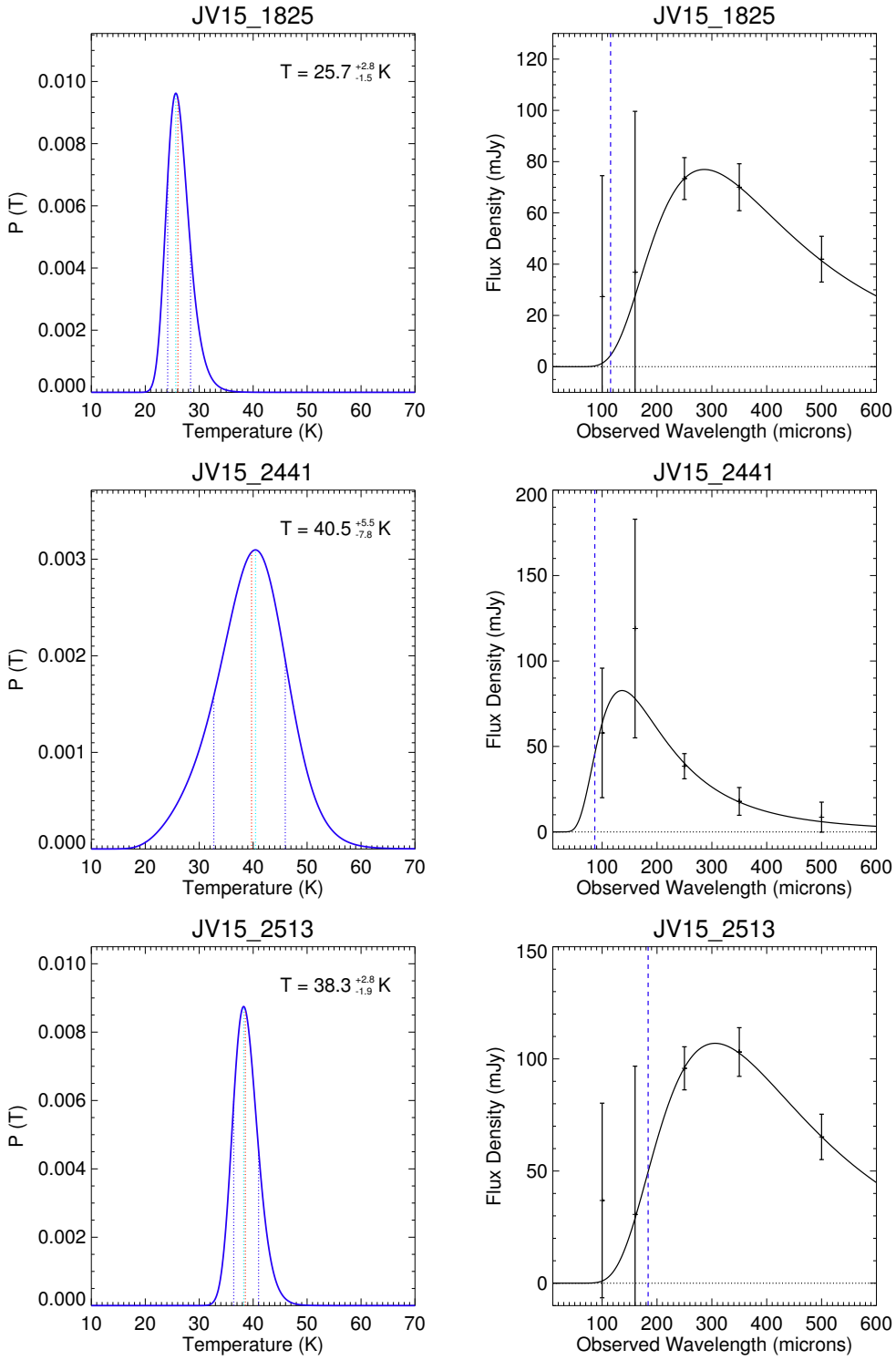

Figure 5.12: Left: PDFs of the dust temperature. Colour code is identical to Fig. 5.11. Right: Observed-frame SEDs with the PACS and SPIRE data overlaid. Photometry below rest-frame 45 μm (blue dashed-line) is not included in the temperature and SED fitting due to the possibility of AGN contamination.

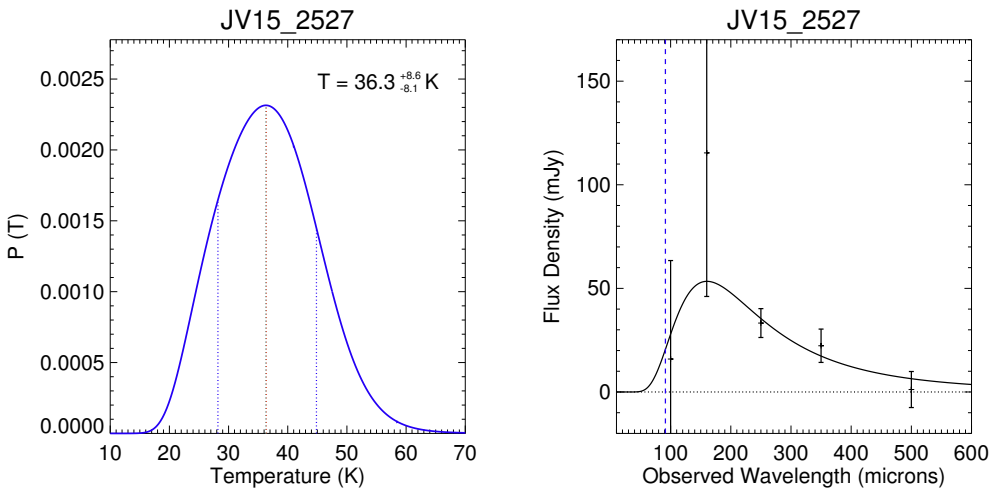

Figure 5.13: Left: PDFs of the dust temperature. Colour code is identical to Fig. 5.11. Right: Observed-frame SEDs with the PACS and SPIRE data overlaid. Photometry below rest-frame 45 μm (blue dashed-line) is not included in the temperature and SED fitting due to the possibility of AGN contamination.

5.5 Discussion

The primary aim of this chapter is to show that it is possible to use a combination of NIR and radio data to create a reliable sample of high-redshift objects with 5-sigma detections at 250 μm using the *Herschel*-ATLAS. The redshifts acquired for the 7 radio sources presented here using WHT-ISIS spectroscopy are between $0.9 < z < 3.1$, and thus clearly demonstrate that the sample selection method used here is valid for finding rare, high-z sources. Star-formation rates, calculated using photometry from the *Herschel*-ATLAS, vary significantly (i.e. from 78 - 2700 $M_{\odot}$ yr^{-1}; see Table. 5.4). The large errors attached to these estimates are primarily due to the size of the dust temperature errors. Nevertheless, the estimated SFRs are high in comparison to quiescent galaxies. Other techniques designed to find high-z objects such as FIR / submm gravitational lenses (i.e. Negrello et al. 2010) tend to more consistently identify objects with higher average SFRs, but further analysis is always impeded by the need for a good lens model. Another method for identifying high-z objects in

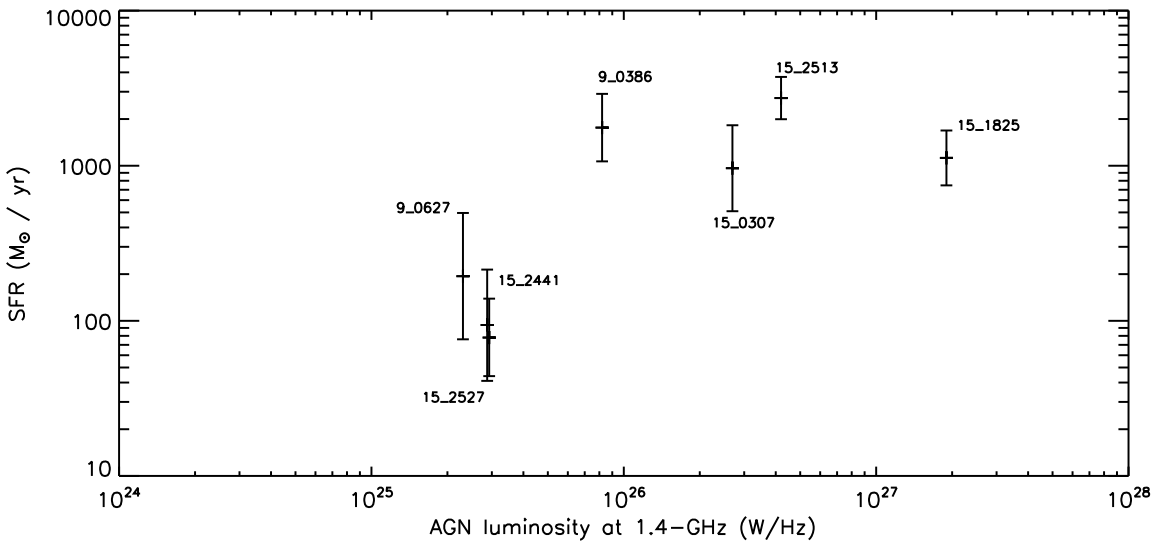

Figure 5.14: SFR versus 1.4-GHz radio luminosity from the AGN.

the H-ATLAS involves using colour-colour diagrams of the main FIR channels from SPIRE (i.e. 250, 350 and 500 μm). Emission from dust typically peaks around 100 μm, so if the colours of individual sources suggest a peak above 350 μm or more, then the source may be at high redshift. However, such sources do not necessarily host radio-AGN. Thus, in order to maximise the legacy of the H-ATLAS data-set, it will be worth identifying as may high-z objects as possible using the methodology outline in this chapter.

Another important goal of this chapter is to determine whether there is any evidence for radio-jet feedback in the sample presented here. An initial inspection of Fig. 5.14, where the star-formation rate is plotted against AGN's radio luminosity (the total radio luminosity minus the radio luminosity from star formation) suggests that star-formation increases with radio luminosity. This might be interpreted as evidence for positive feedback. However, this may simply be due to higher redshift objects having higher SFRs and radio luminosities. Indeed, 3 of the 4 sources with the highest SFRs and radio luminosities have redshifts above

the median of the sample. In addition, it would be preferable to calculate the specific SFR rather than just the SFR, since the former takes mass biases into account. Thus, the distribution observed in Fig. 5.14 cannot be seen as evidence for positive feedback. Nonetheless, it does point the way to future studies which may be in a better position to tackle the question of radio-jet induced star-formation.

As was briefly alluded to in the previous two chapters of this thesis, it is also questionable whether the radio luminosity from AGN activity is the most appropriate variable to use to investigate jet-induced feedback. This is because the radio luminosity is often dominated by core components, which are restricted to pc scales and therefore cannot directly affect the ISM. Radio-jet feedback, be it positive or negative, is thought to be the result of radio-lobe interactions with the ISM. Therefore, the lobe component of the total radio luminosity seems like the most appropriate variable to be used in studies which attempt to demonstrate direct radio feedback. To this end, the addition of high-resolution radio images (from telescopes such as the European VLBI Network and the Multi-Element Radio Linked Interferometer Network), which can isolate and measure the core and lobe components of the radio emission, will be invaluable to determine the existence, frequency and nature of direct radio-jet induced star-formation. I suggest that confirmation of positive feedback requires that both a positive relation is found between the specific SFR and the lobe luminosity, and that no relation is found between the specific SFR and the core luminosity. This will ensure that any relation which is discovered is not simply the result of biases in the sample.

The contribution to the total radio luminosity from star formation is below 5% for all sources except JV09_0386 where the contribution is $\sim$10%. JV09_0386 is the faintest radio source with a FIRST flux density of only 2.16 mJy. What will be of great interest to future studies of this kind is the flux density threshold at which fractional contribution from star formation reaches 30-50% of the radio emission. At these levels, estimating the star-

formation contribution to the total radio luminosity becomes necessary if a correct estimate of the power of the AGN-jet power is required. The methods and techniques outlined above may help us answer such questions.

A further point of interest is why 6 of the 7 radio sources presented here are compact (as seen by FIRST)? This may be due to the high detectability threshold imposed by the FIR data; assuming these sources are undergoing major merger events as described in Tadhunter et al. [2011] (not an unreasonable assumption given the redshift and the SFRs which are observed), it may be the case that these sources are detectable in the FIR only during the most intense star-formation peak after AGN triggering. Estimates for how long high-z, star-bursting radio-loud AGN are detectable in the *Herschel*-ATLAS are difficult to calculate without assuming an evolutionary history, however, given the high SFRs and the rarity of the sources, it does not seem plausible that such a state could be maintained for more than a small fraction of the canonical lifetime of a radio source ($\sim 10^8$ yrs), perhaps partially explaining why the sample is mostly made up of compact sources.

5.6 Conclusions

Seven $K > 18$ radio-loud AGN in the *Herschel*-ATLAS phase 1 fields, have been observed using the ISIS instrument at the WHT. The optical spectra reveal these sources to be between $0.9 < z < 3.1$. In combination with redshifts, the FIR / submm photometry from H-ATLAS enabled the dust temperature of all the sources to be estimated. The dust temperature was found to vary between 25-40 K. Using the L_{250}-SFR equation developed by Hardcastle et al. [2013] for radio galaxies, I estimated the SFRs of the sources; these range from $\sim$50 - 3000 $M_\odot$ / yr.

A method for identifying reliable high-z, star-bursting radio sources in the H-ATLAS was described. Such a sample is ideally suited to further studies of direct radio AGN feedback. A method for determining whether radio-jet induced star-formation exists in the radio galaxy population as a whole has been presented. The confirmation of positive feedback requires that both a positive relation is found between the the specific SFR and the lobe luminosity, and that no relation is found between the specific SFR and the core luminosity. This will ensure that any relation which is discovered is not simply the result of biases in the sample.

Chapter 6

Conclusions

6.1 Summary of the main results

A summary of the main results from this thesis are detailed below followed by a discussion of their implications.

6.1.1 Chapter 3

A sample of 1599 radio sources was selected, and the FIR properties and dust temperatures of these sources were studied using stacking techniques. The main results are:

1. No relation is found between the rest-frame luminosity at 250 μm divided by the K-band luminosity (i.e. the specific L_{250}), and the 1.4-GHz radio luminosity in the sample of radio-detected galaxies presented in Chapter 3.

2. The rest-frame luminosity at 250 μm of radio-detected and non-radio-detected galaxies rises with increasing redshift.

3. Compact radio sources (< 30 kpc) are associated with higher 250 μm luminosities than their more extended (> 30 kpc) counterparts.

4. For matched samples in L_K and g′- r′, sub-1.5 L_K^* radio-detected galaxies have 0.89±0.18 times the 250 μm luminosity of the comparison sample, with fitted temperatures of 20.5±0.5 K and 19.0±0.2 K, respectively.

5. For matched samples in L_K and g′- r′, super-1.5 L_K^* radio-detected galaxies have 0.49±0.12 times the 250 μm luminosity of the comparison sample, with fitted temperatures of 16.2±0.5 K and 21.2±0.2 K, respectively.

6. No relation between spectral index and the luminosity at 250 μm is found for the subset of 1.4-GHz radio sources with detections at 330 MHz.

6.1.2 Chapter 4

Using a well-selected sample of 1528 radio sources, the dust temperatures of radio galaxies was studied in great detail. The main results are:

1. The best-fitting β parameter, calculated by marginalising over the temperature and normalisation of all the radio galaxies in the sample, is $\beta = 2.05 \pm 0.07$. Using this β value, the best-fitting temperature is calculated, and is found to be $T = 24.84 \pm 0.20$ K.

2. The dust temperatures of radio sources increases with redshift, and are consistently higher than the temperatures of the H-ATLAS population presented in S13. This implies that radio jets may be heating the ISM through AGN feedback.

3. The dust temperatures of the radio galaxies shows little to no relation with the K-band luminosity. This implies that stellar mass is relatively unimportant in determining the dust temperature of radio galaxies.

4. The dust temperatures of radio galaxies shows a strong negative dependence with the projected radio size. This suggests that while the radio jet is inside the ISM, it is mechanically heating it. This heating may result in increased SFRs for $\sim 10 - 20$ Myr.

5. The dust temperature of radio galaxies is investigated as a function of 1.4-GHz radio luminosity. Since the radio luminosity is expected to be related to the kinetic jet power, the sample is first sub-divided into compact and extended radio galaxies. I find that the increase in temperature as a function of redshift for compact and extended radio galaxies are statistically indistinguishable.

6.1.3 Chapter 5

A methodology for reliably identifying high-z, star-bursting radio-loud AGN was presented.

1. The optical spectra reveal these sources to be between $0.9 < z < 3.1$. The dust temperature was found to vary between 25-40 K and the the SFR between $\sim$50 - 3000 $M_{\odot}$ / yr.

2. Although a weak positive relation was found between the SFR and the radio-AGN luminosity, sample biases and other factors (e.g. stella mass) mean that it is difficult to consider this as evidence for positive feedback.

6.2 Implications

I find that the FIR luminosities of radio galaxies increases with redshift, in agreement with previous results (Archibald et al. 2001; Reuland et al. 2004). However, the FIR luminosities of radio galaxies tend to be lower than that of 'normal' galaxies (i.e. non-radio-detected). This deficit increases with stellar mass (i.e. the most massive radio galaxies have the lowest FIR luminosities). The fact that the FIR luminosities of radio galaxies differ from those of normal galaxies suggests that radio-AGN activity is either directly, or indirectly, responsible. In this thesis, the explanation for the underlying FIR luminosity deficit of radio galaxies is the result of the interaction of the radio jets and the halo environment. In this scenario, the

radio jets help keep the halo environment hot, limiting the host's external sources of cold gas capable of producing star-formation and thus large amounts of FIR radiation. It is important to note that such an interpretation is inferred, although the mechanical heating of the halo by radio-jets is well established (e.g. Boehringer et al. 1993; Fabian et al. 2003, 2000, 2005; for a review see Fabian 2012). The presence of extended radio jets may also act as a selection effect, as hot-halo environments are expected to efficiently confine radio lobes, boosting the radio flux density above the flux density limit of the NVSS.

I also find that the negative dependence of the FIR luminosity and the dust temperature, on the radio source size points to jet-induced star formation. This is a form of 'direct' feedback, but in isolation, this would imply that radio galaxies should have, on average, higher FIR luminosities than normal galaxies. Since this is clearly not the case, jet-induced star formation is likely to have a relatively modest impact on the FIR luminosity. In addition, it is expected to be a relatively short term phenomenon without a large long-term impact in terms of stellar mass growth. Nevertheless, these results suggest that jet-induced star formation occurs in the radio galaxy population as a whole (e.g. in HERGs *and* LERGs). An analysis of the dust temperature dependence as a function of radio luminosity for compact and extended radio sources was presented. However, no statistically significant differences between the rate of increase of the dust temperature of compact vs extended radio galaxies was found. Better statistics, resulting in more data points and lower errors, and isolating that part of the radio luminosity which is expected to be involved in jet-induced star formation (e.g. lobe emission), may yet reveal evidence for jet-induced star formation.

In the final chapter, a methodology for reliably identifying high-z, star-bursting radio-loud AGN was presented. Such a method may be used to create a large sample with which further observations may be undertaken. Redshifts, dust temperatures and SFRs were cal-

culated for all seven sources. In addition, a method for determining whether direct radio-jet induced star-formation exists in the radio galaxy population was presented. This approach involves the use of high-resolution radio images (i.e. Very Long Baseline Interferometry) which will enable the lobe component of the radio luminosity to be isolated and plotted against the specific star-formation rate.

I believe that investigating the FIR / sub-mm properties of radio galaxies is important if we are to have a complete picture of the way galaxies have evolved over the last 13.8 billion years.

6.3 Future prospects

The analysis presented in this thesis may be extended and improved upon with additional data, due to be released in the near future. The *Herschel*-ATLAS has completed survey operations, and is due to publicly release the entire 550 sq degree data-set within a year. Ancillary data from the VISTA VIKING survey will provide deep NIR data for the phase 1 fields. This new data will allow a greater number of radio sources to be identified and studied, improving on the trends and relations found throughout this thesis by lowering the errors. Deeper NIR data will also enable the detection of higher-redshift radio galaxies, allowing one to determine and constrain their FIR properties. It will be interesting to determine the point at which the FIR luminosity of massive radio galaxies, equals, or surpasses that of the non-radio-detected population, as one might expect it to if the parallel increase in the SFR density (e.g. Madau et al. 1996) and the quasar density of the Universe are physically connected (e.g. Boyle & Terlevich 1998; Richards et al. 2006; Croom et al. 2009). To understand how radio emission results in lower FIR luminosities in some galaxies and not in others, will require a detailed study of the connection between the radio jets, the halo environment and the ISM.

Detailed studies of this kind may only be feasible for a few sources with excellent data across the electromagnetic spectrum. What will be need are: high-resolution, multi-frequency radio observations so that the evolution of the jets may be modelled and the mechanical heating rate calculated, ultra-violet / optical and NIR photometry to model the stellar population of the host and the past and present dust production rates, and finally, resolved FIR / sub-mm observations to trace the gas and dust content of the host and any physical connections these distributions may have with the radio jets.

A method for determining the existence of radio-jet induced star formation was presented in Chapter 5. There are several improvements which can be made. A larger survey area will also allow one to discover more rare, high-z star-bursting radio-loud AGN, improving statistics. The errors on the SFR may be reduced by the addition of sub-mm continuum observations using SUCBA-2 (Holland et al. 2006) and the Atacama Large Milimeter / sub-millimeter Array (ALMA). Such measurements also open the possibility of fitting two temperature models to the dust SED, allowing one to isolate the luminosity from the warmer component which is likely to be the result of star formation. Finally, the addition of VLBI observations and the measurement of other important galaxy parameters (e.g. stellar mass) will be invaluable in order to establish the existence, frequency and nature of direct radio-jet feedback.

The addition of new telescopes due to become fully operational in the near future should expand the potential for new science. ALMA will make the most sensitive high-resolution observations of cold gas in the distant Universe. This will allow one map the distribution of cold gas in galaxies. Studying how the propagation of radio jets through the ISM and IGM affect the gas mass, temperature and density will be of great interest to those studying

the effects of radio-AGN feedback. Square Kilometer Array (SKA) precursors (e.g. JVLA[1], MeerKAT[2], ASKAP[3]) will provide deep, high-resolution coverage at radio wavelengths for large parts of the sky. This will help identify the lower radio-luminosity source population at high redshift, limiting the sources of bias in future samples. In addition, these telescopes will be able to measure emission lines from neutral HI gas, adding another estimate to the total gas mass in high-z radio galaxies.

[1] Jansky Very Large Array
[2] Meer - Karoo Array Telescope
[3] Australian Square Kilometre Array Pathfinder

Appendix A: FIR differences of high and low excitation radio galaxies

The work presented in this appendix is based on an article published in '*Monthly Notices of the Royal Astronomical Society*.' Here I describe the part of the analysis which I was closely associated with.

Hardcastle M. J., Ching J.H.Y., Virdee J. S., et al., 2013, MNRAS, 429, 2407: '*Herschel-ATLAS/GAMA: a difference between star formation rates in strong-line and weak-line radio galaxies*'

Introduction

The differences between HERGs and LERGs is covered in detail in Section 1.4.3. Nevertheless, a brief review is provided here. Fundamentally, the differences between HERGs and LERGs are believed to be the result of the properties of the fuelling gas; HERGs are fuelled by cold gas whereas LERGs are argued to be fuelled by hot gas (Hardcastle, Evans & Croston 2007). Cold gas accretion leads to radiatively efficient emission with high-excitation lines in the optical spectra of AGN, whereas hot gas accretion leads to radiatively inefficient emis-

sion with little or no high-excitation lines. The temperature of the fuelling gas is indicative of the environment of the galaxy. Thus, hot-gas fuelling suggests the presence of a hot-halo environment, which massive elliptical galaxies tend to be embedded in. Sources of cold gas are limited by the shock heating of in-falling material and the ram-pressure-stripping of 'wet' galaxies. Therefore, LERGs tend to be hosted by the canonical 'red and dead' ellipticals with all their associated properties. On the other-hand, cold-gas fuelling is associated with a much broader range of galaxy masses, higher SFRs, bluer optical-colours, and disturbed morphologies (e.g. Baldi & Capetti 2008; Herbert et al. 2010; Ramos Almeida et al. 2011; Best & Heckman 2012; Janssen et al. 2012).

In this appendix, I briefly describe the main findings of the article I was involved with and highlight the work I closely associated with. The radio catalogue which forms the basis of the analysis presented here was created by John Ching (see Section 2.6 for a description of the catalogue, referred to there as the JCC). The catalogue uses FIRST and NVSS data, cross-matched with SDSS galaxies with optical spectra. The result was 1824 matched sources.

FIR luminosities of HERGs and LERGs as a function of radio size

The key result from Hardcastle et al. [2013] is that HERGs have systematically higher FIR luminosities at 250 μm than LERGs. In addition, HERGs have dust temperatures which peak at ~ 30 K whereas LERGs occupy a wide temperature range, from $10 < T < 30$ K. These results are consistent with the view that HERGs have higher SFRs and dust masses than LERGs.

The primary contribution I made to the paper was measuring the projected radio sizes for all the radio sources in the sample. This allowed an investigation of the FIR luminosity and the dust temperatures of HERGs and LERGs as a function of radio source size. The results

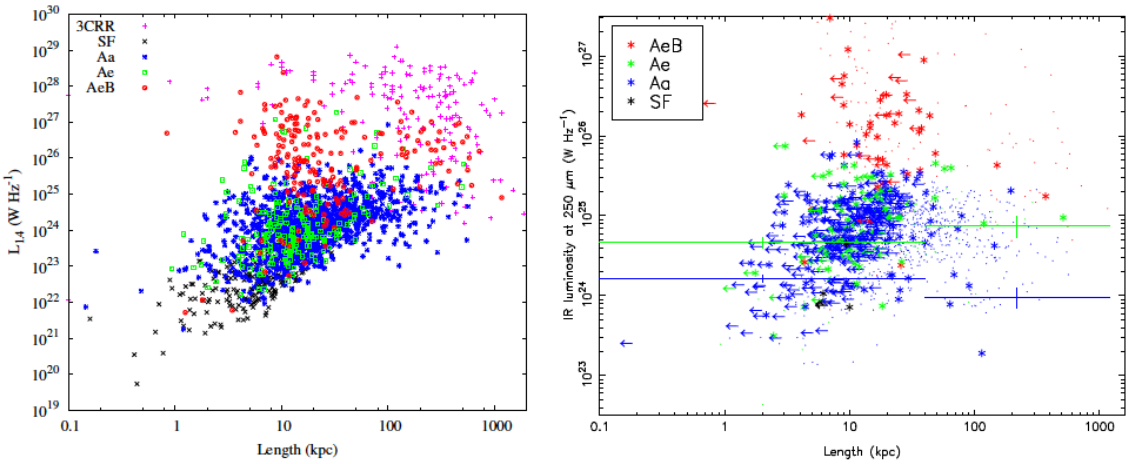

Figure 1: The physical sizes of radio sources and their relationship to radio and FIR luminosity. In the plots, SF stands for 'star-forming', Ae and AeB represent HERGs and Aa represent LERGs. (left) The power / linear-size plot for the sample. (right) FIR luminosity as a function of length (Fig. 10 from Hardcastle et al. 2013).

are shown in Fig. 1. An important caveat in this analysis is that the sample is not complete in $L_{1.4\,\mathrm{GHz}}$ - radio source size space. This is illustrated on the left-hand panel of Fig. 1 which plots the power / linear size diagram for the current sample together with the 3CRR[1] sample. The limited survey area of the H-ATLAS compared to that covered by 3CRR results in fewer sources $> 10^{27}$ W Hz^{-1}, which might be expected to have larger sizes.

Nevertheless, it is still possible to investigate the FIR properties as a function of projected radio size. First, it is clear that the HERGs (Ae + Aeb) / LERGs (Aa) difference persists in this analysis, i.e. HERG sources have higher L_{250} than LERGs irrespective of length. Secondly, I see no evidence for any length dependence of L_{250} for the HERG population, although the error bars are large because the sample is small. Thirdly, I note a marginally significant difference between the L_{250} values for the small and large LERG sources: the null hypothesis that these two are equal can be rejected at the 95% confidence level. However, there is a significant difference in best-fitting temperature in both cases, in the sense that the larger objects have lower best-fitting temperatures (i.e. 29.4 ± 0.5 vs 22 ± 2 K for HERGs;

[1] Third Cambridge Catalogue of Radio Sources

21.8 ± 0.5 vs 12.2 ± 0.4 K for LERGs).

Conclusions

The main conclusions of Hardcastle et al. [2013] are:

1. The rest-frame 250 μm luminosity of HERGs are systematically higher than in LERGs. This difference is apparent at all redshifts and all radio luminosities sampled by our targets.

2. A comparison of the temperatures and dust masses of HERGs and LERGs, stacked in coarse bins, suggests that the dust masses are reasonably comparable for the two samples but that the temperatures in the HERGs are systematically higher.

3. Consistent with the results of Section 3.5.2, we find that HERGs show little to no evidence for a dependence of FIR luminosity on radio source size, while LERGs show marginal evidence for a dependence of FIR luminosity on radio source size

4. Both HERGs and LERGs show a temperature dependence as a function of radio source size, in the sense that the temperature decreases with increasing length. This may be due to radio-jet ISM interactions.

References

Abazajian K. N. et al., 2009, ApJS, 182, 543, arXiv:0812.0649 54

Abramson A., Kenney J. D. P., Crowl H. H., Chung A., van Gorkom J. H., Vollmer B., Schiminovich D., 2011, AJ, 141, 164, arXiv:1101.4066 87

Ahn C. P. et al., 2012, ApJS, 203, 21, arXiv:1207.7137 11

Allen S. W., Dunn R. J. H., Fabian A. C., Taylor G. B., Reynolds C. S., 2006, MNRAS, 372, 21, arXiv:astro-ph/0602549 19, 25

Alvarez M. A., Wise J. H., Abel T., 2009, ApJ, 701, L133, arXiv:0811.0820 11

Amblard A. et al., 2010, A&A, 518, L9+, arXiv:1005.2412 33, 96

Antognini J., Bird J., Martini P., 2012, ApJ, 756, 116, arXiv:1204.3896 22

Antonucci R., 1993, ARA&A, 31, 473 15

Appleton P. et al., 2004, in Bulletin of the American Astronomical Society, Vol. 36, American Astronomical Society Meeting Abstracts #204, p. 815 34

Archibald E. N., Dunlop J. S., Hughes D. H., Rawlings S., Eales S. A., Ivison R. J., 2001, MNRAS, 323, 417, arXiv:astro-ph/0002083 3, 52, 84, 118, 139, 154

Baldi R. D., Capetti A., 2008, A&A, 489, 989, arXiv:0808.1555 20, 24, 160

Baldi R. D., Capetti A., 2010, A&A, 519, A48, arXiv:1005.3223 24

Baldry I. K. et al., 2010, MNRAS, 404, 86, arXiv:0910.5120 55

Barthel P., Haas M., Leipski C., Wilkes B., 2012, ApJ, 757, L26, arXiv:1209.0324 73

Barthel P. D., Arnaud K. A., 1996, MNRAS, 283, L45 25

Becker R. H., White R. L., Helfand D. J., 1995, ApJ, 450, 559 38, 53, 57

Beckmann V., Shrader C. R., 2013, ArXiv e-prints, arXiv:1302.1397 16

Begelman M. C., Cioffi D. F., 1989, ApJ, 345, L21 88, 118

Benson A. J., Bower R. G., Frenk C. S., Lacey C. G., Baugh C. M., Cole S., 2003, ApJ, 599, 38, arXiv:astro-ph/0302450 2, 12, 13

Benson A. J., Lacey C. G., Baugh C. M., Cole S., Frenk C. S., 2002, MNRAS, 333, 156, arXiv:astro-ph/0108217 2, 13

Best P. N., 2000, MNRAS, 317, 720, arXiv:astro-ph/0007285 25

Best P. N., Heckman T. M., 2012, MNRAS, 2402, arXiv:1201.2397 24, 26, 60, 85, 160

Best P. N., Kaiser C. R., Heckman T. M., Kauffmann G., 2006, MNRAS, 368, L67, arXiv:astro-ph/0602171 13, 25

Best P. N., Kauffmann G., Heckman T. M., Brinchmann J., Charlot S., Ivezić Ž., White S. D. M., 2005, MNRAS, 362, 25, arXiv:astro-ph/0506269 3, 20, 21, 22, 25

Best P. N., Longair M. S., Röttgering H. J. A., 1998, MNRAS, 295, 549, arXiv:astro-ph/9709195 22, 58

Best P. N., von der Linden A., Kauffmann G., Heckman T. M., Kaiser C. R., 2007, MNRAS, 379, 894, arXiv:astro-ph/0611197 25

Bianchi S., Maiolino R., Risaliti G., 2012, Advances in Astronomy, 2012, arXiv:1201.2119 15

Binney J., 2004, MNRAS, 347, 1093, arXiv:astro-ph/0308172 14

Bird J., Martini P., Kaiser C., 2008, ApJ, 676, 147, arXiv:0709.2167 22

Bîrzan L., Rafferty D. A., McNamara B. R., Wise M. W., Nulsen P. E. J., 2004, ApJ, 607, 800, arXiv:astro-ph/0402348 86

Blanton M. R., Roweis S., 2007, AJ, 133, 734, arXiv:astro-ph/0606170 55

Boehringer H., Voges W., Fabian A. C., Edge A. C., Neumann D. M., 1993, MNRAS, 264, L25 87, 155

Bournaud F. et al., 2011, ApJ, 730, 4 8

Bourne N. et al., 2012, MNRAS, 421, 3027, arXiv:1201.1916 1, 33, 106

Bower R. G., Benson A. J., Malbon R., Helly J. C., Frenk C. S., Baugh C. M., Cole S., Lacey C. G., 2006, MNRAS, 370, 645, arXiv:astro-ph/0511338 3, 14

Bower R. G., McCarthy I. G., Benson A. J., 2008, MNRAS, 390, 1399, arXiv:0808.2994 3, 14

Boyle B. J., Terlevich R. J., 1998, MNRAS, 293, L49, arXiv:astro-ph/9710134 19, 156

Bromm V., Larson R. B., 2004, ARA&A, 42, 79, arXiv:astro-ph/0311019 8

Bromm V., Yoshida N., 2011, ARA&A, 49, 373, arXiv:1102.4638 8, 9

Bruzual G., Charlot S., 2003, MNRAS, 344, 1000, arXiv:astro-ph/0309134 58

Buttiglione S., Capetti A., Celotti A., Axon D. J., Chiaberge M., Macchetto F. D., Sparks W. B., 2010, A&A, 509, A6, arXiv:0911.0536 24

Calzetti D., 2012, ArXiv e-prints, arXiv:1208.2997 2, 29

Cattaneo A. et al., 2009, Nat, 460, 213, arXiv:0907.1608 15

Cattaneo A., Mamon G. A., Warnick K., Knebe A., 2011, A&A, 533, A5, arXiv:1002.3257 8

Cid Fernandes R., Stasińska G., Schlickmann M. S., Mateus A., Vale Asari N., Schoenell W., Sodré L., 2010, MNRAS, 403, 1036, arXiv:0912.1643 24

Cole S., Lacey C. G., Baugh C. M., Frenk C. S., 2000, MNRAS, 319, 168, arXiv:astro-ph/0007281 2, 13

Cole S. et al., 2001, MNRAS, 326, 255, arXiv:astro-ph/0012429 12

Collister A. A., Lahav O., 2004, PASP, 116, 345, arXiv:astro-ph/0311058 54

Comastri A., Setti G., Zamorani G., Hasinger G., 1995, A&A, 296, 1, arXiv:astro-ph/9409067 19

Condon J. J., 1992, ARA&A, 30, 575 27, 28, 34

Condon J. J., Cotton W. D., Greisen E. W., Yin Q. F., Perley R. A., Taylor G. B., Broderick J. J., 1998, AJ, 115, 1693 37, 53, 56

Croom S. M. et al., 2009, MNRAS, 399, 1755, arXiv:0907.2727 156

Croton D. J. et al., 2006, MNRAS, 365, 11, arXiv:astro-ph/0508046 3, 18

da Cunha E., Charlot S., Elbaz D., 2008, MNRAS, 388, 1595, arXiv:0806.1020 74

Daddi E. et al., 2010, ApJ, 713, 686, arXiv:0911.2776 9

Davies J. I. et al., 2010, A&A, 518, L48, arXiv:1005.3054 100

Davies J. I. et al., 2012, MNRAS, 419, 3505, arXiv:1110.2869 100

De Breuck C., Reuland M., 2003, ArXiv Astrophysics e-prints, arXiv:astro-ph/0312526 118

De Breuck C., van Breugel W., Stanford S. A., Röttgering H., Miley G., Stern D., 2002, AJ, 123, 637, arXiv:astro-ph/0109540 22

de Graauw T. et al., 2010, A&A, 518, L6 31

Dekel A., Birnboim Y., 2006, MNRAS, 368, 2, arXiv:astro-ph/0412300 26

Dekel A. et al., 2009, Nat, 457, 451, arXiv:0808.0553 9, 10, 14

Del Moro A. et al., 2013, A&A, 549, A59, arXiv:1210.2521 73

Dey A., van Breugel W., Vacca W. D., Antonucci R., 1997, ApJ, 490, 698, arXiv:astro-ph/9707166 118

Di Matteo T., Springel V., Hernquist L., 2005, Nat, 433, 604, arXiv:astro-ph/0502199 3

Dicken D. et al., 2012, ApJ, 745, 172, arXiv:1111.4476 88, 108

Dole H. et al., 2006, A&A, 451, 417, arXiv:astro-ph/0603208 1

Draine B. T., Li A., 2007, ApJ, 657, 810, arXiv:astro-ph/0608003 1

Draine B. T., Salpeter E. E., 1979, ApJ, 231, 77 87

Driver S. P. et al., 2011, MNRAS, 413, 971, arXiv:1009.0614 55

Driver S. P. et al., 2009, Astronomy and Geophysics, 50, 050000, arXiv:0910.5123 32, 55

Driver S. P., Popescu C. C., Tuffs R. J., Graham A. W., Liske J., Baldry I., 2008, ApJ, 678, L101, arXiv:0803.4164 1

Dunlop J. S., McLure R. J., Kukula M. J., Baum S. A., O'Dea C. P., Hughes D. H., 2003, MNRAS, 340, 1095, arXiv:astro-ph/0108397 19

Dunne L. et al., 2011, MNRAS, 417, 1510, arXiv:1012.5186 1, 3, 32, 33, 73, 74, 76, 77

Dwek E. et al., 1998, ApJ, 508, 106, arXiv:astro-ph/9806129 1

Dye S. et al., 2010, A&A, 518, L10+, arXiv:1005.2411 63

Eales S. et al., 2010a, PASP, 122, 499, arXiv:0910.4279 4, 31, 37, 52

Eales S. A. et al., 2010b, A&A, 518, L23, arXiv:1005.2189 3

Eisenstein D. J., Loeb A., 1995, ApJ, 443, 11, arXiv:astro-ph/9401016 11

El Bouchefry K., 2009, Astronomische Nachrichten, 330, 871, arXiv:0906.4956 20

Fabian A. C., 2012, ARA&A, 50, 455, arXiv:1204.4114 87, 155

Fabian A. C., Sanders J. S., Allen S. W., Crawford C. S., Iwasawa K., Johnstone R. M., Schmidt R. W., Taylor G. B., 2003, MNRAS, 344, L43, arXiv:astro-ph/0306036 155

Fabian A. C. et al., 2000, MNRAS, 318, L65, arXiv:astro-ph/0007456 155

Fabian A. C., Sanders J. S., Taylor G. B., Allen S. W., 2005, MNRAS, 360, L20, arXiv:astro-ph/0503154 155

Fan X. et al., 2001, AJ, 122, 2833, arXiv:astro-ph/0108063 11

Fanaroff B. L., Riley J. M., 1974, MNRAS, 167, 31P 20

Fazio G. G. et al., 2004, ApJS, 154, 10, arXiv:astro-ph/0405616 30

Fixsen D. J., Dwek E., Mather J. C., Bennett C. L., Shafer R. A., 1998, ApJ, 508, 123, arXiv:astro-ph/9803021 1

Fleuren S. et al., 2012, MNRAS, 423, 2407, arXiv:1202.3891 139

Floyd D. J. E., Kukula M. J., Dunlop J. S., McLure R. J., Miller L., Percival W. J., Baum S. A., O'Dea C. P., 2004, MNRAS, 355, 196, arXiv:astro-ph/0308436 19

Gaibler V., Khochfar S., Krause M., Silk J., 2012, MNRAS, 425, 438, arXiv:1111.4478 88, 109, 118

Galametz A. et al., 2012a, ApJ, 749, 169, arXiv:1202.4489 25

Galametz M. et al., 2012b, MNRAS, 425, 763, arXiv:1207.1301 100

Gehrz R., 1989, in IAU Symposium, Vol. 135, Interstellar Dust, Allamandola L. J., Tielens A. G. G. M., eds., p. 445 1

Gilli R., Comastri A., Hasinger G., 2007, A&A, 463, 79, arXiv:astro-ph/0610939 19

Gilli R., Salvati M., Hasinger G., 2001, A&A, 366, 407, arXiv:astro-ph/0011341 19

Glover S., 2005, Space Science Reviews, 117, 445, arXiv:astro-ph/0409737 8

Golombek D., Miley G. K., Neugebauer G., 1988, AJ, 95, 26 30

Granato G. L., De Zotti G., Silva L., Bressan A., Danese L., 2004, ApJ, 600, 580, arXiv:astro-ph/0307202 3

Greif T. H., Glover S. C. O., Bromm V., Klessen R. S., 2010, ApJ, 716, 510 8

Greif T. H., Johnson J. L., Klessen R. S., Bromm V., 2008, MNRAS, 387, 1021, arXiv:0803.2237 8

Griffin M. J. et al., 2010, A&A, 518, L3+, arXiv:1005.5123 31, 54

Gültekin K. et al., 2009, ApJ, 698, 198, arXiv:0903.4897 10

Haas M. et al., 2004, A&A, 424, 531, arXiv:astro-ph/0406111 30

Hardcastle M. J. et al., 2013, MNRAS, 429, 2407, arXiv:1211.6440 24, 48, 63, 99, 140, 144, 150, 160, 161, 162

Hardcastle M. J., Evans D. A., Croston J. H., 2007, MNRAS, 376, 1849, arXiv:astro-ph/0701857 25, 26, 159

Hardcastle M. J., Evans D. A., Croston J. H., 2009, MNRAS, 396, 1929, arXiv:0904.1323 18, 73

Hardcastle M. J. et al., 2010, MNRAS, 409, 122, arXiv:1009.5866 52

Harwit M., Pacini F., 1975, ApJ, 200, L127 34

Heckman T. M., Smith E. P., Baum S. A., van Breugel W. J. M., Miley G. K., Illingworth G. D., Bothun G. D., Balick B., 1986, ApJ, 311, 526 24

Helou G., Khan I. R., Malek L., Boehmer L., 1988, ApJS, 68, 151 34

Helou G., Soifer B. T., Rowan-Robinson M., 1985, ApJ, 298, L7 34

Herbert P. D., Jarvis M. J., Willott C. J., McLure R. J., Mitchell E., Rawlings S., Hill G. J., Dunlop J. S., 2010, MNRAS, 406, 1841, arXiv:1004.1099 24, 160

Hes R., Barthel P. D., Hoekstra H., 1995, A&A, 303, 8 58

Hickox R. C., Mullaney J. R., Alexander D. M., Chen C.-T. J., Civano F. M., Goulding A. D., Hainline K. N., 2013, ArXiv e-prints, arXiv:1306.3218 118

Hine R. G., Longair M. S., 1979, MNRAS, 188, 111 24

Hogg D. W., 1999, ArXiv Astrophysics e-prints, arXiv:astro-ph/9905116 6

Holland W. et al., 2006, in Society of Photo-Optical Instrumentation Engineers (SPIE) Conference Series, Vol. 6275, Society of Photo-Optical Instrumentation Engineers (SPIE) Conference Series 157

Hopkins P. F., Hernquist L., Cox T. J., Di Matteo T., Robertson B., Springel V., 2006, ApJS, 163, 1, arXiv:astro-ph/0506398 19

Houck J. R. et al., 2004, ApJS, 154, 18, arXiv:astro-ph/0406167 30

Huang J.-S., Glazebrook K., Cowie L. L., Tinney C., 2003, ApJ, 584, 203, arXiv:astro-ph/0209440 12

Hwang H. S. et al., 2010, MNRAS, 409, 75, arXiv:1009.1058 33, 96

Ibar E. et al., 2010, MNRAS, 409, 38, arXiv:1009.0262 32, 54

Impey C., Gregorini L., 1993, AJ, 105, 853 30

Ivison R. J. et al., 2010, A&A, 518, L31+, arXiv:1005.1072 34

Jackson N., Rawlings S., 1997, MNRAS, 286, 241 24

Janssen R. M. J., Röttgering H. J. A., Best P. N., Brinchmann J., 2012, A&A, 541, A62, arXiv:1206.0578 24, 160

Jarvis M. J., Rawlings S., Eales S., Blundell K. M., Bunker A. J., Croft S., McLure R. J., Willott C. J., 2001, MNRAS, 326, 1585, arXiv:astro-ph/0106130 19, 133

Jarvis M. J. et al., 2010, MNRAS, 409, 92, arXiv:1009.5390 34, 65, 141

Johnson J. L., Bromm V., 2007, MNRAS, 374, 1557, arXiv:astro-ph/0605691 11

Kaiser C. R., Dennett-Thorpe J., Alexander P., 1997, MNRAS, 292, 723, arXiv:astro-ph/9710104 53, 81, 113

Kalfountzou E., Jarvis M. J., Bonfield D. G., Hardcastle M. J., 2012, MNRAS, 427, 2401, arXiv:1209.2329 118

Kauffmann G., Charlot S., 1998, MNRAS, 297, L23, arXiv:astro-ph/9802233 58

Kellermann K. I., Sramek R., Schmidt M., Shaffer D. B., Green R., 1989, AJ, 98, 1195 15

Kennicutt R. C. et al., 2011, PASP, 123, 1347, arXiv:1111.4438 100

Kennicutt, Jr. R. C., 1998a, ARA&A, 36, 189, arXiv:astro-ph/9807187 2

Kennicutt, Jr. R. C., 1998b, ApJ, 498, 541, arXiv:astro-ph/9712213 29, 61, 63

Kennicutt, Jr. R. C. et al., 2009, ApJ, 703, 1672, arXiv:0908.0203 29, 63

Kereš D., Katz N., Weinberg D. H., Davé R., 2005, MNRAS, 363, 2, arXiv:astro-ph/0407095 9, 26

Kessler M. F. et al., 1996, A&A, 315, L27 30

Kochanek C. S. et al., 2001, ApJ, 560, 566, arXiv:astro-ph/0011456 12

Lawrence A. et al., 2007, MNRAS, 379, 1599, arXiv:astro-ph/0604426 38, 54

Leighly K. M., Halpern J. P., Jenkins E. B., Casebeer D., 2007, ApJS, 173, 1, arXiv:0705.0940 132

Li A., Draine B. T., 2001, ApJ, 554, 778, arXiv:astro-ph/0011319 1

Li Y. et al., 2007, ApJ, 665, 187, arXiv:astro-ph/0608190 11

Loeb A., Rasio F. A., 1994, ApJ, 432, 52, arXiv:astro-ph/9401026 11

Lynden-Bell D., Pringle J. E., 1974, MNRAS, 168, 603 15

Madau P., Ferguson H. C., Dickinson M. E., Giavalisco M., Steidel C. C., Fruchter A., 1996, MNRAS, 283, 1388, arXiv:astro-ph/9607172 102, 156

Madau P., Rees M. J., 2001, ApJ, 551, L27, arXiv:astro-ph/0101223 11

Magdis G. E. et al., 2010, MNRAS, 409, 22, arXiv:1007.4900 33

Magorrian J. et al., 1998, AJ, 115, 2285, arXiv:astro-ph/9708072 10

Marconi A., 2006, Memorie della Societa Astronomica Italiana Supplementi, 9, 285 18

Marconi A., Hunt L. K., 2003, ApJ, 589, L21, arXiv:astro-ph/0304274 10

Martínez-Sansigre A., Rawlings S., Garn T., Green D. A., Alexander P., Klöckner H.-R., Riley J. M., 2006a, MNRAS, 373, L80, arXiv:astro-ph/0609030 31

Martínez-Sansigre A., Rawlings S., Lacy M., Fadda D., Jarvis M. J., Marleau F. R., Simpson C., Willott C. J., 2006b, MNRAS, 370, 1479, arXiv:astro-ph/0604382 31

Martínez-Sansigre A., Rawlings S., Lacy M., Fadda D., Marleau F. R., Simpson C., Willott C. J., Jarvis M. J., 2005, Nat, 436, 666, arXiv:astro-ph/0505486 31

Martizzi D., Teyssier R., Moore B., Wentz T., 2012, MNRAS, 422, 3081, arXiv:1112.2752 3

Matthews T. A., Morgan W. W., Schmidt M., 1964, ApJ, 140, 35 19

Mauch T., Klöckner H.-R., Rawlings S., Jarvis M., Hardcastle M. J., Obreschkow D., Saikia D. J., Thompson M. A., 2013, MNRAS, arXiv:1307.4590 54, 57, 83, 120

Mauch T., Sadler E. M., 2007, MNRAS, 375, 931, arXiv:astro-ph/0612018 3, 27, 60

McLure R. J., Dunlop J. S., 2002, MNRAS, 331, 795, arXiv:astro-ph/0108417 10

McLure R. J., Willott C. J., Jarvis M. J., Rawlings S., Hill G. J., Mitchell E., Dunlop J. S., Wold M., 2004, MNRAS, 351, 347, arXiv:astro-ph/0403106 24, 45, 108

McNamara B. R., Nulsen P. E. J., 2012, New Journal of Physics, 14, 055023, arXiv:1204.0006 87

Meisenheimer K., Haas M., Müller S. A. H., Chini R., Klaas U., Lemke D., 2001, A&A, 372, 719, arXiv:astro-ph/0102333 30

Mellema G., Kurk J. D., Röttgering H. J. A., 2002, A&A, 395, L13, arXiv:astro-ph/0209601 118

Merloni A., Heinz S., 2008, MNRAS, 388, 1011, arXiv:0805.2499 3

Merritt D., Ferrarese L., 2001, ApJ, 547, 140, arXiv:astro-ph/0008310 10

Molinari S. et al., 2010, PASP, 122, 314, arXiv:1001.2106 100

Müller S. A. H., Haas M., Siebenmorgen R., Klaas U., Meisenheimer K., Chini R., Albrecht M., 2004, A&A, 426, L29, arXiv:astro-ph/0409719 30

Narayan R., Mahadevan R., Quataert E., 1998, in Theory of Black Hole Accretion Disks, Abramowicz M. A., Bjornsson G., Pringle J. E., eds., p. 148 16

Negrello M. et al., 2010, Science, 330, 800, arXiv:1011.1255 147

Novikov I. D., Thorne K. S., 1973, in Black Holes (Les Astres Occlus), Dewitt C., Dewitt B. S., eds., pp. 343–450 15

Oliver S. J. et al., 2012, MNRAS, 424, 1614, arXiv:1203.2562 32

Paradis D. et al., 2010, A&A, 520, L8, arXiv:1009.2779 100

Pascale E. et al., 2010, in EAS Publications Series, Vol. 40, EAS Publications Series, L. Spinoglio & N. Epchtein, ed., pp. 411–415 32, 62

Pascale E. et al., 2011, MNRAS, 415, 911, arXiv:1010.5782 54

Pelupessy F. I., Di Matteo T., Ciardi B., 2007, ApJ, 665, 107 11

Pilbratt G. L. et al., 2010, A&A, 518, L1+, arXiv:1005.5331 3, 52

Planck Collaboration et al., 2013a, ArXiv e-prints, arXiv:1303.5062 7

Planck Collaboration et al., 2013b, ArXiv e-prints, arXiv:1303.5076 6

Poglitsch A. et al., 2010, A&A, 518, L2, arXiv:1005.1487 31, 54

Ramos Almeida C., Tadhunter C. N., Inskip K. J., Morganti R., Holt J., Dicken D., 2011, MNRAS, 410, 1550, arXiv:1008.2683 24, 160

Rawlings S., Jarvis M. J., 2004, MNRAS, 355, L9, arXiv:astro-ph/0409687 16

Rees M. J., 1989, MNRAS, 239, 1P 88

Rees M. J., Ostriker J. P., 1977, MNRAS, 179, 541 13

Reuland M., Röttgering H., van Breugel W., De Breuck C., 2004, MNRAS, 353, 377, arXiv:astro-ph/0405567 3, 52, 84, 118, 139, 154

Reuland M., van Breugel W., Röttgering H., de Vries W., De Breuck C., Stern D., 2003, ApJ, 582, L71, arXiv:astro-ph/0302432 31

Richards G. T. et al., 2006, AJ, 131, 2766, arXiv:astro-ph/0601434 156

Rieke G. H. et al., 2004, ApJS, 154, 25 30

Riess A. G. et al., 2009, ApJ, 699, 539, arXiv:0905.0695 6

Rigby E. E., Best P. N., Brookes M. H., Peacock J. A., Dunlop J. S., Röttgering H. J. A., Wall J. V., Ker L., 2011a, MNRAS, 416, 1900, arXiv:1104.5020 138

Rigby E. E. et al., 2011b, MNRAS, 415, 2336, arXiv:1010.5787 52, 119

Rowlands K. et al., 2012, MNRAS, 419, 2545, arXiv:1109.6274 1

Sadler E. M. et al., 2002, MNRAS, 329, 227, arXiv:astro-ph/0106173 3, 27, 60, 61

Sanders D. B., Mirabel I. F., 1996, ARA&A, 34, 749 28, 29

Sanders D. B., Soifer B. T., Elias J. H., Madore B. F., Matthews K., Neugebauer G., Scoville N. Z., 1988, ApJ, 325, 74 18

Seymour N. et al., 2007, ApJS, 171, 353, arXiv:astro-ph/0703224 31

Shakura N. I., Sunyaev R. A., 1973, A&A, 24, 337 15

Shetty R., Kauffmann J., Schnee S., Goodman A. A., 2009a, ApJ, 696, 676, arXiv:0902.0636 98

Shetty R., Kauffmann J., Schnee S., Goodman A. A., Ercolano B., 2009b, ApJ, 696, 2234, arXiv:0902.3477 98

Sijacki D., Springel V., 2006, MNRAS, 366, 397, arXiv:astro-ph/0509506 3

Simpson C., Rawlings S., Lacy M., 1999, MNRAS, 306, 828, arXiv:astro-ph/9902087 22, 58

Smith A. J., Loveday J., Cross N. J. G., 2009, MNRAS, 397, 868, arXiv:0806.0343 58

Smith D. J. B. et al., 2011, MNRAS, 416, 857, arXiv:1007.5260 54, 120, 139

Soifer B. T., Sanders D. B., Madore B. F., Neugebauer G., Danielson G. E., Elias J. H., Lonsdale C. J., Rice W. L., 1987, ApJ, 320, 238 29

Springel V., Frenk C. S., White S. D. M., 2006, Nat, 440, 1137, arXiv:astro-ph/0604561 8

Springel V. et al., 2005, Nat, 435, 629, arXiv:astro-ph/0504097 2, 8

Tabatabaei F. S. et al., 2013, A&A, 552, A19, arXiv:1301.6884 34

Tadhunter C. et al., 2011, MNRAS, 412, 960, arXiv:1011.2096 25, 108, 150

Tadhunter C. N., Morganti R., Robinson A., Dickson R., Villar-Martin M., Fosbury R. A. E., 1998, MNRAS, 298, 1035, arXiv:astro-ph/9807238 24

Tanaka T., Haiman Z., 2009, ApJ, 696, 1798, arXiv:0807.4702 11

Taylor M. B., 2005, in Astronomical Society of the Pacific Conference Series, Vol. 347, Astronomical Data Analysis Software and Systems XIV, P. Shopbell, M. Britton, & R. Ebert, ed., p. 29 55

Tremaine S. et al., 2002, ApJ, 574, 740, arXiv:astro-ph/0203468 10

Urry C. M., Padovani P., 1995, PASP, 107, 803, arXiv:astro-ph/9506063 15

van Breugel W. J. M., Dey A., 1993, ApJ, 414, 563 118

van Breugel W. J. M., Stanford S. A., Spinrad H., Stern D., Graham J. R., 1998, ApJ, 502, 614, arXiv:astro-ph/9803019 23

Vogelsberger M., Genel S., Sijacki D., Torrey P., Springel V., Hernquist L.,), 2013, ArXiv e-prints, arXiv:1305.2913 3

Vollmer B. et al., 2012, A&A, 537, A143, arXiv:1111.5236 87

Volonteri M., Rees M. J., 2006, ApJ, 650, 669, arXiv:astro-ph/0607093 11

Wang T. et al., 2012, ApJ, 752, 134, arXiv:1204.4194 8

Werner M. W. et al., 2004, ApJS, 154, 1, arXiv:astro-ph/0406223 30

White S. D. M., Rees M. J., 1978, MNRAS, 183, 341 13

Willott C. J., Rawlings S., Jarvis M. J., Blundell K. M., 2003, MNRAS, 339, 173, arXiv:astro-ph/0209439 11, 19, 23, 45, 119

Wise J. H., Abel T., 2007, ApJ, 665, 899, arXiv:0704.3629 8

Wise J. H., Abel T., 2008, ApJ, 685, 40 8

Worpel H., Brown M. J. I., Jones D. H., Floyd D. J. E., Beutler F., 2013, ArXiv e-prints, arXiv:1305.2673 25

Wylezalek D. et al., 2013, ArXiv e-prints, arXiv:1304.0770 25